Carl Erik Lie Foss

Thermal Stability and Electrochemical Performance of Graphite Anodes in Li-ion Batteries

Thesis for the degree of Philosophiae Doctor

Trondheim, April 2014

Norwegian University of Science and Technology
Faculty of Natural Sciences and Technology
Department of Materials Science and Engineering

NTNU – Trondheim
Norwegian University of
Science and Technology

NTNU
Norwegian University of Science and Technology

Thesis for the degree of Philosophiae Doctor

Faculty of Natural Sciences and Technology
Department of Materials Science and Engineering

ISBN 978-82-326-0126-4 (printed ver.)
ISBN 978-82-326-0127-1 (electronic ver.)
ISSN 1503-8181

IMT-Report 2014:201

Doctoral theses at NTNU, 2014:101

Printed by NTNU-trykk

Preface

This thesis has been a part of a project titled “Carbon materials for improved stability of anodes in lithium ion batteries” (CARBATT). The project had the following research partners (grant number 195432/S10); Elkem Carbon, SINTEF, NTNU, CarboTech Holding AS, and Miljøbil Grenland. Elkem Carbon supplied the project with the various carbon materials used for testing.

All the work in this thesis has been performed by the author except; DSC results performed by MsC Øystein Gullbrekken in Chapter 5 (Fig. 5.2 and 5.3), XRD results by MsC Ingrid Roten Mattson in Chapter 4 (Table 4.1), and oxygen analysis was performed by Dr Rebecca Thorne. Particle size distributions (with Camsizer) was sent and measured at Elkem carbon. My main supervisor, Fride Vullum-Bruer, and co-supervisors, Svein Sunde and Ann Mari Svensson, have all contributed to the discussion of the results in Chapters 4 through 7.

Carl Erik Lie Foss
Trondheim, 3. februar 2014

Acknowledgement

There are several people deserving of an acknowledgement for the work produced in this thesis. First of all I have to thank my main supervisor, Fride Vullum-Bruer, for excellent guidance and support these past four years. I would also like to thank my co-supervisor, Ann Mari Svensson and Svein Sunde for their contribution to the discussions and always finding time to help me with my work. I would like to especially mention Ann Mari Svensson, as she took over as main supervisor during Fride Vullum-Bruer's maternity leave. You have all been very kind and patient with me.

There are also several colleagues at department of material science, which have been most helpful. Julian Tolchard has been very kind with regards to help with SEM and XRD measurements. Whenever I needed some equipment or just a chat, Kjell Røkke was always there to help. Martha Bjerknes always brightened the morning with a friendly hello, and she also was most helpful with travel bills etc. Also I would like to thank Frode Seland for always taking the time to chat and help with electrochemical questions, Edel Sheridan, who was extremely helpful and valuable in the start up as well as throughout, and Morten Onsrud for being a helpful colleague and an easy going guy. Thanks to all the master students working on the same project; Øystein Gullbrekken, Ingrid Roten Mattson and Phung Tran

Elkem Carbon, SINTEF, NTNU, CarboTech Holding AS, and Miljøbil Grenland are acknowledged for their financial support.

My stay here in Trondheim has been made most enjoyable, largely due to the fact that so many of my friends have stayed here as well. The entire soccer team of Polycrystal Palace is acknowledged for great football sessions, and some nice social events. My old friends and colleagues; Tor Olav Sunde, Morten Tjelta, Torunn Ervik, Vegar Øygarden, Astri B Haugen, Astrid Bakken, Ørjan F. Lohne, Conor McCarthy, Tobias Danner, Markus Bernhardt, Jostein Malmo, Magnus Hattrem, Rebecca Thorne and also I would like to thank my office mates Ahmet Tezel and Stefanus Lombing.

Finally I would like to thank my family for their endless love and support, and perhaps most importantly, I would like to thank my very patient and caring girlfriend, Anne Marthe Nymark.

Table of contents

1. Introduction

1.1 Motivation

The lithium ion battery has since its commercialization in the early 90's been at the frontier as a battery choice for small portable applications (like cell phones, iPad and iPod's). However, lithium ion batteries are also one of the more promising candidates for larger applications, like electric vehicles (EV's) and hybrid electric vehicles (HEV). Lithium metal has a very low density, which is very useful for large scale operations, as it provides for low volume and light weight batteries. Fig. 1.1 illustrates the benefits of lithium ion compared to other battery technologies in terms of energy density. Lithium metal is also among the more electronegative metals (-3.04 vs. H_2/H^+ [1]), meaning it can achieve very high open circuit potentials, leading to a high power output and increased energy density.

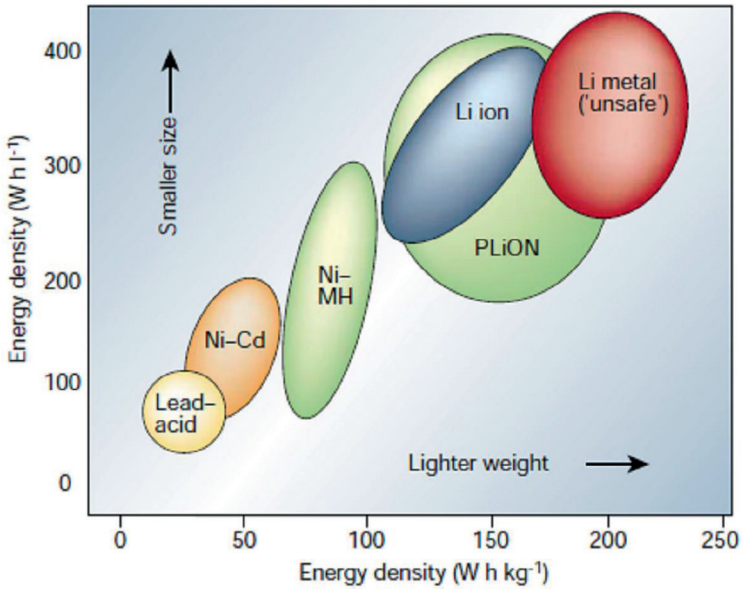

Figure 1.1. Volumetric and gravimetric energy density (for different battery technologies) [2].

The choice of anode material (defined during the discharge process) is more or less dominated by carbons. There are vast amounts of different carbon materials, all of which have slightly different properties. In addition, there are various ways to modify a carbon surface (i.e. by heat treatment or surface modifications) that to a large extent can tailor the material to either store large amounts of energy or be able to reversibly intercalate lithium at high rates. High rates would be very attractive with regards to use in EV's, as this would be very beneficial for faster charge and discharge.

The intercalation process in carbon is known to occur mainly through the edge and defect sites [3-5]. A higher fraction of edge planes would therefore be beneficial for higher charge rates, and there are clear experimental data indicating that a higher fraction of edge planes reduces the charge transfer resistance [6]. The downside is that a higher fraction of edge planes also causes a significantly higher irreversible capacity loss (ICL) due to increased electrolyte reduction and film formation [7]. In terms of achieving higher charge rates one must consider other factors as well, such as electrode porosity, electrode density (or loading), and particle size [8]. Knowledge of these factors, perhaps especially fraction of edge/defects would prove most valuable in the study of graphite electrodes for lithium ion batteries.

Selection of appropriate electrolytes is of vital importance when producing a full sized battery. The electrolytes can largely influence the batteries performance. Lithium salts dissolved in various ratios of organic components are usually utilized in full cell lithium ion batteries these days. A good electrolyte must have high conductivity and be stable in a wide electrochemical operating window. Carbons are generally not stable in these electrolytes at low potentials. Below a certain potential the electrolyte starts to decompose and form a film on the carbon surface which acts as a passivation layer and protects the carbon from further reactions with the electrolyte. This passivating film was termed the solid electrolyte interphase (SEI) in the late 70's [9]. The SEI is very important, both in the electrochemical performance, but also for the thermal stability of the lithium ion battery system. Ideally, it should behave like a solid electrolyte, meaning it should be both electronically insulating (to prevent further electrolyte reduction) and ionically conductive (to allow for fast lithium ion transport). The composition of the SEI can vary drastically depending on different parameters such as; formation conditions, surface properties of the graphite, and electrolyte composition. Therefore, the SEI is in the center of attention in most lithium ion battery research and it is perhaps one of the main reasons why these systems still can be so complex to study.

The challenge in the study of these materials lies in the extraction of important information about the surface properties and relating this to the electrochemical performance, and increasing the knowledge and understanding about the interplay between surface properties and electrolyte. The goal is to improve properties like low temperature performance, electrochemical performance, safety and thermal stability. These matters can all be related to the surface properties and electrolyte and the formation of the SEI.

1.2 Aim of work

When studying the thermal stability and electrochemical performance of graphite anodes in Li-ion batteries, it is natural to start by identifying important parameters that provide good electrochemical performance (long cycle life and high capacity) and improved thermal stability (high onset temperature for exothermic reactions) in the graphite material. With regards to cycle life the cell is generally considered dead after a capacity fade to about 80 % of initial nominal capacity [10].

Density functional theory (DFT) is a relatively new method which has been employed to investigate the ratio of edge/basal planes and defects on the surface of the graphite. The goal is to relate these parameters with their impact on the initial capacity loss and the formation of the protective film. Furthermore, there are few studies connecting these properties with thermal stability, which would be quite interesting to investigate as well. More specifically, the first part of the thesis aims to study the properties of various graphites with different surface morphology, and relate this to their electrochemical performance and their thermal stability. In order to investigate the thermal stability of the system differential scanning calorimetry (DSC) has been used.

The composition of the electrolyte can, in addition to surface properties, have a large impact on the composition and the properties of the SEI. This will affect the electrochemical performance and determine the long term stability of the graphite. For Li-ion batteries used in EV's it is also important that the system can handle temperature variations. With this in mind, the second part of the thesis aims to focus on various electrolyte choices and their effect on the electrochemical performance at various temperatures. DSC has also been employed here to determine the upper and lower operating temperature limits of the electrolytes.

The SEI seems to be involved in all parts of Li-ion battery research, be it thermal stability, long term cycling or high capacity. The composition of the SEI has been thoroughly studied by others, and with regards to the electrochemical performance it is generally considered that the SEI is very much involved in the capacity fade over time. Insufficient film formation with pore passivation properties and also continued growth of the SEI, would both lead to increased internal resistance in the cell. In the study of resistances and transport processes within a system, electrochemical impedance spectroscopy (EIS) is an excellent tool. However, since the impedance often have to fit data to equivalent circuits (EQC) in order to extract useful information, the challenge often lies in the choice of EQC. This is even more complicated for these systems due to the complex nature of the film formed on the electrode and the fact that the literature is much divided in their interpretation of impedance spectra. The last part of the thesis therefore aims to focus on the explanation of the EIS spectra observed in Li-ion batteries. The goal is to extract important parameters, like charge transfer resistance, electrolyte resistance, and film resistance and study how these resistances increase over time, eventually leading to capacity fade.

References

1. G. Aylward and T. Findlay, *SI Chemical data*. 5 ed. 2002: John Wiley & Sons Australia.
2. J.M. Tarascon and M. Armand, *Issues and challenges facing rechargeable lithium batteries.* Nature, 2001. **414**(6861): p. 359-367.
3. T. Tran and K. Kinoshita, *Lithium intercalation deintercalatation behaviour of basal and edge planes of highly oriented pyrolytic-graphite and graphite powder.* Journal of Electroanalytical Chemistry, 1995. **386**(1-2): p. 221-224.
4. Y. NuLi, J. Yang, and Z. Jiang, *Intercalation of lithium ions into bulk and powder highly oriented pyrolytic graphite.* Journal of Physics and Chemistry of Solids, 2006. **67**(4): p. 882-886.
5. A. Funabiki, M. Inaba, and Z. Ogumi, *A.c. impedance analysis of electrochemical lithium intercalation into highly oriented pyrolytic graphite.* Journal of power sources, 1997. **68**(2): p. 227-231.
6. Y. Yamada, K. Miyazaki, and T. Abe, *Role of Edge Orientation in Kinetics of Electrochemical Intercalation of Lithium-Ion at Graphite.* Langmuir. **26**(18): p. 14990-14994.
7. T. Placke, et al., *Influence of graphite surface modifications on the ratio of basal plane to non-basal plane surface area and on the anode performance in lithium ion batteries.* Journal of power sources, 2011. **200**(0): p. 83-91.
8. H. Buqa, et al., *High rate capability of graphite negative electrodes for lithium-ion batteries.* Journal of the Electrochemical Society, 2005. **152**(2): p. A474-A481.
9. E. Peled, *The Electrochemical-Behaviour of Alkali and Alkaline-Earth Metals in Non-Aqueous Battery Systems - The Solid Electrolyte Interphase Model.* Journal of the Electrochemical Society, 1979. **126**(12): p. 2047-2051.
10. *Handbook of Battery Materials*, ed. J.O. Besenhard. 1999: Wiley-VCH.

2. Lithium ion batteries

2.1 The lithium ion battery system

The lithium ion battery system consists of an anode and a cathode separated by a membrane soaked in electrolyte. Fig. 2.1 shows a typical discharge process. The anode and the cathode are defined during the discharge process, but be aware that upon charging the anode becomes the cathode and vice versa. During the discharge process, the lithium ions stored within the anode, are oxidized and move through the electrolyte towards the cathode. Here, they are subsequently reduced and stored within the material. At the same time a current moves through the outer circuit, which we are able to utilize. The charging process would then be the reverse of this process.

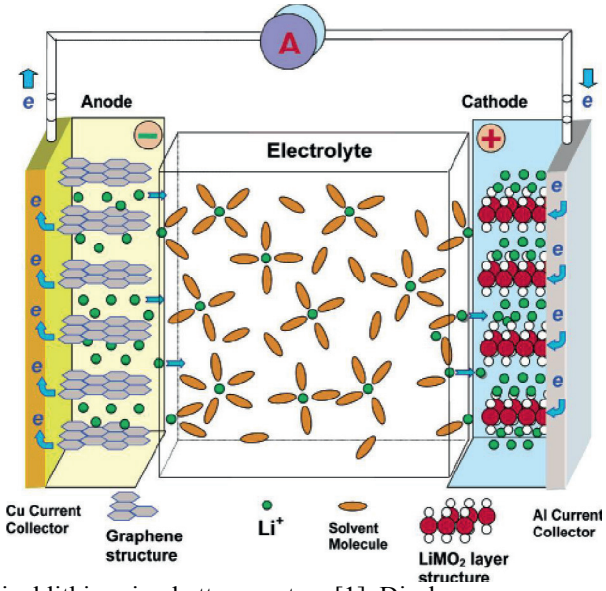

Figure 2.1. Typical lithium ion battery system [1]. Discharge process.

Lithium metal was initially used as anode material in lithium batteries in the early 90's. Lithium is very electronegative and light weight and therefore has the potential to store large amounts of energy per mass. The reason for converting to lithium ion was a decision mainly based on safety. When lithium re-deposited on the anode during charging, the formation was uneven. This was mainly due to an inhomogeneous surface causing uneven current densities leading to so-called dendrite formation. These dendrites could pierce the polypropylene/polyethylene membrane separating the anode and cathode, causing short circuit and possible exothermic reactions (thermal runaway). Lithium metal was then replaced by a material able to store lithium in its ionic form within the structure, such as carbon. By storing ionic lithium through intercalation into a

"host" material instead of storing lithium in metallic form, dendrite formation could be avoided, and safety improved.

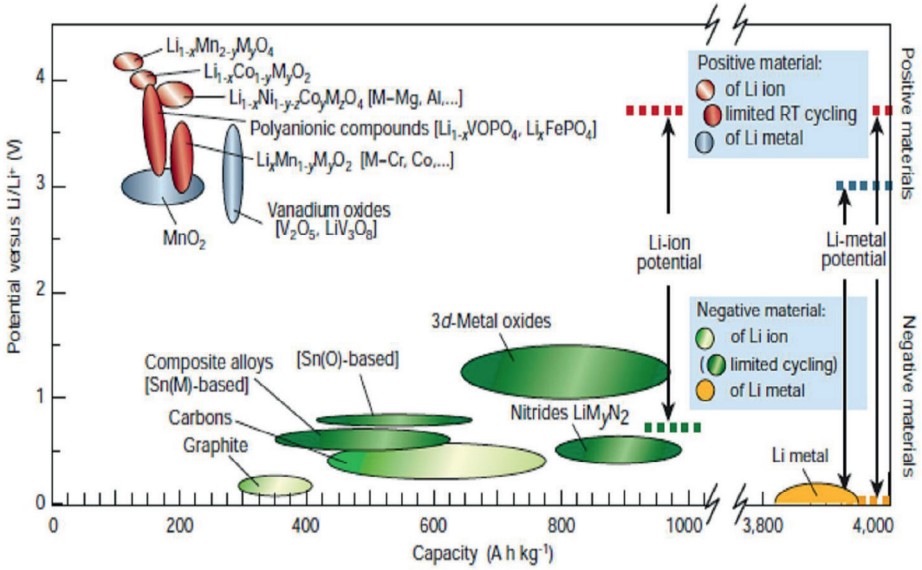

Figure 2.2. Potential vs. capacity for typical lithium ion anodes and cathode materials [2].

Fig. 2.2 gives an overview of the potential and capacity of some of the most typical anode and cathode materials used in lithium ion batteries. Notably, here the anode and cathode are defined as negative and positive electrode to avoid the confusion mentioned previously. A short introduction to anode, cathode, electrolyte, current collector and separator follows.

2.1.1 Anode materials

The anode usually is some sort of host material, capable of storing lithium ions in its structure. The most commonly used anode material in current lithium ion batteries is graphite due to low price and availability. Alternatives to carbon, considering price and availability, include tin (Sn) and silicon (Si) which both provide high volumetric capacities [3]. Si and Sn have the potential to achieve much higher capacities than graphite. Silicon thin films deposited on nickel substrate by chemical vapor deposition [4], showed capacities up to 1000 mAh/g during the 3 first cycles. However, poor stability was observed during the next cycles, related to mechanical disintegration. It is believed that the strain caused by large expansion upon intercalation is the reason for this poor stability. To remedy these high volume expansions and the capacity loss it was found that decreasing the particle size was beneficial for the performance [5]. Nanostructured silicon prepared by physical vapor deposition [6] showed capacities

around 1100 mAh/g with 50 % retention after 50 cycles. A silicon-carbon composite [7] also showed improved performance compared to graphite, with a reversible capacity of about 700 mAh/g and good cyclability. Additionally, it is noteworthy that the use of binders improved the cyclability of Si anodes [8]. However, no large commercialization of silicon anodes has been implemented yet.

2.1.2 Cathode materials

The cathode is normally a lithium-containing species such as spinel structures (e.g. $LiMn_2O_4$), layered oxides (e.g. $LiCoO_2$) and more open structures (e.g. $LiFePO_4$). Although many types of cathode materials have been investigated much of the research can be summarized into two main categories [9]. These are 1) Layered oxides and spinels (like $Li_xNi_{1-y-z}Mn_yCo_zO_2$ and $LiCoO_2$) and 2) open structures like vanadium oxides and olivine $LiFePO_4$. In the latter group, Li_2FeSiO_4 [10] and Li_2MnSiO_4 [11] have received some attention the past 7-8 years with promising results.

The first big commercialization of lithium ion batteries came when Sony bought the Goodenough patent on $LiCoO_2$ [12] in the early 90s and used it to make $LiCoO_2$/coke batteries. This same basic system is still in use today in most cell phone batteries but capacity and performance has increased since then.

One of the most used cathode material these days are NMC ($Li_xNi_{1-y-z}Mn_yCo_zO_2$) and lithium rich NMC based on these layered oxides. In NMC each component adds something beneficial and the combination of nickel, manganese and cobalt seems to complement each other. Obviously the amount of lithium increases the overall capacity but studies have shown that more lithium in the structure also minimized the effect of Jahn-Teller distortions due to the fact that more lithium caused the lattice parameter to decrease and force manganese to want to be closer to its (4+) oxidation state rather than its (3+) oxidation state [13]. The nickel in NMC is generally considered the electroactive member, while manganese stabilizes the lattice and cobalt is mainly ordering the transition metals (but can also increase rate capability and conductivity) [9]. Manganese dissolution has been the main cause of degradation as it can dissolve irreversibly into the electrolyte which causes structural instability. Manganese can also diffuse to the anode side and become incorporated into the solid electrolyte interphase film, increasing the electronic conductivity, causing further SEI growth (and consequently capacity loss).

2.1.3 Electrolytes

Normal proton based electrolytes cannot be used with lithium ion batteries due to the wide operating electrochemical window (usually 0-4.5 V vs. Li/Li^+) [1]. The electrolyte most commonly used is therefore a mixture of organic solvents and inorganic species (lithium salts). Even with the use of these solvents there is still a need for the formation of a protective film on graphite to further increase the window of electrochemical stability [14]. The solvents most commonly used are cyclic carbonates, like ethylene

carbonate (EC) or propylene carbonate (PC), in combination with a linear carbonate, like ethyl methyl carbonate (EMC), dimethyl carbonate (DMC) or diethylene carbonate (DEC). The most commonly used lithium salt in commercial batteries has been $LiPF_6$, due to its overall good properties [1]. Fig. 2.3 shows the molecular formula for these solvents together with the most commonly used additive, vinylene carbonate (VC).

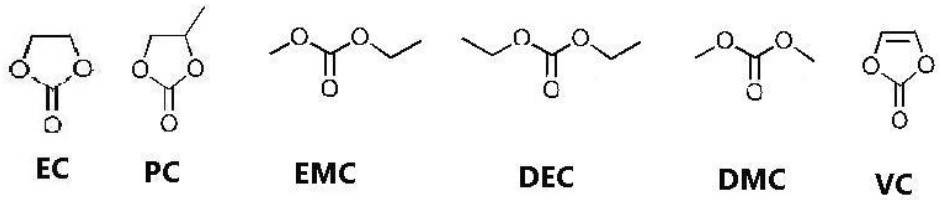

Figure 2.3. Molecular formula for ethylene carbonate (EC), propylene carbonate (PC), ethyl methyl carbonate (EMC), diethylene carbonate (DEC) and the most commonly used additive, vinylene carbonate (VC)

The reason for mixing linear and cyclic carbonates is to, among other things, compromise between the solubility of the salt and conductivity of the solution. EC and PC have a high dielectric constant (very polar) and are very good with regards to the solubility of the ionic salts in the electrolyte. However, EC and PC have a high viscosity, causing decreasing conductivity of the solution. Low viscosity solvents like EMC, DMC and DEC are therefore added to improve properties like conductivity, wettability and low viscosity. These solvents also have additional parameters to consider. With regards to safety the flash points of the respective solvents become important. The flash point is the temperature at which an external heat source could ignite the electrolyte and therefore is a very important parameter to consider when developing new electrolytes for lithium ion batteries. Table 2.1 summarizes some of the properties of these organic solvents.

Table 2.1. Properties of some organic carbonates [1]

Solvent	T_m (^oC)	T_b(^oC)	T_f(^oC)	η (viscosity) 25 ^oC	ε (dielectric constant) 25 ^oC
EC	36.4	248	160	1.90 (40^oC)	89.78
PC	-48.8	242	132	2.53	64.92
DMC	4.6	91	18	0.59 (20 ^oC)	3.107
DEC	-74.3	126	31	0.75	2.805
EMC	-53	110	-	0.65	2.958

Here T_m, Tb and T_f denote melting point, boiling point and flash point, respectively.

With regards to additives there are many options. The main function of these additives would be to facilitate a good SEI formation, reduce capacity losses, improve thermal stability and prevent dissolution on the cathode [15]. Studies on the first electron reduction reported that the most commonly used solvents were reduced in the order, EC>PC>VC>DMC>EMC>DEC, and the second electron reduction VC>EC>PC [16].

There seems to be a close link between the potential at which solvents undergo reduction and the electron affinity (EA). It is therefore natural that EA is an important parameters to consider with regards to development of new SEI forming additives [17].

2.1.4 Current collector

The electrolyte used in lithium ion batteries (LIB) demands a certain stability in terms of the choice of current collector. Based on price and stability in the given potential regions the natural choice and most used current collector today are Cu for the negative electrode and Al for the positive electrode. Cyclic voltammograms of Al and Cu in a typical LIB electrolyte system show that Cu experiences high current densities at high potentials vs. Li/Li^+ (around 3.3 V vs. Li/Li^+), which is believed to be related to oxidation and dissolution of Cu, and that Al has very small current density in the same region, which is related to formation of a good passivating oxide film, protecting against oxidation [18]. At low potentials vs. Li/Li^+ (close to 0 V vs. Li/Li^+), Al shows very high current around 0 V vs. Li/Li^+ related to Li and Al alloying. Cu shows no large currents in this region. Studies of electrochemical behavior and passivation of current collectors for use in lithium ion batteries was recently reviewed [19].

2.1.5 Separators

The main purpose of the separator in a lithium ion battery is first of all to prevent direct contact between the two electrodes, so as to avoid a short circuit, and at the same time provide good conductivity across. In addition, it is important that it remains stable towards the electrolyte components and temperature variations (high chemical and thermal stability). Throughout this thesis the choice of separator has remained constant since any investigations of separator are beyond the scope of these studies. A microporous trilayer membrane (PP/PE/PP) from Celgard (Celgard 2320) was selected. This separator has a thickness of about 20 μm and a porosity of 39 %.

2.2 Carbon

Carbon has the potential to form many different types of bonds (sp, sp^2 and sp^3 hybridization), and can therefore exist in several structures. The most common allotropes of carbon are diamond, fullerenes and graphite. Even though carbon nanotubes have shown some promise with higher capacities than graphite (possibility of LiC_2, which theoretically would mean capacities of 1116 mAh/g), they suffer from high irreversible capacity and a poor voltage profile [20]. Graphite therefore remains the most used and relevant allotrope with regards to electrode material for lithium ion batteries.

2.2.1 Properties of graphite

In graphite carbon has sp^2 (tetrahedral) hybridization which gives it a layered structure where the carbon layers are stacked in sequence. If the sequence is ABAB, then the graphite takes the crystallographic form of *hexagonal* graphite (Fig. 2.4). The surface perpendicular to the c-axis is commonly called the basal plane, while the surface parallel to the c-axis is called edge plane (or prismatic surface). The electronic properties of edge and basal surfaces are quite different, which will influence the electrochemical reactivity [21]. An ABCABC stacking gives a *rhombohedral* graphite. The bonds between the atoms are of both covalent and metallic character within each layer. The layers are linked by a weak van der Walls interaction produced by a delocalized π-orbital. The distance between C-C bonds is 1.42 Å with an interplanar distance of 3.354 Å [21]. In addition, we also have an *amorphous carbon* form which is similar to graphite in bonding and structure, but have no *long range order*. Graphite is anisotropic meaning it is a good electrical and thermal conductor within the layers, but poor electrical and thermal conductor perpendicular to the layers (this is due to the weak van der Walls bonding and no orbital overlap to form a partly filled conduction band) [22]. This anisotropic behavior makes graphite a good candidate for intercalation compounds, such as in lithium ion batteries.

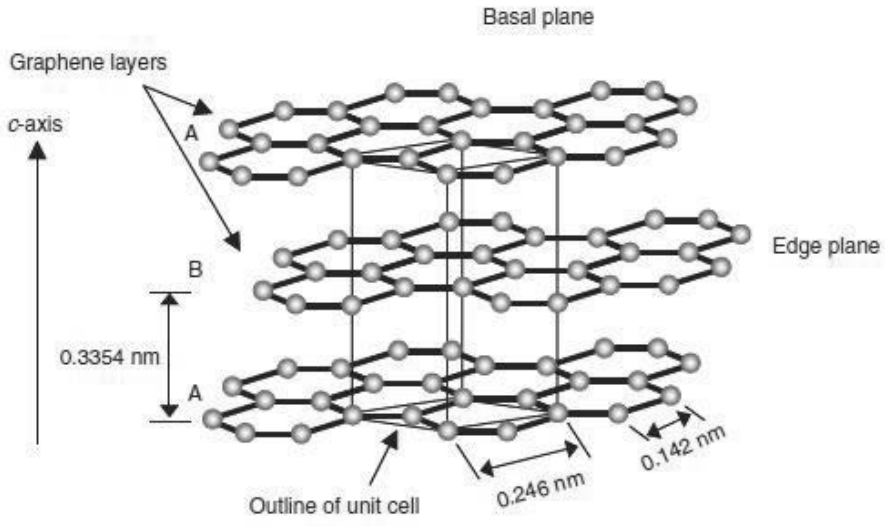

Figure 2.4. Crystal structure of hexagonal graphite. Modified from [23].

2.2.2 Graphite as anode material in lithium ion batteries

Graphite is most used as anode material in lithium ion batteries due to a relatively high reversibility (theoretical capacity of 372 mAh/g). Carbon materials that are able to reversibly store lithium in its structure are often divided into "graphitic" and "non-graphitic" [24]. They both have the basic bonding and structure of graphite, but graphitic is more ordered (long range order) while non-graphitic carbon has no long range order. The difference between non-graphitic and amorphous carbon is that non-graphitic still contains areas with crystalline phase linked together by amorphous phases. Non-graphitic can be further divided into hard and soft carbons. The difference between hard and soft carbons is their ability (or inability) to reform the structure and crystallize upon heat treatment. Hard carbons cannot reform the crystal structure due to the cross-linking between crystalline areas effectively inhibiting any reformation. Soft carbons on the other hand can crystallize and, if heat treated to around 3000 ^{o}C, will achieve an almost perfect crystalline structure. Most carbon materials will contain both graphitic and non-graphitic structures, but the most important difference (and most observable difference) is the charge/discharge behavior, which is explained further in a separate section.

2.3 Intercalation and exfoliation

Eq. 2.1 shows the general electrochemical reaction for lithium intercalation.

$$xLi^+ + C_n + xe^- \leftrightarrow Li_x{}^+C_n{}^- \quad (2.1)$$

When lithium ions approach the carbon surface, electrons from the current source reduces the carbon host, making them slightly negative [25]. The lithium then positions itself between the hexagonal graphite sheets in the carbon to maintain charge neutrality. Upon intercalation the graphite crystal structure goes from AB (hexagonal) to AA stacking [26, 27]. Notably, studies on highly oriented pyrolytic graphite (HOPG) shows that intercalation occurs mainly through the edge site and that intercalation through basal planes occurs mainly on defect sites [28-30].

Lithium graphite intercalation compounds (Li-GIC), as they are commonly called, faced a few challenges in the beginning. Propylene carbonate (PC), which was a very commonly used electrolyte, would cause destruction of the carbon at around 0.8 V vs. Li/Li^+ (exact voltage is determined mainly by the carbon surface and charge current), leading to a physical disintegration [31]. This destruction of carbon with PC was termed "exfoliation" [32-37]. Exfoliation can also lead to delamination between the carbon material and the current collector, making them inactive with regards to lithium storage (causing significant capacity loss), and is very common in PC based electrolytes [38]. A very important discovery was made in the early 90's, when they found that ethylene carbonate (EC) could replace PC as electrolyte, and thereby form a passivating film which protected the graphite from further exfoliation [39]. This surface film was originally termed solid electrolyte interphase (SEI) by Peled [40] (who first described this film forming on alkali and alkaline earth metals in a non-aqueous lithium battery system and its resulting effect on the kinetics).

In graphite, the reasons for the different behavior between EC and PC have been attributed to the extra methyl group in PC causing additional strain between the graphite sheets since PC is a species very similar to EC on a molecular level [41]. Besenhard et.al [42] studied the film formation on graphite anodes in lithium ion batteries and proposed a mechanism for exfoliation of graphite by solvent co-intercalation (and consequent decomposition) in EC containing electrolyte. Electrolyte species would co-intercalate during the first lithiation cycle, forming so called graphite intercalation compounds (GIC), whose formation would cause huge expansion in the graphite matrix and consequently cause exfoliation. In the same process the reduced electrolyte species would also form a protective layer (or film) which prevented further co-intercalation after the initial cycle.

Aurbach et.al found that this mechanism of co-intercalation was accurate for ether based solutions [43], but they discovered (or proposed) that the mechanism was different for PC based electrolytes and claimed that the electrolyte decompositions occur more in cracks and crevices [44].

During lithium intercalation into the graphite structure, the space between the graphene layers has to expand in order to give room for the intercalated lithium ion. The interlayer distance between the layers in graphite is typically around 0.33 nm [21], and XRD studies of lithium intercalated graphite [45] show how the interlayer distance increases upon intercalation. DFT studies on the ternary GIC energy for EC and PC [46] show how lithium solvated by only EC would require an intermolecular distance of about 0.69 nm. Lithium ions solvated with PC would require around 0.85 nm. This would mean an expansion of over 100% in order for the lithium intercalation compounds to fit in the graphite structure. The difference in Li-GIC's radius of solvated EC vs. PC is very interesting and could go a long way in explaining why EC causes considerably less exfoliation of graphite compared to PC. GIC takes up a lot of space during the initial film formation process according to Besenhards model [42]. However, it is generally accepted that after this initial film formation process, intercalation occurs only *after* the GIC has removed its solvation sheath. This process is commonly termed de-solvation and is believed to be among the main contributors to the overall activation energy [47-51]. High-resolution transmission electron microscopy (HRTEM) and X-ray diffraction (XRD) studies of the microstructure of intercalated graphite (LiC_6)[52] showed a lattice constant of about 3.7 Å (0.37 nm), indicating an expansion of around 10 %.

2.3.1 Charge/discharge characteristics

The charge/discharge characteristics are very different for graphitic and non-graphitic structures. Upon intercalation of lithium ions into a graphitic structure, the lithium ions position themselves between the carbon layers, causing expansion accompanied by a phase transition from AB (hexagonal) /ABC (rhombohedral) stacking to AA stacking [26, 27], as previously mentioned. In a typical galvanostatic curve during intercalation, it can be observed that the voltage remains constant for a long period of time during constant current at several different potentials, producing voltage plateaus (Fig. 2.5). This phenomenon is called "staging" [24] (initially proposed by Besenhard [34]) and is a thermodynamic effect that is mainly attributed to two things; Van der walls expansion of the graphene layers [53] and lithium-lithium interactions. "Staging" is therefore very typical for carbons with high degree of graphitization. XRD studies of lithium intercalated graphite [45] also show how the interlayer distance follow the theory of stage formation in GIC.

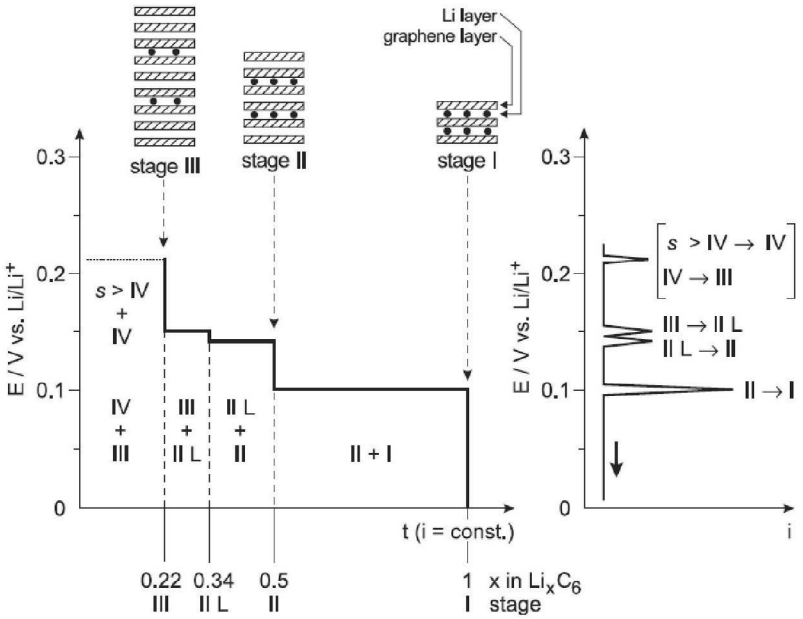

Figure 2.5. Stage formation during intercalation of graphite. Galvanostatic curve (left) and Voltammetric curve (right). Obtained from [24], which is a reproduction from Besenhard [34].

As mentioned previously, non-graphitic carbon is usually divided into soft (graphitizable) and hard (non-graphitizable) carbons, and they both have different voltage profiles compared to graphite. The most recognizable difference is that they have no voltage plateaus, which is a characteristic of the "staging" phenomenon. Soft carbons (like turbostratic carbons and cokes) generally exhibit lower capacities compared to what is theoretically achieved in pure graphite (372 mAh/g). However, upon heat treatment they show characteristics that become increasingly similar to graphite and "staging" [54].

Some carbonaceous materials also show capacities higher than that of graphite [55-58], which would suggest a different model of lithium storage. In Fig. 2.6 the differences between the charge/discharge characteristics for synthetic graphite, petroleum pitch (soft/hard carbon but with high hydrogen content) and resole resin (hard carbon) are presented [58].

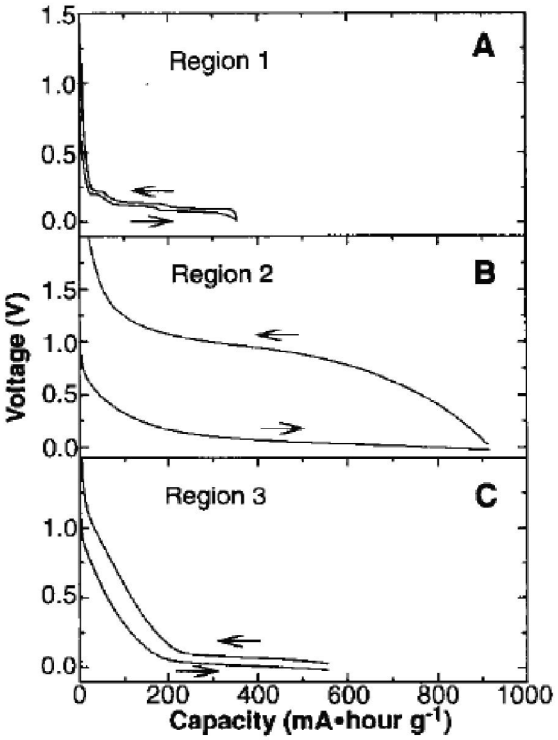

Figure 2.6. Reprinted from [58]. Second charge/discharge cycle with; (A) Synthetic graphite; (B) Petroleum pitch; and (C) Resole resin

Synthetic graphite (Fig. 2.6A), which in this case is soft carbon heat treated to above 2400 ^{o}C, shows voltage plateaus characteristic of "staging". The staging is not as abrupt as the galvanostatic curve in Fig. 2.5, but more smooth in its transition between the different stages. This arises mainly from the fact that some carbon particles provide faster (or slower) intercalation than others, so that we have no clear transition where every particle is at a certain stage (phase distribution).

The petroleum pitch (Fig. 2.6B) shows a large hysteresis in the voltage vs. capacity curve. This hysteresis was thoroughly studied [55, 59-61] and related to the hydrogen content. A clear correlation with increased reversible charge and hydrogen content was observed. It was suggested that high hydrogen content would allow lithium to bind in the vicinity of these hydrogens in the hydrogen containing carbons and change the bond structure [55, 58, 60].

The hard carbon (resole resin) (Fig. 2.6C) has a relatively large reversible capacity, but a low flat potential plateau, very close to the lithium potential, which suggests weakly bonded lithium [58].

There are several models suggesting possible mechanisms for lithium storage above the theoretical value for graphite. To explain the behavior of hard carbon in Fig. 2.6C, a "house of cards" model was suggested [62]. Here it is proposed that lithium is adsorbed on both surfaces of single sheets, allowing for more lithium storage. Another study suggested the existence of covalent Li_2 molecules in the carbon structure [56]. The discovery that mild oxidation of synthetic graphite increased performance was suggested to be due to improved SEI formation and accommodation of extra lithium at the zigzag and armchair edges and nanovoids [63, 64]. A model somewhat similar [65], suggested that lithium is doped at the edge of the graphitic layers, and on the surface of the crystallites. Another possible explanation for the accommodation of extra lithium was in the study of the high capacity of heat treated phenolic resin, which was able to intercalate up to C_2Li. This was attributed to a higher interlayer distance of 3.7-4.0 Å [57]. In conclusion, there are many possible explanations for the accommodation of lithium above the theoretical value of graphite. It seems that the literature is somewhat divided on the matter.

2.4 Solid electrolyte interphase

The choice of electrolyte can have a major impact on the batteries' performance, not only because of difference in conductivity and wettability, but also due to the properties of the solid electrolyte interphase (SEI). The two most important properties of a good SEI film are: 1) electronically insulating (prevent further reduction) 2) ionically conductive (allowing lithium ions to pass through). The SEI is known to mainly consist of decomposed species from the electrolyte [66] and consequently the composition of the SEI is very electrolyte dependent. In addition, the SEI will also have different properties depending on the formation conditions, like charge current and temperature [67], and it can also be sensitive to the actual graphite surface. XPS studies show that the thickness and composition of the SEI is very different on the basal planes compared to the edge planes of graphite [68]. The SEI on edge planes is generally thicker and also consists of more inorganic compounds than on the basal planes. Thickness of the SEI film was measured with atomic force microscopy (AFM) [69] to be about 250 Ångstroms, but the thickness is determined by the electron tunneling range [40]. Therefore, reported values can typically be between twenty to several hundreds of Ångströms [70]. The properties of the SEI also appear to change with degree of lithiation of the graphite. XPS analysis has shown that the SEI is dynamic in its behavior [71] . After 3 cycles of operation the SEI, in its de-lithiated state, was thicker and contained more Li_2CO_3 or semi-carbonates compared to a sample in a lithiated state.

There have been numerous studies investigating the species involved. This has been reviewed recently [72], and will be, together with some of the main properties of the SEI, discussed in more detail in the following sections.

2.4.1 Irreversible capacity loss

The irreversible capacity loss (ICL) during the first cycle of operation has also been related to the SEI and its thickness. The main mechanism leading to ICL is assumed to be capturing of lithium ions in the SEI during formation, rendering certain active areas of the graphite unavailable for lithium intercalation. It is commonly believed that the SEI is mainly formed *during the first cycle* and continues to grow during operation. However, a study investigating the growth rate after initial SEI formation with a high precision coulometry [73] found that the SEI grows as a function of $t^{1/2}$, independently of number of cycles (this assumes we are at a potential where electrolyte reduction occurs, around 0.25 V vs. Li/Li^+).

The SEI also seemed to grow faster with increasing temperature and the charge consumption during formation was larger for materials with a higher surface area. This means that the main factor influencing the amount of SEI and continued growth is the actual surface area of the graphite. Studies have showed a linear relationship for the formation of SEI and ICL with the total surface area [74], as measured by BET

(Brunauer, Emmet, Teller) [75]. An increase in surface area would lead to an increase in ICL, and thereby an increase in SEI thickness. Recently there has been more focus on the amount of edge planes vs. basal planes in graphite and its effect on the ICL [76], as it is the edge planes (and defects) that are believed to be more active sites with regards to SEI formation.

2.4.2 Composition and mechanism

The SEI consists of many different species which can be divided into two main categories:

1) Inorganic compounds, like LiF and Li_2CO_3. LiF is mainly a salt reduction product ($LiPF_6$, $LiBF_4$ and $LiAsF_6$), but can also be formed due to reactions of impurities in the electrolyte (like trace amounts of H_2O) with the initially formed film [77, 78]. Li_2CO_3 is a possible reduction product of EC/PC, but it can also be formed upon storage by reaction with the initially formed film with trace H_2O [79]

2) Organic compounds (semi-stable) like lithium-alkyl carbonates and lithium semi-carbonates formed by either a two electron reduction of the solvents, or single electron reduction, followed by a radical termination [80].

The reduction of EC is proposed to have a reaction mechanism as given in Fig. 2.7 [15].

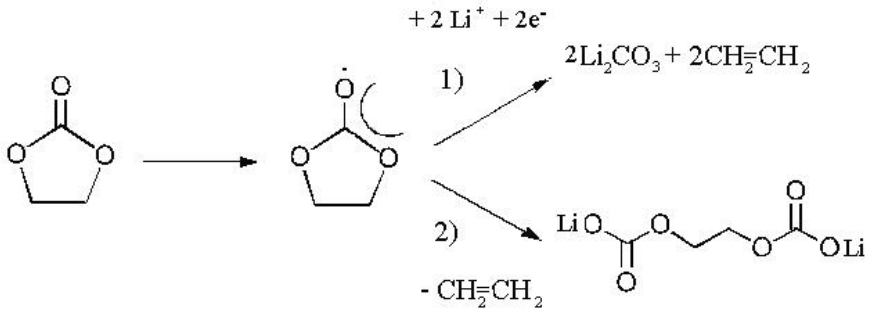

Figure 2.7. Reduction mechanism for EC.

EC is reduced, in a ring opening process, to a radical anion (RA) with two further possible reaction paths. Reaction path 1 produces an abundance of Li_2CO_3 and ethylene gas formation (for PC reduction this would be propylene gas). Reaction products of reaction path 2 provide more organic compounds. Whether reduction of EC/PC follows path 1 or 2 is largely dependent on the graphite surface, as studies on SEI composition on graphite have shown that the SEI on basal planes consists mostly of organic species, while on the edge planes there are more inorganic species, like Li_2CO_3 [68]. It is also

noteworthy that EC reduction was found to occur at two different voltage stages [67, 81]. The first reduction occurred before the first lithium intercalation, creating a highly resistive film and a more porous structure with an SEI composition consisting of inorganic components [15]. The second reduction occurs at about the same voltage as with lithium intercalation, yielding a highly conductive SEI consisting of more organic components [15]. The first reduction therefore fits well with reaction path 1, while the second fits well with reaction path 2. This is reasonable as the two electron reduction is more likely to occur before any film is present, as the film would increase the tunnelling distance for the electrons, making reaction path 2 more competitive [80].

The most typical lithium ion *additive*, vinylene carbonate (VC), actually works such that it deactivates the catalytic sites, preventing reaction path 1 from occurring, followed by incorporation into the SEI at lower voltages vs. Li/Li^+ (in effect promoting reaction path 2).

Since the SEI is formed in this stepwise manner it is natural that the SEI consists of layers with different chemical composition and morphology which is very dependent on the solvent used [82]. Fig. 2.8 [70] illustrates how the SEI generally consists of a dense inorganic layer close to the surface with a porous organic layer further out.

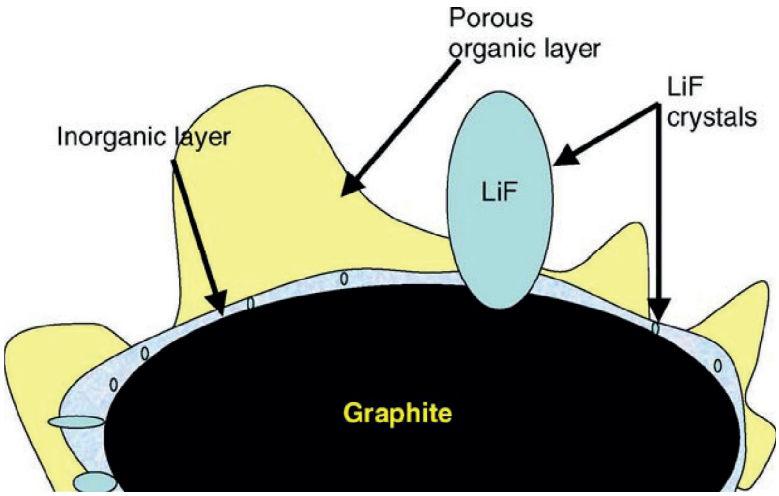

Figure 2.8. General SEI composition [70].

Ionic conduction in the SEI occurs through migration of lithium ions in the pores. A more porous structure will therefore have far lower resistance and increased conductivity of lithium ions. An SEI consisting of more organic components will therefore have far better conductivity than one consisting of only inorganic species. $(CH_2OCO_2Li)_2$, Li_2CO_3, Li_xSO_y, Li_2O, CH_3OLi and CH_3OCO_2Li are considered good passivating agents due to their compactness and polar nature [43]. The common

attribute for these in addition to their polar nature, is good adhesion to the graphite surface, which also makes it easier to adhere to other adsorbed species. Notably, Li_2CO_3 is considered an excellent passivation agent for graphite electrodes in lithium ion batteries. CO_2 can also be used as *additive* to increase the amount of Li_2CO_3, which have also showed to improve performance [38].

There is an adverse relationship between lithium conductivity and SEI stability. A high conductivity (low resistance) SEI will in general be less passivating than a lower conductivity (high resistance) compact passivation layer. The presence of Li_2CO_3, although beneficial for the film passivation, will cause resistance increase. Presence of LiF will also increases the interfacial resistance due to low lithium ion-conductivity compared to the carbonates [83].

During ageing of these surface films formed in alkyl carbonates, it is believed that more LiF will form gradually [79]. XPS studies of LiF during cycling showed that the amount increased until reaching a steady state around 50 cycles [71]. Resistance increase in the SEI (e.g. by increased amount of Li_2CO_3 or LiF) could eventually inhibit the transport of lithium ions from electrolyte to the interior of the graphite particle. Growth and resistance increase of the SEI, are together with micro-exfoliation, considered the main reasons why lithium battery capacity fades with time.

2.4.3 SEI composition as a function of temperature and current density

The chemical composition of the SEI is known to change at elevated temperatures. An XPS study [83] of the SEI at elevated temperatures showed that for electrolytes containing the lithium salt, $LiPF_6$, the amount of LiF increased with storage temperature. Li_2CO_3 is also believed to be formed at elevated temperatures due to conversion of meta-stable species, like lithium alkyl carbonates and semi-carbonates [84].

The formation of SEI at different temperatures was studied to optimize the formation conditions with regards to temperature and current [85]. SEI formation at elevated temperatures and high current densities resulted in a more porous (due to increased dissolution of the preliminary formed SEI), though highly conductive, SEI that would be less stable (with regards to self discharge etc). Consequently, formation at low temperatures and low current densities yielded a more compact SEI which is highly resistive and has poor conductivity.

The optimal conditions were found to be a charging current of about 10-20 mA/g and a temperature of 20-35 ^{o}C. However, it is important to stress that this was for one specific system, and other carbon types and electrolyte systems may have other optimal conditions for initial SEI formation.

2.5 Solvation sheath and de-solvation energy

When lithium ions move through the electrolyte, they are solvated by electrolyte species. After the initial film formation, it is generally accepted that the solvated lithium ion are required to de-solvate before intercalation can occur, which is the process where the lithium ion is separated from the electrolyte species to which it is associated. The de-solvation energy will most likely contribute to the overall resistance with regards to the lithium ion transport. In the literature there has been some recent studies investigating the contribution of "de-solvation" to the total charge transfer resistance in impedance data [47-51]. The easier it is for a solvated lithium ion to de-solvate, the lower the contribution to the overall resistance of the system.

In Fig. 2.9 the amount of EC, in EC/DMC and EC/EMC systems, is studied as a function of the solvation energy [47]. The figure clearly shows how the amount of EC in the electrolyte increases the activation energy for de-solvation. It stabilizes at 40 % EC where there is enough EC in the solution to completely solvated all the lithium ions.

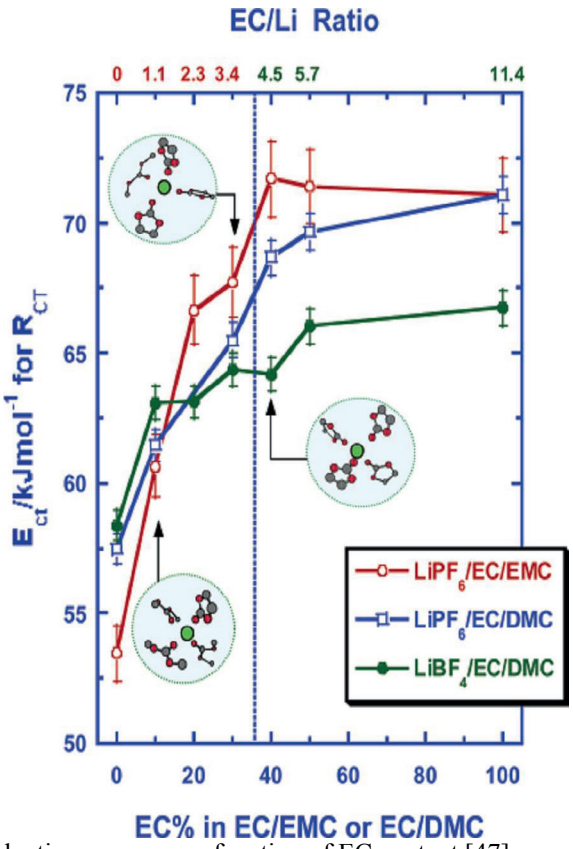

Figure 2.9. De-solvation energy as a function of EC content [47].

The behavior observed in Fig. 2.9 can be explained by the fact that, as long as there is sufficient amounts of EC molecules in the solution to completely solvate every lithium ion, the de-solvation energy will be higher due to the stronger affinity of EC towards lithium compared to the linear carbonates. This is related to the higher dielectric constants of the cyclic carbonates compared to the linear carbonates (see Table 2.1). This in turn means that it is possible to manipulate the contribution to the overall resistance from the de-solvation process simply by adjusting the amount of cyclic carbonates in the electrolyte composition. In an attempt to lower the de-solvation energy it was found that the presence of counter ions facilitated the de-solvation process, decreasing the overall resistance [46].

Since the de-solvation energy is assumed to be one of the major energy consuming steps, the lithium binding energy emerges as an important parameter to consider in the search for new additives [86].

2.6 Surface groups and active surface area

Surface groups and active surface area (ASA) can potentially have a major impact on the performance of graphite in lithium ion batteries. Surface groups and ASA can influence the SEI formation and consequently will be responsible for ICL and exfoliation.

Exfoliation was initially believed to be related to crystal structure, as studies saw a beneficial effect of high amounts of rhombohedral stacking defects suppressing exfoliation [87, 88]. A study with heat treatment (HT) of graphite in helium showed a decrease in the amount of rhombohedral stacking defects and achieved a perfect hexagonal structure [89]. This graphite experienced exfoliation and ICL during the first cycle of operation, consistent with the decrease in amount of rhombohedral phase. However, upon HT in an oxidizing atmosphere, which preserved the same crystal structure, the exfoliation and ICL decreased gradually with increasing oxidation temperature. The main conclusion from this is that the rhombohedral stacking faults seemed to have no direct influence on the exfoliation, and that exfoliation is governed by graphite surface properties and not the crystal structure. Notably, the crystal structure can still have an indirect influence by affecting the surface morphology and defects

The attention was therefore directed towards the role of graphite surface group chemistry and its effect on exfoliation and ICL. Acidic surface groups, obtained by prolonged ageing in humid air, seemed to be very beneficial with regards to reducing exfoliation and ICL [90]. Amount of rhombohedral stacking was again showed not to have any significant impact. The decreased exfoliation effect observed by ageing can be explained by introducing a new term, the active surface area (ASA). The ASA is the cumulated surface area of the different types of defects present at the carbon surface (stacking faults, single and multiple atoms, vacancies, dislocations) [91]. Active surface area is usually determined by chemisorption. The process is initiated by adsorbing oxygen species on the surface and then removing these species by HT connected to a mass spectrometer that measures the amount of CO and CO_2 desorbed. The surface area occupied by oxygen atoms can then be calculated.

HT of graphite SLX 50 increased the structural ordering significantly, and ASA measurements showed that this value consequently decreased [92]. A low ASA value caused poor passivation and a high ASA was indentified as an important parameter with regards to surface passivation. In addition, a high ASA value allowed the surface passivation (electrolyte reduction) reaction to occur at more positive potentials. This ensures that the surface is passivated long before one reaches the potentials where exfoliation reactions occur.

Based on these discoveries, a thorough study of the surface properties of graphite in relation to ASA and exfoliation was conducted [93]. The main conclusions were that there seemed to be an ASA threshold around 0.2 m^2/g, which need to be surpassed in order to form a good protective film. Beyond this threshold the presence of oxygen groups at the surface improved the SEI formation and prevented further exfoliation.

The graphite atoms on the edge planes are considered more reactive since they have unpaired electrons able to form bonds with oxygen. As the reactivity of oxygen surface groups and ASA are important for an effective SEI formation, this essentially means that ASA is correlated with the edge plane reactivity [94]. With this in mind the newest addition to these studies has been nitrogen adsorption measurements evaluated by DFT to estimate the amount of edge/basal planes [76, 95, 96]. A recent study investigated the difference between mild and strong oxidation using this technique [76]. By evaluating the amount of edge/basal planes and defect in the graphite as a function of oxidation temperature they were able to suggest a mechanism explaining why oxidation up to 580 ^{o}C decreased the amount of edge/defects. However, above 580 ^{o}C they observed a further increase in amount of edge planes. Fig. 2.10 shows how this could work by a difference in mild and strong oxidation. The mild oxidation only "attacked" defect and edge sites, while the strong oxidation above 580 ^{o}C "attacked" the basal planes. This left behind large pores which increased the amount of edge planes once again.

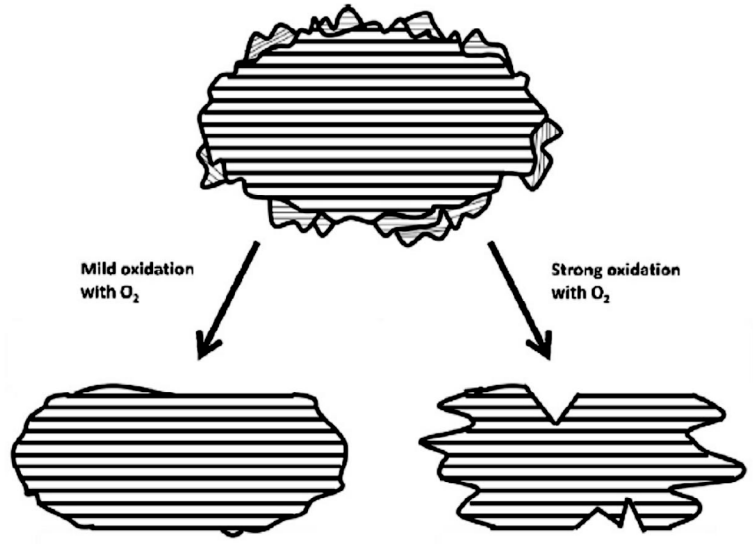

Figure 2.10. Mild and strong oxidation scheme adapted from [76].

References

1. K. Xu, *Nonaqueous liquid electrolytes for lithium-based rechargeable batteries.* Chemical reviews, 2004. **104**(10): p. 4303-4417.
2. J.M. Tarascon and M. Armand, *Issues and challenges facing rechargeable lithium batteries.* Nature, 2001. **414**(6861): p. 359-367.
3. D. Larcher, et al., *Recent findings and prospects in the field of pure metals as negative electrodes for Li-ion batteries.* Journal of materials chemistry, 2007. **17**(36): p. 3759-3772.
4. S. Bourderau, T. Brousse, and D.M. Schleich, *Amorphous silicon as a possible anode material for Li-ion batteries.* Journal of power sources, 1999. **81**: p. 233-236.
5. M. Winter and J. Besenhard, *Electrochemical lithiation of tin and tin-based intermetallics and composites.* Electrochimica Acta, 1999. **45**(1-2): p. 31-50.
6. J. Graetz, et al., *Highly Reversible Lithium Storage in Nanostructured Silicon.* Electrochemical and solid-state letters, 2003. **6**(9): p. A194-A197.
7. J. Yang, et al., *Si/C Composites for High Capacity Lithium Storage Materials.* Electrochemical and solid-state letters, 2003. **6**(8): p. A154-A156.
8. W.R. Liu, et al., *Enhanced cycle life of Si anode for Li-ion batteries by using modified elastomeric binder.* Electrochemical and Solid State Letters, 2005. **8**(2): p. A100-A103.
9. M.S. Whittingham, *Lithium batteries and cathode materials.* Chemical reviews, 2004. **104**(10): p. 4271-4301.
10. A. Nytèn, et al., *Electrochemical performance of Li2FeSiO4 as a new Li-battery cathode material.* Electrochemistry Communications, 2005. **7**(2): p. 156-160.
11. R. Dominko, et al., *Structure and electrochemical performance of Li2MnSiO4 and Li2FeSiO4 as potential Li-battery cathode materials.* Electrochemistry Communications, 2006. **8**(2): p. 217-222.
12. K. Mizushima, et al., *LixCoO2 (0<x<-1): A new cathode material for batteries of high energy density.* Materials Research Bulletin, 1980. **15**(6): p. 783-789.
13. J.M. Tarascon, et al., *The Spinel Phase of LiMn2O4 as a Cathode in Secondary Lithium Cells.* Journal of the Electrochemical Society, 1991. **138**(10): p. 2859-2864.
14. J.B. Goodenough and Y. Kim, *Challenges for Rechargeable Li Batteries.* Chemistry of materials, 2009. **22**(3): p. 587-603.
15. S. Zhang, *A review on electrolyte additives for lithium-ion batteries.* Journal of power sources, 2006. **162**(2): p. 1379-1394.
16. K. Tasaki, *Solvent decompositions and physical properties of decomposition compounds in Li-ion battery electrolytes studied by DFT calculations and molecular dynamics simulations.* Journal of Physical Chemistry B, 2005. **109**(7): p. 2920-2933.
17. M.D. Halls and K. Tasaki, *High-throughput quantum chemistry and virtual screening for lithium ion battery electrolyte additives.* Journal of power sources. **195**(5): p. 1472-1478.

18. S.-T. Myung, et al., *Electrochemical behavior of current collectors for lithium batteries in non-aqueous alkyl carbonate solution and surface analysis by ToF-SIMS.* Electrochimica Acta, 2009. **55**(1): p. 288-297.
19. S.-T. Myung, Y. Hitoshi, and Y.-K. Sun, *Electrochemical behavior and passivation of current collectors in lithium-ion batteries.* Journal of materials chemistry, 2011. **21**(27): p. 9891-9911.
20. B.J. Landi, et al., *Carbon nanotubes for lithium ion batteries.* Energy & Environmental Science, 2009. **2**(6): p. 638-654.
21. R.L. McCreery, *Advanced carbon electrode materials for molecular electrochemistry.* Chemical reviews, 2008. **108**(7): p. 2646-2687.
22. D. Chung, *Review graphite.* Journal of materials science, 2002. **37**(8): p. 1475-1489.
23. M. Inaba, *Secondary batteries-Lithium rechargeable systems - Lithium-ion | Negative Electrodes: Graphite*, in *Encyclopedia of Electrochemical Power Sources*. 2009, Elsevier: Amsterdam. p. 198-208.
24. M. Winter, et al., *Insertion Electrode Materials for Rechargeable Lithium Batteries.* Advanced materials, 1998. **10**(10): p. 725-763.
25. J.O. Besenhard and M. Winter, *Handbook of Battery Materials*, ed. J.O. Besenhard. 1999: Wiley-VCH.
26. S. Doyenlang, et al., *Theoretical-study of charge-transfer in graphite-intercalation compounds.* Synthetic Metals, 1993. **58**(1): p. 95-107.
27. R.C. Boehm and A. Banerjee, *Theoretical study of lithium intercalated graphite.* The Journal of Chemical Physics, 1992. **96**(2): p. 1150-1157.
28. T. Tran and K. Kinoshita, *Lithium intercalation deintercalatation behaviour of basal and edge planes of highly oriented pyrolytic-graphite and graphite powder.* Journal of Electroanalytical Chemistry, 1995. **386**(1-2): p. 221-224.
29. Y. NuLi, J. Yang, and Z. Jiang, *Intercalation of lithium ions into bulk and powder highly oriented pyrolytic graphite.* Journal of Physics and Chemistry of Solids, 2006. **67**(4): p. 882-886.
30. A. Funabiki, M. Inaba, and Z. Ogumi, *A.c. impedance analysis of electrochemical lithium intercalation into highly oriented pyrolytic graphite.* Journal of power sources, 1997. **68**(2): p. 227-231.
31. A.N. Dey and B.P. Sullivan, *Electrochemical decomposition of propylene carbonate on graphite.* Journal of the Electrochemical Society, 1970. **117**(2): p. 222-&.
32. M. Arakawa and J. Yamaki, *The cathodic decomposition of propylene carbonate in lithium batteries.* Journal of electroanalytical chemistry and interfacial electrochemistry, 1987. **219**(1-2): p. 273-280.
33. J. Besenhard, *Electrochemical preparation and properties of ionic alkali metal- and NR4-graphite intercalation compounds in organice electrolytes.* Carbon, 1976. **14**(2): p. 111-115.
34. J. Besenhard and H. Fritz, *The electrochemistry of black carbons.* Angewandte Chemie. International edition in English, 1983. **22**(12): p. 950-975.
35. J.O. Besenhard, H. Mohwald, and J.J. Nickl, *Electronic conductivity and structure of DMSO-solvated A-+-graphite and NR-4(+)-graphite intercalation compounds.* Carbon, 1980. **18**(6): p. 399-405.

36. G. Eichinger, *Cathodic decomposition reactions of propylene carbonate.* Journal of Electroanalytical Chemistry, 1976. **74**(2): p. 183-193.
37. J.O. Besenhard and H.P. Fritz, *Cathodic reduction of graphite in organic solutions of alkali and NR4+ salts.* Journal of Electroanalytical Chemistry, 1974. **53**(2): p. 329-333.
38. D. Aurbach, et al., *The Correlation Between the Surface Chemistry and the Performance of Li-Carbon Intercalation Anodes for Rechargeable `Rocking-Chair' Type Batteries.* Journal of the Electrochemical Society, 1994. **141**(3): p. 603-611.
39. R. Fong, U. Vonsacken, and J. Dahn, *Studies of lithium intercalation into carbons using nonaqueous electrochemical-cells.* Journal of the Electrochemical Society, 1990. **137**(7): p. 2009-2013.
40. E. Peled, *The Electrochemical-Behaviour of Alkali and Alkaline-Earth Metals in Non-Aqueous Battery Systems - The Solid Electrolyte Interphase Model.* Journal of the Electrochemical Society, 1979. **126**(12): p. 2047-2051.
41. K. Xu, *Whether EC and PC Differ in Interphasial Chemistry on Graphitic Anode and How.* Journal of the Electrochemical Society, 2009. **156**(9): p. A751-A755.
42. J.O. Besenhard, et al., *Filming mechanism of lithium-carbon anodes in organic and inorganic electrolytes.* Journal of power sources, 1995. **54**(2): p. 228-231.
43. D. Aurbach, et al., *On the correlation between surface chemistry and performance of graphite negative electrodes for Li ion batteries.* Electrochimica Acta, 1999. **45**(1): p. 67-86.
44. D. Aurbach, *Electrode-solution interactions in Li-ion batteries: a short summary and new insights.* Journal of power sources, 2003. **119-121**: p. 497-503.
45. J.R. Dahn, *Phase-diagram of LixC6.* Physical Review B, 1991. **44**(17): p. 9170-9177.
46. K. Tasaki, A. Goldberg, and M. Winter, *On the difference in cycling behaviors of lithium-ion battery cell between the ethylene carbonate- and propylene carbonate-based electrolytes.* Electrochimica Acta, 2011. **56**(28): p. 10424-10435.
47. K. Xu, et al., *Solvation Sheath of Li+ in Nonaqueous Electrolytes and Its Implication of Graphite/Electrolyte Interface Chemistry.* The Journal of Physical Chemistry C, 2007. **111**(20): p. 7411-7421.
48. K. Xu, *"Charge-Transfer" Process at Graphite/Electrolyte Interface and the Solvation Sheath Structure of Li+ in Nonaqueous Electrolytes.* Journal of the Electrochemical Society, 2007. **154**(3): p. A162-A167.
49. T. Abe, et al., *Lithium Ion Transfer at the Interface between Lithium-Ion-Conductive Solid Crystalline Electrolyte and Polymer Electrolyte.* Journal of the Electrochemical Society, 2004. **151**(11): p. A1950-A1953.
50. T. Abe, et al., *Solvated Li-Ion Transfer at Interface Between Graphite and Electrolyte.* Journal of the Electrochemical Society, 2004. **151**(8): p. A1120-A1123.
51. K. Xu, A. von Cresce, and U. Lee, *Differentiating Contributions to Ion Transfer Barrier from Interphasial Resistance and Li+ Desolvation at Electrolyte/Graphite Interface.* Langmuir, 2010. **26**(13): p. 11538-11543.

52. X.Y. Song, K. Kinoshita, and T.D. Tran, *Microstructural characterization of lithiated graphite.* Journal of the Electrochemical Society, 1996. **143**(6): p. L120-L123.
53. R. Schlögl, *Graphite - A Unique Host Lattice*, in *Progress in Intercalation Research*, W. Müller-Warmuth and R. Schöllhorn, Editors. 1994, Springer Netherlands. p. 83-176.
54. J.R. Dahn, et al., *Dependence of the electrochemical intercalation of lithium in carbons on the crystal structure of the carbon.* Electrochimica Acta, 1993. **38**(9): p. 1179-1191.
55. T. Zheng, et al., *Lithium Insertion in High Capacity Carbonaceous Materials.* Journal of the Electrochemical Society, 1995. **142**(8): p. 2581-2590.
56. K. Sato, et al., *A Mechanism of Lithium Storage in Disordered Carbons.* Science, 1994. **264**(5158): p. 556-558.
57. S. Yata, et al., *Structure and properties of deeply Li-doped polyacenic semiconductor materials beyond C6Li stage.* Synthetic Metals, 1994. **62**(2): p. 153-158.
58. J.R. Dahn, et al., *Mechanisms for lithium insertion in carbonaceous materials.* Science, 1995. **270**(5236): p. 590-593.
59. T. Zheng and J.R. Dahn, *Hysteresis observed in quasi open-circuit voltage measurements of lithium insertion in hydrogen-containing carbons.* Journal of power sources, 1997. **68**(2): p. 201-203.
60. T. Zheng, W.R. McKinnon, and J.R. Dahn, *Hysteresis during Lithium Insertion in Hydrogen-Containing Carbons.* Journal of the Electrochemical Society, 1996. **143**(7): p. 2137-2145.
61. T. Zheng, J.S. Xue, and J.R. Dahn, *Lithium Insertion in Hydrogen-Containing Carbonaceous Materials.* Chemistry of materials, 1996. **8**(2): p. 389-393.
62. J.S. Xue and J.R. Dahn, *Dramatic Effect of Oxidation on Lithium Insertion in Carbons Made from Epoxy Resins.* Journal of the Electrochemical Society, 1995. **142**(11): p. 3668-3677.
63. C. Menachem, et al., *Characterization of modified NG7 graphite as an improved anode for lithium-ion batteries.* Journal of power sources, 1997. **68**(2): p. 277-282.
64. E. Peled, et al., *Improved Graphite Anode for Lithium-Ion Batteries Chemically: Bonded Solid Electrolyte Interface and Nanochannel Formation.* Journal of the Electrochemical Society, 1996. **143**(1): p. L4-L7.
65. S. Wang, Y. Matsumura, and T. Maeda, *A model of the interactions between disordered carbon and lithium.* Synthetic Metals, 1995. **71**(1â€“3): p. 1759-1760.
66. D. Aurbach, et al., *New insights into the interactions between electrode materials and electrolyte solutions for advanced nonaqueous batteries.* Journal of power sources, 1999. **81**: p. 95-111.
67. S.S. Zhang, K. Xu, and T.R. Jow, *EIS study on the formation of solid electrolyte interface in Li-ion battery.* Electrochimica Acta, 2006. **51**(8-9): p. 1636-1640.
68. E. Peled, et al., *Effect of carbon substrate on SEI composition and morphology.* Electrochimica Acta, 2004. **50**(2-3): p. 391-395.

69. D. Alliata, et al., *Electrochemical SPM investigation of the solid electrolyte interphase film formed on HOPG electrodes.* Electrochemistry Communications, 2000. **2**(6): p. 436-440.
70. K. Edstrom, M. Herstedt, and D.P. Abraham, *A new look at the solid electrolyte interphase on graphite anodes in Li-ion batteries.* Journal of power sources, 2006. **153**(2): p. 380-384.
71. H. Bryngelsson, et al., *How dynamic is the SEI?* Journal of power sources, 2007. **174**(2): p. 970-975.
72. P. Verma, P. Maire, and P. Novák, *A review of the features and analyses of the solid electrolyte interphase in Li-ion batteries.* Electrochimica Acta, 2010. **55**(22): p. 6332-6341.
73. A.J. Smith, et al., *A High Precision Coulometry Study of the SEI Growth in Li/Graphite Cells.* Journal of the Electrochemical Society, 2011. **158**(5): p. A447-A452.
74. F. Joho, et al., *Relation between surface properties, pore structure and first-cycle charge loss of graphite as negative electrode in lithium-ion batteries.* Journal of power sources, 2001. **97-98**: p. 78-82.
75. S. Brunauer, P.H. Emmett, and E. Teller, *Adsorption of Gases in Multimolecular Layers.* Journal of the American Chemical Society, 1938. **60**(2): p. 309-319.
76. T. Placke, et al., *Influence of graphite surface modifications on the ratio of basal plane to non-basal plane surface area and on the anode performance in lithium ion batteries.* Journal of power sources, 2011. **200**(0): p. 83-91.
77. K. Kanamura, et al., *X-ray photoelectron spectroscopic analysis and scanning electron-microscopic observation of the lithium surface immersed in nonaqueous solvents.* Journal of the Electrochemical Society, 1994. **141**(9): p. 2379-2385.
78. K. Kanamura, H. Tamura, and Z.-i. Takehara, *XPS analysis of a lithium surface immersed in propylene carbonate solution containing various salts.* Journal of Electroanalytical Chemistry, 1992. **333**(1-2): p. 127-142.
79. D. Aurbach, Y. Ein-Ely, and A. Zaban, *The Surface Chemistry of Lithium Electrodes in Alkyl Carbonate Solutions.* Journal of the Electrochemical Society, 1994. **141**(1): p. L1-L3.
80. D. Aurbach, et al., *Identification of surface-films formed on lithium in propylene carbonate solutions.* Journal of the Electrochemical Society, 1987. **134**(7): p. 1611-1620.
81. S. Zhang, et al., *Understanding solid electrolyte interface film formation on graphite electrodes.* Electrochemical and solid-state letters, 2001. **4**(12): p. A206-A208.
82. K. Kanamura, et al., *Morphology and chemical-compositions of surface-films of lithium deposited on a Ni substrate in nonaqueous electrolytes.* Journal of Electroanalytical Chemistry, 1995. **394**(1-2): p. 49-62.
83. A.M. Andersson and K. Edstrom, *Chemical Composition and Morphology of the Elevated Temperature SEI on Graphite.* Journal of the Electrochemical Society, 2001. **148**(10): p. A1100-A1109.
84. M.N. Richard and J.R. Dahn, *Accelerating rate calorimetry study on the thermal stability of lithium intercalated graphite in electrolyte I. Experimental.* Journal of the Electrochemical Society, 1999. **146**(6): p. 2068-2077.

85. S.S. Zhang, K. Xu, and T.R. Jow, *Optimization of the forming conditions of the solid-state interface in the Li-ion batteries.* Journal of power sources, 2004. **130**(1-2): p. 281-285.
86. M.H. Park, et al., *Low Li+ binding affinity: An important characteristic for additives to form solid electrolyte interphases in Li-ion batteries.* Journal of power sources. **196**(11): p. 5109-5114.
87. B. Simon, et al., *Hexagonal vs Rhombohedral Graphite: the Effect of Crystal Structure on Electrochemical Intercalation of Lithium Ions.* Molecular Crystals and Liquid Crystals Science and Technology. Section A. Molecular Crystals and Liquid Crystals, 1998. **310**(1): p. 333-340.
88. S. Flandrois and B. Simon, *Carbon materials for lithium-ion rechargeable batteries.* Carbon, 1999. **37**(2): p. 165-180.
89. M.E. Spahr, et al., *Purely Hexagonal Graphite and the Influence of Surface Modifications on Its Electrochemical Lithium Insertion Properties.* Journal of the Electrochemical Society, 2002. **149**(8): p. A960-A966.
90. M.E. Spahr, et al., *The role of graphite surface group chemistry on graphite exfoliation during electrochemical lithium insertion.* Journal of power sources, 2003. **119-121**(0): p. 543-549.
91. P. Novák, et al., *The importance of the active surface area of graphite materials in the first lithium intercalation.* Journal of power sources, 2007. **174**(2): p. 1082-1085.
92. M.E. Spahr, et al., *Surface reactivity of graphite materials and their surface passivation during the first electrochemical lithium insertion.* Journal of power sources, 2006. **153**(2): p. 300-311.
93. S.H. Ng, et al., *Correlations between surface properties of graphite and the first cycle specific charge loss in lithium-ion batteries.* Carbon, 2009. **47**(3): p. 705-712.
94. P. Bernardo, et al., *Influence of graphite surface properties on the first electrochemical lithium intercalation.* Carbon, 2011. **49**(14): p. 4867-4876.
95. J.P. Olivier and M. Winter, *Determination of the absolute and relative extents of basal plane surface area and "non-basal plane surface" area of graphites and their impact on anode performance in lithium ion batteries.* Journal of power sources, 2001. **97-98**: p. 151-155.
96. J.P. Olivier and S. Ross, *On Physical Adsorption. XVI. The Physical Interaction of H2, D2, CH4, and CD4 with Graphite.* Proceedings of the Royal Society of London. Series A. Mathematical and Physical Sciences, 1962. **265**(1323): p. 447-454.

3. Experimental techniques and graphite powder characteristics

There are numerous different methods used for the study of lithium ion batteries. In the following sections the main tools utilized to study the surface properties of graphite, thermal and electrochemical performance will be briefly presented. The specific experimental parameters will be described in more detail within the chapter where that specific method has been used.

3.1 Surface properties

The various graphites tested are commercial, like SLP30 (TIMCAL^{TM}) and G8, P5 (Cpreme), and as supplied from Elkem Carbon (A2/H2). The difference between A2 and H2 is the milling type. A2 used an Alpine mill (jet mill) while H2 used a Hicom mill (high intensity tumbling mill). Although the A2/H2 all were heat treated between 2300- 3000 ^{o}C in N_2 atmosphere to achieve a higher degree of graphitization, some of the A2/H2 samples experienced further heat treatment, where the minimum temperature was known to be 2650 ^{o}C (and up to 3000 ^{o}C) . These are denoted A2-2650 and H2-2650 in this work. The following sections will go through some of the most used methods in the study of the surface properties of these graphite materials.

3.1.1 BET Surface area

BET is a surface area technique that uses N_2 adsorption at varying pressures to determine the total surface area of a sample. BET can also be used to determine the pore size distribution. The method assumes that adsorption isotherm vs. pressure (relative to equilibrium pressure) is in the linear region. This assumption is usually correct if p/p_0 is between 0.05 and 0.35 [1]. It also assumes that the sample is energetically homogenous, meaning that Nitrogen is adsorbed with equal amount of energy on the entire surface of the sample.

3.1.2 Density functional theory

Density functional theory (DFT) can, by utilizing adsorption isotherms, provide an estimate for the amount of edge, basal or defect planes in graphite. This method was recently employed by Placke et.al [2]. The model was originally developed by Ross and Olivier [3] and deals with nitrogen adsorption data on heterogeneous surfaces of the same compound. The experimental adsorption isotherms, Q (p), are measured with standard nitrogen adsorption equipment. Then the value for q(p,e), which is the theoretical adsorption at a given adsorption potential and pressure, is evaluated/obtained

by non local DFT [4]. The value for amount adsorbed at the different surface energies, f(ε), is then de-convoluted according to the following equation:

$$Q(p) = \int q(p,\varepsilon) f(\varepsilon) d\varepsilon \tag{3.1}$$

The model assumes that the surface is inhomogenous with respect to nitrogen adsorption, which implies that edge planes in graphite will have different adsorption energies compared to basal planes or defects. Therefore, one can evaluate the contribution to the surface area at different adsorption energies, and to some extent obtain the relative ratio of edge/prismatic, defects and basal planes of the graphite sample. The main assumption with this method is that the surface behaves heterogeneously. Estimation of edge/basal/defect surface area has been shown to fit well with experimental data for synthetic graphite, natural graphite and carbon blacks [5].

For this work, a TriStar 3020 from Micromeritics was used for the nitrogen adsorption data and the following DFT evaluations (which are embedded in the software).

3.1.3 Pore size distribution

According to IUPAC [6] macropores are defined as pores with pore width exceeding 50 nm, micropores are pores with pore width below 2 nm, and mesopores have pore widths in intermediate sizes (less than 50 nm, but higher than 2 nm). Pore size is important in lithium ion batteries since micropores are too small to be active with regards to lithium intercalation. However, studies have shown that almost all of the graphite mesopores are wetted by the electrolyte and are a part of the electroactive surface area [7]. With this in mind it becomes very useful to investigate just how much mesopores and micropores a graphite sample contains, so that one can determine the actual surface area active in the electrochemical processes.

A semi-empirical method for determining micropores from Nitrogen gas adsorption isotherms was developed by HK (Horvath and Kawazoe) [8] in the early 80's. In this model it is assumed that the potential energy between the adsorbate and adsorbent, which can have some spatial distribution, are replaced by a *mean* potential energy. By using thermodynamics they are able to relate this average potential to the free energy of adsorption, creating a relation between filling pressure and pore width. They relate this mean energy with an equation describing how certain pore sizes/shapes have a characteristic pressure at which they are filled. However this method underestimates the pore size of micropores and mesopores (since it bases its calculation on macroscopic scale) and a two stage method was developed to improve upon this [9]. Due to the challenges with the HK method, estimation of micro/mesopores using DFT is generally considered a better approach, yielding more accurate values [10, 11].

3.1.4 Particle size distribution

Particle size distribution (PSD) was investigated with a CamsizerXT from Retsch Technology, and the values are given in Table 3.1. The particle size distribution was measured at the facilities of one of the industry partners, Elkem Carbon. For comparison, the d90 of the commercial graphites (TIMCAL™ for SLP30 and Cpreme for G8/P5) were added. The measurements of the d90 with the Camsizer are consistent with the supplied information from the manufacturer of the commercial graphites.

Table 3.1. Particle size distributions.

Carbon type	CamsizerXT PSD (From Retsch Technology)			From the manufacturer
	d10 (μm)	d50 (μm)	d90 (μm)	d90 (μm)
SLP30	8.9	16.2	28.7	32
G8	5.3	8.8	14.6	12-18
P5	4.2	6.7	9.9	9-13
A2	5.9	11.1	20.4	
H2	6.1	10.8	17.3	

3.1.5 Electrode density

Different types of carbon powders have been investigated in this study. Many of the characterization studies can only be applied to the actual carbon powders, but in reality (full sized battery) these are made into slurries and casted onto a Cu-foil. A property which would be useful for manufacturing is the electrode density, which is basically how much carbon powder you can fill into a certain volume. This is especially important for EV's, as you want to increase the volumetric energy density as much as possible. Depending on the powder properties the actual electrode density can vary between different carbon powders. The electrode densities with standard deviation for the cast used in this work are listed in Table 3.2. DFT/BET surface area measurements are also listed together with DFT estimated surface area of pores. Notably, DFT surface area estimates are slightly higher compared to BET. This difference arises mainly from the difference in their assumptions. Mainly BET assumes that N_2 adsorbs homogenously, while DFT assumes heterogeneous adsorption, as previously discussed.

Table 3.2. Electrode density and BET/DFT surface area measurements.

Carbon type	BET surface area (m^2/g)	Total DFT surface area (m^2/g)	Total DFT surface area of pores >14.83 Å (m^2/g)	Electrode density* (g/cm^3)
SLP30	6.16	6.47	2.41	0.775 ± 0.026
G8	1.79	1.88	0.61	1.068 ± 0.019
P5	3.48	3.69	1.23	1.072 ± 0.074
A2	22.52	25.42	8.95	0.757 ± 0.069
A2-2650	9.68	11.07	3.92	0.787 ± 0.034
H2	26.71	29.69	10.62	0.756 ± 0.027
H2-2650	12.17	12.86	4.71	0.794 ± 0.020

To increase electrode density it is common to perform calendaring on the electrode, which compresses the graphite electrode, consequently increasing the density. This has been showed to decrease the ICL and the reversible capacity of graphite, in addition to exhibiting a slight decrease in chemical diffusion with increased electrode density [12].

Table 3.3 shows the effect of calendaring on the electrode density of a cast made of an older batch of A2. The calendaring was performed on rubber rolls with a force of 60kN/m. The rolls were rotating at a speed of 10 m/s.

Table 3.3. Effect of calendaring on an older batch† of A2.

Carbon type	Electrode density (g/cm^3)	BET surface area (m^2/g)
A2	0.705 ± 0.031	19.60
A2 (after calendaring)	0.932 ± 0.001	19.60

* Bulk electrode density calculated by total weight, including PVDF and carbon black, divided by total volume

† Note the difference in BET surface area between this batch and the one in Table 3.2

Notably, the electrode density increased with calendaring. Another interesting result is that the standard deviation for the calendared samples was drastically reduced. This can be attributed to a more uniform thickness of the entire cast vs. the samples which were not calendared.

3.1.6 Oxygen content

Amount of oxygen on the surface of some of the different graphites was estimated using a TC-436 oxygen-nitrogen analyzer from LECO (Table 3.4). A recent study [13] investigated the effect of oxygen content with regards to the irreversible capacity loss, but found no clear correlation. The noticeable difference is the decrease in O_2 % with heat treatment, is related to a decreased amount of edge planes and defects at the expense of basal planes, as this is the main site where the oxygen groups are able to form.

Table 3.4. Oxygen content.

Carbon type	Oxygen content (%)
SLP30	0.183
A2	0.299
A2-2650	0.009
H2	0.395
H2-2650	0.007

3.1.7 X-ray diffraction

With respect to carbon, X-ray diffraction (XRD) is mostly used as a tool to investigate the degree of graphitization. The L_c value refers to the crystallite size perpendicular to the graphene layers, while the L_a value refers to crystallite size along the graphene layers. The d value refers to the distance between the graphene layers, also called the interlayer distance. Large values of L_a and L_c is correlated with a high degree of graphitization (long range order). If these values are low, we have no long range order and the material is considered amorphous. For natural graphite the L_c value is more than 1000 Å and the d value is 3.354 Å. For artificial graphite the L_c value is below 1000 Å and the d value is above 3.36 Å [14]. The interlayer distance, d, in amorphous carbon is twisted or rotated, and the number of hexagonal rings that consists of a crystallite is far less than in natural graphite. Therefore, the distance between the layers is far larger, and by examining this distance with XRD you get an indication of how well your sample is graphitized. The interlayer distance is calculated from Bragg's law and the L_c value is usually estimated from the full width at half maximum (FWHM) using the Scherrer equation. In general L_c values are usually taken from the 00*l* (*hkl*, where h and k = 0) diffraction line, while the L_a value is taken from the hk0 diffraction line [15]. Due to poor diffraction properties of carbon with respect to X-rays, the signal to noise ratio is very low. The measurements are also very sensitive to sample thickness as this can contribute to peak broadening. There is however a method developed to circumvent this

issue, published by Iwashita [16], which extracts information from carbon samples using a silicon standard as reference.

Since the L_a and L_c values can be different depending on which orientation that is chosen (002 will yield different results compared to 004 due to random stacking of crystallites), it is usually recommended to report values as L_c (002), so that the reader knows which orientation has been used for the calculations.

Fig. 3.1 shows a typical XRD pattern for graphite SLP30. By comparing the intensities of the (101) hexagonal and (101) rhomboehedral diffraction lines [17], the amount of rhombohedral phase can be estimated. In the figure, the L_c value is commonly estimated from the (002) peak.

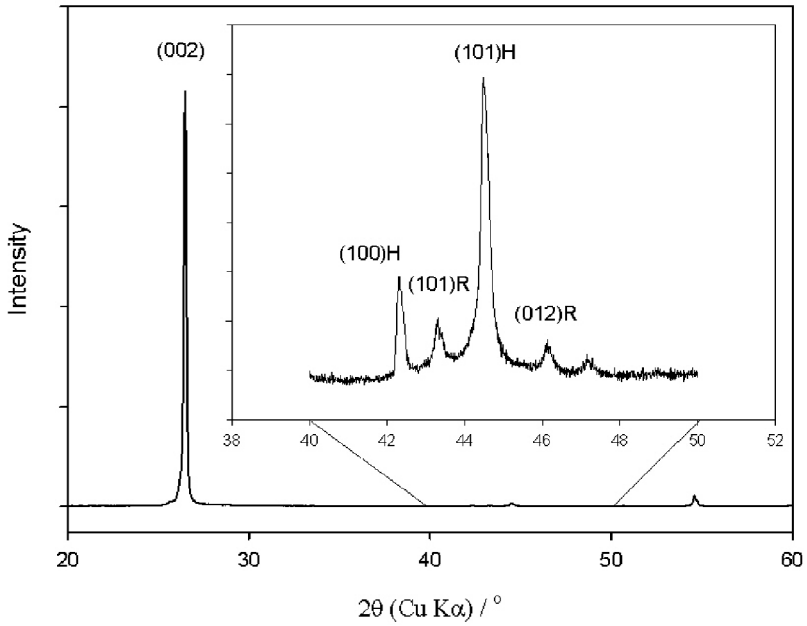

Figure 3.1. Typical X-ray diffraction pattern of graphite SLP30 with Cu-kα_1 radiation using a D8-focus from Bruker.

3.1.8 Scanning electron microscopy

Scanning electron microscopy (SEM) has also been utilized in this study to capture images of the surface morphology. In short, this method captures a magnified image of your sample by bombarding it with electrons from an electron beam, which are then reflected back to a detector, revealing information about the surface. Usually one has the option to use backscattered or secondary electrons, which provide different information. In this work, secondary electrons have been used. SEM can also be combined with energy-dispersive X-ray spectroscopy (EDS), which can give information about surface composition, and potentially give information about the inorganic components of the SEI. A typical SEM image of graphite SLP30 can be viewed in Fig. 3.2.

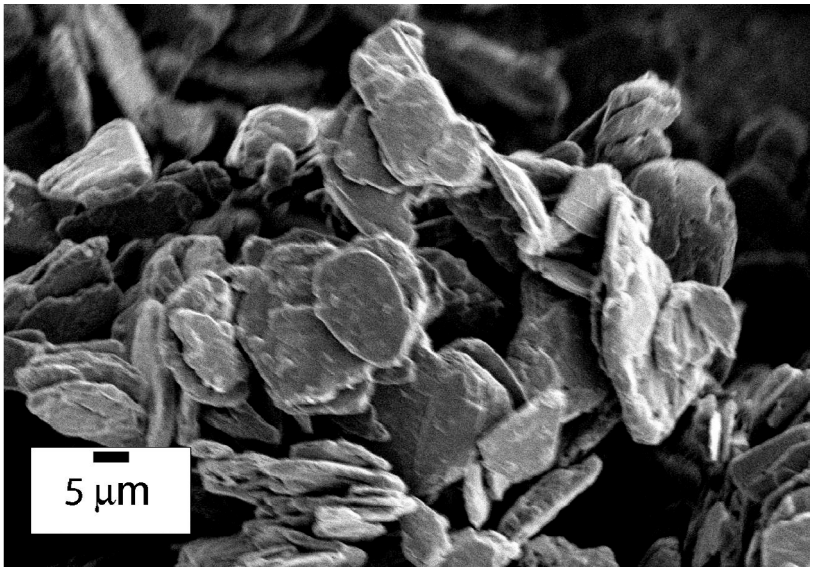

Figure 3.2. SEM image of SLP30 powder.

3.2 Electrochemical methods

Fig. 3.3 shows both two- and three- electrode setups commonly used in electrochemical testing. The two-electrode setup is used with galvanostatic cycling, but with impedance measurements, three-electrode setups are more convenient. This is due to the fact that one often wants to study only the changes occurring at one of the electrodes, the working electrode (WE). As soon as another electrode is added into the same system, such as a counter electrode (CE), a new interphase is instantly formed [18]. Impedance measurements with a two-electrode system would therefore record responses from both the WE and CE. A reference electrode (RE) therefore becomes necessary if it is desired to investigate only the response from one of the electrodes in an electrochemical cell.

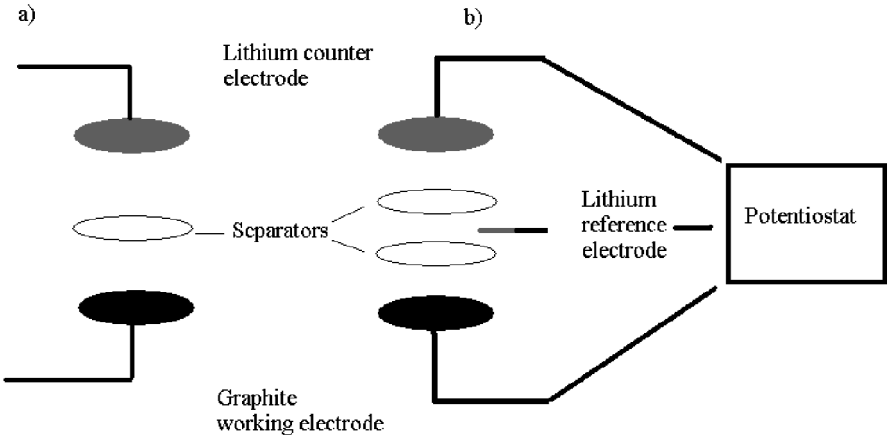

Figure 3.3. Typical electrochemical setups; a) Two-electrode cell b) Three-electrode cell.

Normally in lithium ion battery research, lithium metal is used as both reference and counter electrode. Using lithium metal as a CE is reasonable since we then have the same half-cell reaction (dissolution and deposition of lithium) occurring at each electrode, making the composition of the electrolyte more or less unaltered. The actual properties of a CE and reference electrode are well explained in a book by Southampton electrochemistry group [19], however a short summary will be presented. For a CE it is very important that the surface area is such that the half-cell reactions occurring here do not limit the half-cell reaction occurring at the WE, which in our case is the graphite. This is usually achieved by having a larger surface area of CE compared to the WE. For the reference electrode, it is important that it is located as close to the electrode of

interest as possible without disturbing the current path from the CE. The reference electrode should also be as non-polarizable as possible (meaning it doesn't store any charge in the double layer, but simply allow current to flow through), such that the change in chemical potential is minimal. This is achieved by using an electrode with high surface area and low resistance, providing fast kinetics (reversible reaction).

Even though Lithium metal is often used both as a reference electrode and counter electrode in lithium ion battery research, a recent study [20] showed the limitations of using lithium as a reference electrode (and counter electrode for two-electrode setups) due polarization occurring at high current densities (above 1 mA/cm^2). The effect of polarization of both CE and reference is important to keep in mind as a small change in the reference potential could have a large impact on the performance of the different graphite electrodes tested.

3.2.1 Galvanostatic cycling

Galvanostatic cycling uses a constant current to change the chemical potential of a system. A constant current is supplied until a limiting voltage (vs. a reference) is reached. For a graphite/lithium half-cell, a constant current would be supplied to intercalate lithium ions into the graphite structure, decreasing the potential of graphite vs. Li/Li^+. That current can then be reversed, applying the opposite constant current, until the graphite is completely empty of lithium ions (usually around 1-1.5 V vs. Li/Li^+). By measuring the current and time it can determine how much charge was used to fully intercalate (or de-intercalate) the graphite and one can charge/discharge graphite numerous times to investigate the cycling effect of the system in question. Important parameters include charge/discharge rates (also termed C-rate), and reversibility of the system (how much of the capacity is retained after each cycle). The C-rate is determined by how much current is supplied compared to the maximum (theoretical) charge available. For graphite a constant current of 10 mAh/g would have a C-rate of C/37.2, assuming it reaches the theoretical capacity of 372 mAh/g. This means it would take the system about 37.2 hours to completely charge (or discharge).

Typical initial galvanostatic curves for graphite SLP30 with 1:2:2 EC:DMC:EMC electrolyte, can be seen in Fig. 3.4. Notice the difference between the first and second cycle, around 0.8 V. This shoulder on the first cycle is attributed to electrolyte reduction and film formation and is not present during the second cycle, indicative of a complete film formation. Fig. 3.5 shows a similar curve, only here the electrolyte contains PC, a solvent known to cause some exfoliation before a protective film is formed. Signs of exfoliation are observable as a prolonged stay at higher potentials during the initial lithiation, as marked in the figure.

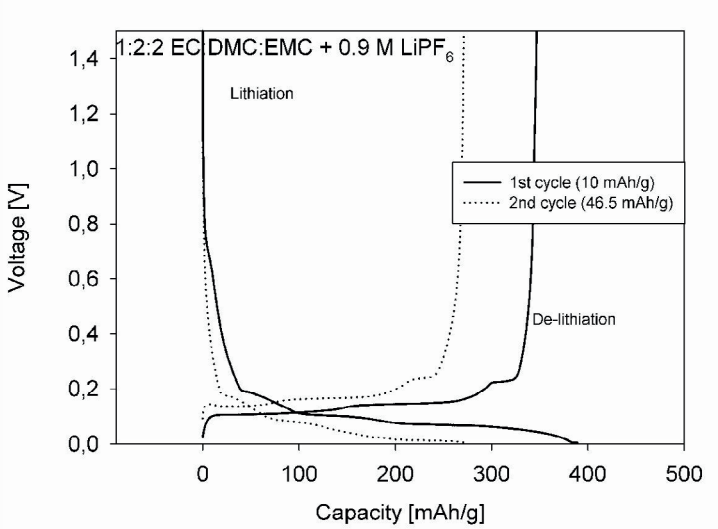

Figure 3.4. Initial galavanostatic curve for graphite SLP30/lithium half-cells in 1:2:2 EC:DMC:EMC electrolyte. 1st cycle at 10 mAh/g and 2nd cycle at 46.5 mAh/g.

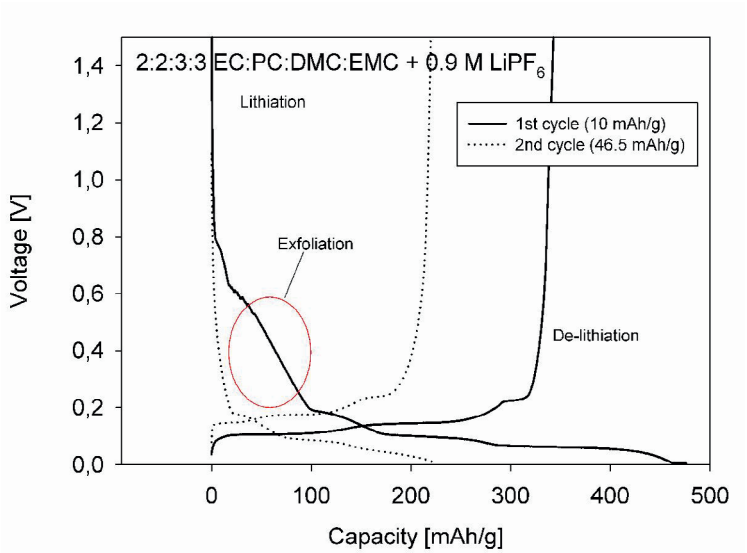

Figure 3.5. Initial galavanostatic curve for graphite SLP30/lithium half-cells in 2:2:3:3 EC:PC:DMC:EMC electrolyte. 1st cycle at 10 mAh/g and 2nd cycle at 46.5 mAh/g.

The potential plateaus during the initial intercalation, related to stage formation in graphite, are also seen in Fig. 3.4 and 3.5. However, the potentials where this occurs can be more clearly observed with differential capacity plots, as in Fig. 3.6 and 3.7.

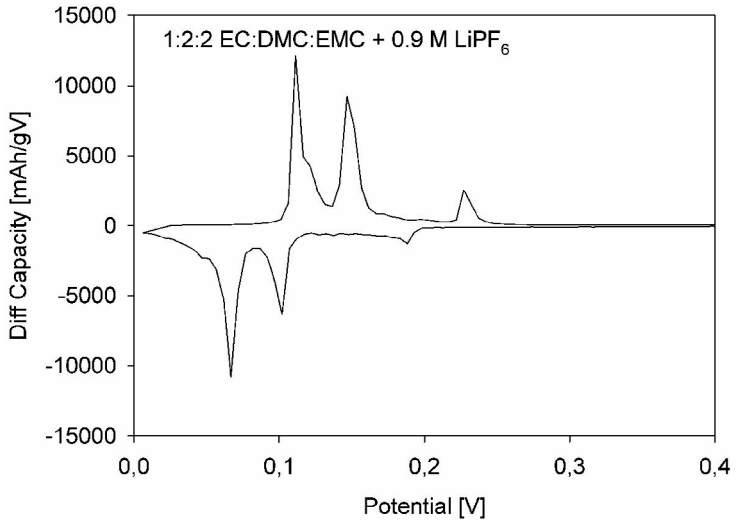

Figure 3.6. Differential capacity curve of the first cycle at 10 mAh/g for graphite SLP30/lithium half-cells in 1:2:2 EC:DMC:EMC electrolyte.

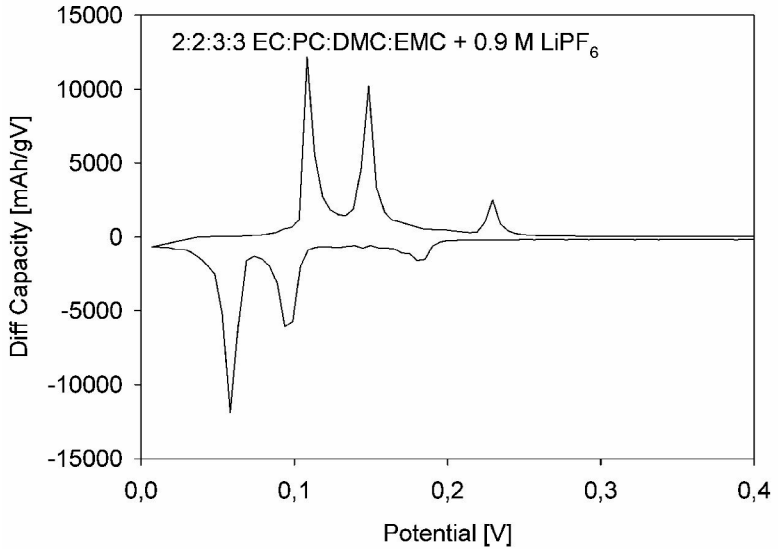

Figure 3.7. Differential capacity curve of the first cycle at 10 mAh/g for graphite SLP30/lithium half-cells in 2:2:3:3 EC:PC:DMC:EMC electrolyte.

3.2.2 Electrochemical Impedance Spectroscopy

Electrochemical Impedance Spectroscopy (EIS), or AC impedance as it is sometimes called, is an electrochemical characterisation tool which is mainly used to investigate the rate at which different reactions occur on an electrode surface. The interested reader can learn more about EIS in the book by Orazem and Tribollet [21].

The method, in short, supplies an AC current/voltage with different frequencies and measures the corresponding current/voltage response. To extract data, the measurements are usually fitted using a software, for example ZsimpWin (from Princeton Applied Research), with equivalent circuits (EQC) based on real physical values. Herein lays the greatest challenges with impedance as it may be difficult to find a system which provides a good fit and at the same time have physical meaning. The same system can in practice show good fits with many different models. Some of the more common EQC are listed in Table 3.5.

Perhaps the most discussed circuit element is the constant phase element (CPE). Often a CPE is used in the fitting of impedance data when a normal capacitance shows poor correlation. The challenges lie in the fact that it is difficult to explain the physical meaning of a CPE. Hirschorn [22, 23] explains how CPE can be fitted well with a model of a normal power-law distribution of local resistivity with a uniform dielectric constant. They stress the importance of using the correct formula for any given distribution [24] when estimating the capacitance from CPE. The model developed by Brug et al. [25] deals with surface distribution of time constants having uniform Ohmic and charge-transfer resistances, while the model developed by Hus and Mansfeld [26] deals with normal distribution. A surface distribution of time constants fits well with the porous graphite electrode with a surface film that can have different properties on edge, defect and basal sites. This could justify the use of a CPE to fit the data for graphite electrodes in lithium ion batteries.

Table 3.5. Common equivalent circuit elements [27].

	Symbol	Impedance
Resistance	R (Ohm)	R
Capacitance	C (F or Ohm^{-1} s)	$\frac{1}{j\omega C}$
Inductance	L (H or Ohm s)	$j\omega L$
Infinite Diffusion	Z_w(Ohm)	$\frac{R_w}{\sqrt{j\omega}}$
Finite Diffusion	Z_o (Ohm)	$R_D \tanh(\sqrt{(\frac{j\omega L_D^2}{D})} / \sqrt{(\frac{j\omega L_D^2}{D})}$
		$R_D \coth(\sqrt{(\frac{j\omega L_D^2}{D})} / \sqrt{(\frac{j\omega L_D^2}{D})}$
Constant phase element- CPE	Q ($Ohm^{-1}s^{\alpha}$)	$\frac{1}{Q(j\omega)^{\alpha}}$

The inhomogeneous surface film on graphite can also cause other effects, such as an inductive loop at low frequencies, which has been explained by different degrees of lithiation for various graphite particles due to different kinetics of intercalation, caused mainly by a difference in the surface film [28]. This effect could be more pronounced at lower temperature due to decreased kinetics. If the kinetics is fast, every particle should be able to intercalate more or less at the same time. However, if the kinetics are slow, some particles may be intercalated at a different rate than others, giving rise to lithium concentration gradients and thereby an inductive response (there may also be a difference occurring at fast kinetics due to differences in active sites, SEI formation etc, but this would not be as visible as the kinetics are so fast).

A recent review discussed the different time constants most common in EIS spectra of lithium ion battery systems [29]. In short, there are two main models describing the EIS system of lithium ion batteries; The *adsorption model* in Fig. 3.8 (originally developed by Bruce et. al [30, 31]), which states that the high frequency arc is due to solvated lithium partially de-solvating. The partially solvated lithium ion is then completely removed from its solvation sheath and enters the lattice (which would be a middle frequency arc), before we finally have some ion diffusion at low frequencies.

The adsorption model does not account for the well-known SEI film, and therefore a better model might be the *surface layer model* (by Aurbach's group) [33] shown in Fig. 3.9.

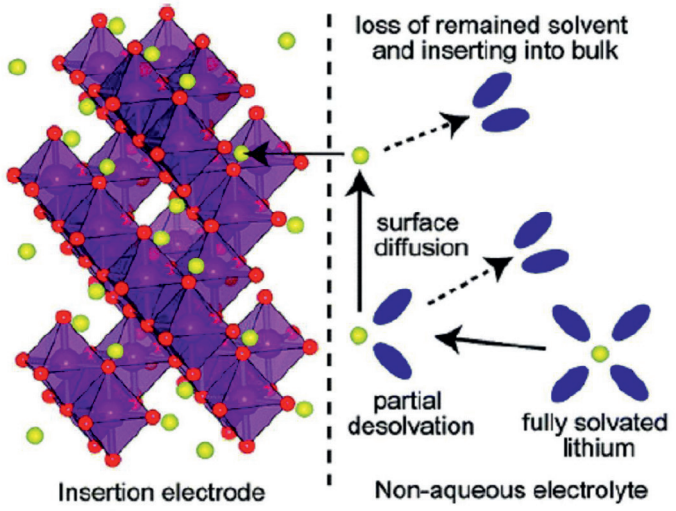

Figure 3.8. Adsorption model from [32].

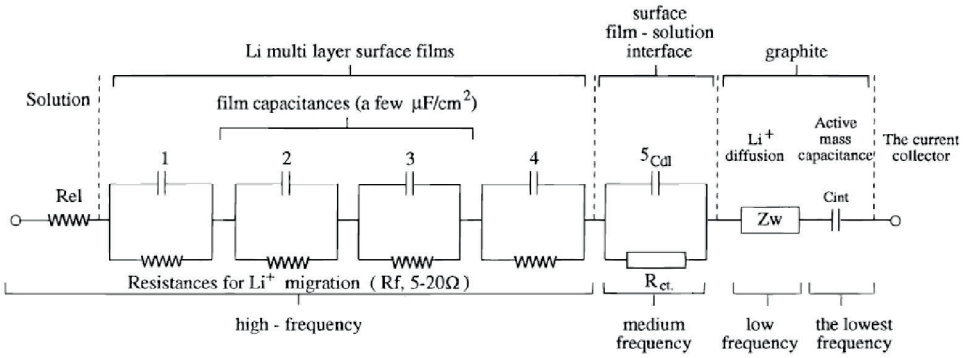

Figure 3.9. Surface layer model [33].

In the surface layer model the high frequency arc is attributed to the surface film, middle frequency is the charge transfer, and the low frequency is lithium ion diffusion in the graphite. While the adsorption model attributes the high frequency area to de-solvation processes, the surface layer model attributes this to Li^+ migration through the film.

Fig. 3.10 shows the model suggested by Xu [34, 35] based on studies by Abe and Ogami [36, 37] stating that it is in fact the de-solvation process being responsible for the largest contribution to the impedance, the so called "charge transfer". This was then investigated experimentally by comparing activation energies of a system with and

without interphase, thereby being able to conclude that the de-solvation energy indeed is the largest contributor to the overall activation energy [38]. They calculated the activation energy from impedance measurements at different temperatures by plotting log (Rct^{-1}) vs. the reciprocal of temperature 1/T, and the slope could be related to the activation energy according to Eq. 3.2 [36, 37].

$$Ea = -19.144 * slope \ \ (kJ\ mol^{-1}) \qquad (3.2)$$

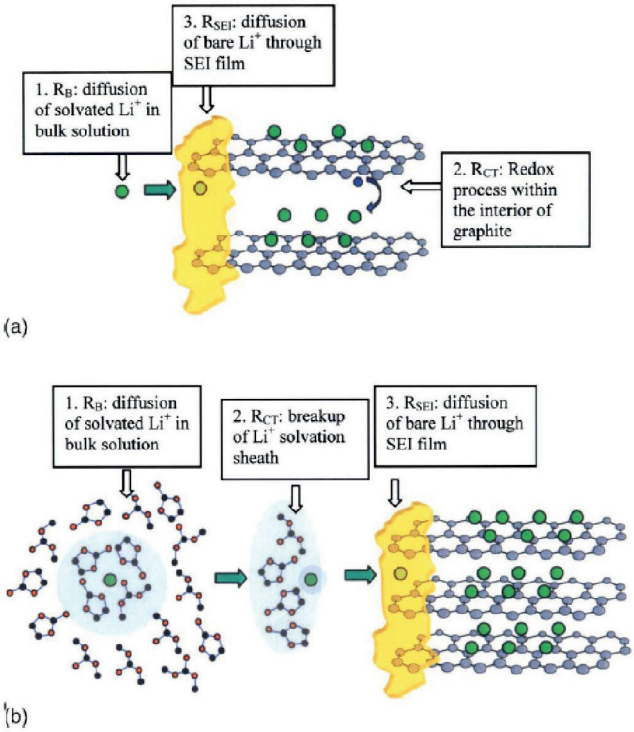

Figure 3.10. Model suggested by Xu et.al [35]. a) Normal convention with Li^+ diffusion across SEI at high frequency followed by a charge transfer at the interface at lower frequencies b) rationale based on Abe and Ogami [36, 37] suggesting that de-solvation energy is responsible for a large part of the charge transfer.

3.3 Differential scanning calorimetry

Differential scanning calorimetry (DSC) measures the difference in heat between your sample and a reference up to a certain temperature upon heating or cooling. If the sample demands less heat than the reference, we have an exothermic reaction. If the sample demands more heat than the reference, the reaction is endothermic.

For a full cell battery, both the positive electrode (PE) and the negative electrode (NE), exhibit thermal responses. The contribution in terms of thermal response from PE and NE showed that it is the decomposition of the PE and the consequent reaction with electrolyte that causes thermal runaway [39]. However, it is the heat from the breakdown of the SEI on the NE that showed the lowest onset temperature for exothermic reaction in a full cell. This is important to keep in mind as this could be an initiator for the exothermic reactions occurring on the PE, ultimately leading to thermal runaway. A fully lithiated NE is often used in DSC to investigate the "worst case scenario" as studies on the effect of state of charge (SOC) shows that the more lithium left in the graphite structure after the initial SEI breakdown, the more heat is evolved, and the earlier is the onset temperature for structural collapse [40]. This structural collapse then liberates the remaining lithium ions to further react with PVDF to produce even more heat. A more recent study [41] relates this structural collapse to intercalation of solvent molecules (now made possible by initial SEI breakdown occurring around 70-80 ^{o}C) and formation of gaseous products increasing the internal pressure upon further heating. The SEI breakdown, especially in $LiPF_6$ containing electrolytes, where $LiPF_6$ can decompose to LiF and PF_5 [42-45] (around 70 ^{o}C), can be facilitated by PF_5 being a strong Lewis acid and able to attack the functional groups (like the C-O group of $(CH_2OCO_2Li)_2$) and damage the SEI at 80 ^{o}C [46].

The main observation regarding DSC of intercalated graphite and its reactions can be summarized as follows [47] .

1) Meta-stable components of the SEI decompose to stable according to Eq. 3.3-3.4.

$$(CH_2OCO_2Li)_2 \rightarrow Li_2CO_3 + C_2H_4 + CO_2 + \frac{1}{2}O_2 \quad (3.3)$$

$$2Li + (CH_2OCO_2Li)_2 \rightarrow 2Li_2CO_3 + C_2H_4 \quad (3.4)$$

2) Intercalated lithium diffuse to the surface (or are exposed) and react with electrolyte to make stable products

This process continues until all the active edge sites are blocked by stable species, such as Li_2CO_3 and LiF [40]. The remaining lithium in the structure is very active and will with increasing temperature eventually cause exfoliation and be released into the electrolyte where it finally reacts with PVDF (to form LiF and hydrogen) at high temperature [40].

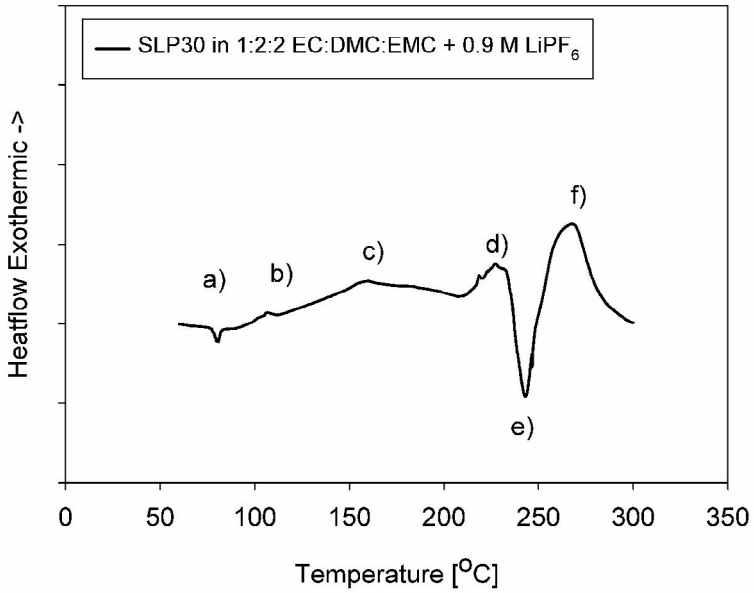

Figure 3.11. Differential scanning calorimetry; a) $LiPF_6$/EC melting [39] b-d) decomposition of SEI [47] e) exfoliation of graphite [41] followed by f) reaction of remaining lithium with PVDF to form LiF and hydrogen [40].

Fig. 3.11 summarizes the typical DSC response of fully lithiathed graphite in contact with electrolyte. The possible reactions in the temperature range 80-120 ^{o}C (Fig. 3.11 b-d), in addition to Eq. 3.3 and 3.4, are Eq. 3.5 through 3.9 [41]:

$$LiPF_6 \rightarrow LiF + PF_5 \tag{3.5}$$

$$Li_2CO_3 + PF_5 \rightarrow CO_2 + 2LiF + PF_3O \tag{3.6}$$

$$PF_5 + traceH_2O \rightarrow 2HF + PF_3O \tag{3.7}$$

$$Li_2CO_3 + 2HF \rightarrow 2LIF + H_2O + CO_2 \tag{3.8}$$

$$Li_2CO_3 \rightarrow Li_2O + CO_2 \tag{3.9}$$

Notably, the reaction mechanism in Eq. 3.4 can represent all reactions with intercalated lithium and various electrolyte related surface species [41]. Since the breakdown of the SEI is affected by the amount of meta-stable species in the SEI, it is natural to believe that a higher amount of SEI would cause a higher thermal response. This was indeed confirmed by a study comparing the thermal response of two similar graphites (with high and low surface area) [40], and by a study relating the amount of heat evolved to the ICL and BET surface areas [48].

3.4 Other methods

There are a few methods used in the study of lithium ion batteries which have not been utilized much in this work, but have been used a lot by others, and can provide important information about the system. These will be mentioned shortly.

Raman is a spectroscopic technique that irradiates a sample with a laser beam causing "inelastic scattering". A basic intro to Raman and carbon is found in [49]. The sample is exposed to monochromatic light, and due to inelastic scattering the energy of the photon is shifted either up or down compared to the original frequency. This shift provides information about vibration, rotational and other low frequency transitions in molecules. The shift is often characteristic of different samples, like a fingerprint. It can be used to identify unknown samples by comparing with known data, or in the case for graphite it can be used to study the shift due to graphite (G-band) structure at 1582 or disordering (D-band) at 1360. The D-band (disorder) appears around 1360 cm^{-1}, while the G-band (graphite) appears around 1582 cm^{-1}. The ratio of these is often taken as an indication of graphitization. With regards to ASA there is also a relationship between Raman L_a value and the ASA [50]. High active surface area means low L_a value.

X-ray photoelectron spectroscopy (XPS) and Fourier transform infrared spectroscopy (FTIR) has also been utilized a lot in the literature, mainly in the study of the surface film. Some notable studies with XPS are those by Kanamura [45, 51], and FTIR by Aurbach [52-54], who identified the main components of the SEI. Some of the main components identified in these studies are alkyl carbonates (RCO_3Li, R = alkyl), lithium ethyl carbonate and Li_2CO_3, to name a few.

References

1. S. Brunauer, P.H. Emmett, and E. Teller, *Adsorption of Gases in Multimolecular Layers.* Journal of the American Chemical Society, 1938. **60**(2): p. 309-319.
2. T. Placke, et al., *Influence of graphite surface modifications on the ratio of basal plane to non-basal plane surface area and on the anode performance in lithium ion batteries.* Journal of power sources, 2011. **200**(0): p. 83-91.
3. J.P. Olivier and S. Ross, *On Physical Adsorption. XVI. The Physical Interaction of H2, D2, CH4, and CD4 with Graphite.* Proceedings of the Royal Society of London. Series A. Mathematical and Physical Sciences, 1962. **265**(1323): p. 447-454.
4. P. Tarazona, *Free-energy density functional for hard spheres.* Physical Review A, 1985. **31**(4): p. 2672-2679.
5. J. Olivier, Adsorption of carbons, 2008: p. CH7.
6. A.D. McNaught and A. Wilkinson, eds. *IUPAC. Compendium of Chemical Terminology*. 2 ed. Blackwell Scientific Publications,. Oxford (1997).
7. F. Joho, et al., *Relation between surface properties, pore structure and first-cycle charge loss of graphite as negative electrode in lithium-ion batteries.* Journal of power sources, 2001. **97-98**: p. 78-82.
8. G. Horvath and K. Kawazoe, *Method for the calculation of effective pore-size distribution in molecular-sieve carbon.* Journal of Chemical Engineering of Japan, 1983. **16**(6): p. 470-475.
9. R.J. Dombrowski and C.M. Lastoskie, *A two-stage Horvath-Kawazoe adsorption model for pore size distribution analysis*, in *Studies in Surface Science and Catalysis*, B.M.J.R. F. Rodriguez-Reinoso and K. Unger, Editors. 2002, Elsevier. p. 99-106.
10. S. Lowell, et al., *Micropore Analysis*, in *Characterization of Porous Solids and Powders: Surface Area, Pore Size and Density*. 2004, Springer Netherlands. p. 129-156.
11. S. Lowell, et al., *Mesopore Analysis*, in *Characterization of Porous Solids and Powders: Surface Area, Pore Size and Density*. 2004, Springer Netherlands. p. 101-128.
12. J. Shim and K.A. Striebel, *The dependence of natural graphite anode performance on electrode density.* Journal of power sources, 2004. **130**(1-2): p. 247-253.
13. P. Bernardo, et al., *Influence of graphite surface properties on the first electrochemical lithium intercalation.* Carbon, 2011. **49**(14): p. 4867-4876.
14. *Handbook of Battery Materials*, ed. J.O. Besenhard. 1999: Wiley-VCH.
15. M. Inagaki, *New Carbons - Control of Structure and Functions*. Materials & Mechanical. 2000: Elsevier Science Ltd. 1-240.
16. N. Iwashita, et al., *Specification for a standard procedure of X-ray diffraction measurements on carbon materials.* Carbon, 2004. **42**(4): p. 701-714.
17. H. Huang, et al., *Effect of a rhombohedral phase on lithium intercalation capacity in graphite.* Solid State Ionics, 1998. **110**(3-4): p. 173-178.

18. J.O.M. Bockris, A.K.N. Reddy, and M.E. Gamboa-Aldeco, *Modern Electrochemistry 2A*. 2 ed. 2000.
19. D. Pletcher, et al., *Instrumental methods in electrochemistry*. Southampton Electrochemistry Group. 1985, England: Woodhead Publishing Limited.
20. F. La Mantia, et al., *Reliable reference electrodes for lithium-ion batteries.* Electrochemistry Communications, 2013. **31**: p. 141-144.
21. M.E. Orazem and B. Tribollet, in *Electrochemical Impedance Spectroscopy*. 2008, John Wiley & Sons, Inc.
22. B. Hirschorn, et al., *Constant-Phase-Element Behavior Caused by Resistivity Distributions in Films*, in *Corrosion*, D.C. Hansen, A. Alfantazi, and V.J. Gelling, Editors. p. 77-94.
23. B. Hirschorn, et al., *Constant-Phase-Element Behavior Caused by Resistivity Distributions in Films I. Theory.* Journal of the Electrochemical Society. **157**(12): p. C452-C457.
24. B. Hirschorn, et al., *Determination of effective capacitance and film thickness from constant-phase-element parameters.* Electrochimica Acta. **55**(21): p. 6218-6227.
25. G.J. Brug, et al., *The analysis of electrode impedances complicated by the presence of a constant phase element.* Journal of electroanalytical chemistry and interfacial electrochemistry, 1984. **176**(1-2): p. 275-295.
26. C.H. Hsu and F. Mansfeld, *Concernng the conversion of the constant phase element parameter Y 0 into a capacitance.* Corrosion, 2001. **57**(9): p. 747-748.
27. V.F. Lvovich, *Equivalent-Circuit Elements and Modeling of the Impedance Phenomenon*, in *Impedance Spectroscopy*, John Wiley & Sons, Inc. p. 37-47.
28. J.S. Gnanaraj, et al., *Formation and growth of surface films on graphitic anode materials for Li-ion batteries.* Electrochemical and Solid State Letters, 2005. **8**(2): p. A128-A132.
29. Q.C. Zhuang, et al., *Diagnosis of Electrochemical Impedance Spectroscopy in Lithium Ion Batteries.* Progress in Chemistry, 2010. **22**(6): p. 1044-1057.
30. P.G. Bruce and M.Y. Saidi, *A 2-step model of intercalation.* Solid State Ionics, 1992. **51**(3-4): p. 187-190.
31. P.G. Bruce and M.Y. Saidi, *The mechanism of electrointercalation.* Journal of Electroanalytical Chemistry, 1992. **322**(1-2): p. 93-105.
32. S. Kobayashi and Y. Uchimoto, *Lithium ion phase-transfer reaction at the interface between the lithium manganese oxide electrode and the nonaqueous electrolyte.* Journal of Physical Chemistry B, 2005. **109**(27): p. 13322-13326.
33. M.D. Levi and D. Aurbach, *Simultaneous measurements and modeling of the electrochemical impedance and the cyclic voltammetric characteristics of graphite electrodes doped with lithium.* Journal of Physical Chemistry B, 1997. **101**(23): p. 4630-4640.
34. K. Xu, et al., *Solvation Sheath of Li+ in Nonaqueous Electrolytes and Its Implication of Graphite/Electrolyte Interface Chemistry.* The Journal of Physical Chemistry C, 2007. **111**(20): p. 7411-7421.
35. K. Xu, *"Charge-Transfer" Process at Graphite/Electrolyte Interface and the Solvation Sheath Structure of Li+ in Nonaqueous Electrolytes.* Journal of the Electrochemical Society, 2007. **154**(3): p. A162-A167.

36. T. Abe, et al., *Lithium Ion Transfer at the Interface between Lithium-Ion-Conductive Solid Crystalline Electrolyte and Polymer Electrolyte.* Journal of the Electrochemical Society, 2004. **151**(11): p. A1950-A1953.
37. T. Abe, et al., *Solvated Li-Ion Transfer at Interface Between Graphite and Electrolyte.* Journal of the Electrochemical Society, 2004. **151**(8): p. A1120-A1123.
38. K. Xu, A. von Cresce, and U. Lee, *Differentiating Contributions to "Ion Transfer" Barrier from Interphasial Resistance and Li+ Desolvation at Electrolyte/Graphite Interface.* Langmuir. **26**(13): p. 11538-11543.
39. H. Maleki, et al., *Thermal stability studies of Li-ion cells and components.* Journal of the Electrochemical Society, 1999. **146**(9): p. 3224-3229.
40. H. Yang, et al., *Investigations of the exothermic reactions of natural graphite anode for Li-ion batteries during thermal runaway.* Journal of the Electrochemical Society, 2005. **152**(1): p. A73-A79.
41. O. Haik, et al., *On the Thermal Behavior of Lithium Intercalated Graphites.* Journal of the Electrochemical Society, 2011. **158**(8): p. A913-A923.
42. T. Kawamura, et al., *Thermal stability of alkyl carbonate mixed-solvent electrolytes for lithium ion cells.* Journal of power sources, 2002. **104**(2): p. 260-264.
43. X. Zhang, et al., *Diagnostic characterization of high power lithium-ion batteries for use in hybrid electric vehicles.* Journal of the Electrochemical Society, 2001. **148**(5): p. A463-A470.
44. S.E. Sloop, et al., *Chemical reactivity of PF5 and LiPF6 in ethylene carbonate/dimethyl carbonate solutions.* Electrochemical and Solid State Letters, 2001. **4**(4): p. A42-A44.
45. K. Kanamura, H. Tamura, and Z.-i. Takehara, *XPS analysis of a lithium surface immersed in propylene carbonate solution containing various salts.* Journal of Electroanalytical Chemistry, 1992. **333**(1-2): p. 127-142.
46. H.H. Lee, C.C. Wan, and Y.Y. Wang, *Thermal stability of the solid electrolyte interface on carbon electrodes of lithium batteries.* Journal of the Electrochemical Society, 2004. **151**(4): p. A542-A547.
47. M.N. Richard and J.R. Dahn, *Accelerating rate calorimetry study on the thermal stability of lithium intercalated graphite in electrolyte I. Experimental.* Journal of the Electrochemical Society, 1999. **146**(6): p. 2068-2077.
48. F. Joho, P. Novak, and M.E. Spahr, *Safety aspects of graphite negative electrode materials for lithium-ion batteries.* Journal of the Electrochemical Society, 2002. **149**(8): p. A1020-A1024.
49. R.L. McCreery, *Advanced carbon electrode materials for molecular electrochemistry.* Chemical reviews, 2008. **108**(7): p. 2646-2687.
50. C. Vix-Guterl, et al., *Surface Characterizations of Carbon Multiwall Nanotubes: Comparison between Surface Active Sites and Raman Spectroscopy.* The Journal of Physical Chemistry B, 2004. **108**(50): p. 19361-19367.
51. K. Kanamura, et al., *X-ray photoelectron spectroscopic analysis and scanning electron-microscopic observation of the lithium surface immersed in nonaqueous solvents.* Journal of the Electrochemical Society, 1994. **141**(9): p. 2379-2385.

52. D. Aurbach, et al., *Identification of surface-films formed on lithium in propylene carbonate solutions.* Journal of the Electrochemical Society, 1987. **134**(7): p. 1611-1620.
53. D. Aurbach, et al., *The study of electrolyte-solutions based on ethylene and diethyl carbonates for the rechargeable Li batteries.2. Graphtie-electrodes.* Journal of the Electrochemical Society, 1995. **142**(9): p. 2882-2890.
54. D. Aurbach, Y. Ein-Ely, and A. Zaban, *The Surface Chemistry of Lithium Electrodes in Alkyl Carbonate Solutions.* Journal of the Electrochemical Society, 1994. **141**(1): p. L1-L3.

4. DFT assisted assessment of edge/defect ratios in graphite and their influence on the thermal stability of lithium ion batteries

4.1 Summary

Raw graphite can be processed industrially in large quanta but for the graphite to be useful in lithium ion batteries (LIB's), certain parameters need to be optimized to reduce the first cycle irreversible capacity loss (ICL) and to increase cyclability. Some key parameters are graphite morphology, amount of active surface area, and particle size. Some of these parameters can to some extent be manipulated by surface coatings, milling processes or heat treatment in various atmospheres. In this study, several graphite materials (as received) from the industry have been investigated for use as anode material in LIB's and compared with commercial graphite. These materials have been exposed to two different milling processes, and some of the materials were heat treated in nitrogen atmosphere above 2650 ^{o}C. No significant difference in capacity was observed, but the heat treated materials obtained a lower BET surface area, which resulted in lower ICL. BET combined with density functional theory (DFT) has been employed to study the ratio of basal to non-basal plane and to determine the relative amount of defects. Thermal properties have been investigated with differential scanning calorimetry (DSC). High ethylene carbonate (EC) content improved the thermal stability for graphite with high amount of edge/defect surface area, but showed no improvement of graphite with lower amount of edge/defects. However, high ICL combined with low surface area seemed to improve the thermal properties in terms of total heat evolved. DFT measurement combined with ICL could therefore potentially be used as a tool to predict thermal stability.

Highlights

Graphite discharge capacity has been investigated for various graphite surfaces (amount edge/basal/defect) and related to the thermal behavior observed with DSC.

Keywords; lithium ion battery, graphite, thermal stability, DSC, DFT

4.2 Introduction

Lithium ion batteries (LIB) have been used commercially since the early 90's when Sony bought the Goodenough patent on $LiCoO_2$ [1] and used it to make $LiCoO_2$/coke batteries. The choice of using lithium ion batteries is mainly due to its high energy density (low weight and high energy). In our energy demanding society it would prove very useful to increase the size and change the operating conditions of the lithium ion battery, so that it may be used for large scale applications, such as electric vehicles (EV). This poses new challenges with regards to safety, cycle life and operating conditions.

Graphite has been the main choice of anode material in lithium ion batteries because of its availability and low cost. The electrolytes most commonly used have been the combination of cyclic carbonates, like ethylene carbonate (EC) and propylene carbonate (PC), together with linear carbonates, like diethylene carbonate (DEC), dimethyl carbonate (DMC), and ethyl methyl carbonate (EMC). However, due to the instability of graphite in these electrolytes, there is an irreversible capacity loss (ICL) during the first cycle of operation mainly due to the reduction of electrolyte species. After the reduction, a passive film is formed, preventing further reduction and increasing the stability of the graphite/electrolyte interface. This film is commonly termed the solid electrolyte interphase (SEI) [2]. Prior to this film formation, solvent species could co-intercalate into the graphite structure, causing exfoliation [3].

The reduction product of EC, $(CH_2OCO_2Li)_2$, and Li_2CO_3 are among the most passivating species due to their small size and polar nature, and are together with Li_xSO_y, Li_2O, and CH_3OLi regarded as good passivating agents [4]. EC is therefore known to be a vital electrolyte component when it comes to the formation of the SEI.

The surface properties of the graphite, both total surface area and amount of active surface area (ASA), have proven to be important parameters with regards to the first cycle irreversible capacity loss (ICL) [5, 6] and SEI formation and stability. However, a more recent study by Placke et.al [7] implemented the use of density functional theory (DFT) [8, 9] to determine the ratio of non-basal planes (edge/defects) vs. basal, to see how the amounts of defects varies with heat treatment of the graphite in oxygen atmosphere. They didn't see a linear increase in ICL with increasing BET as with previous authors [10], but they saw a strong correlation between non-basal planes and ICL. Another reason why the amount of non-basal plane might be useful is that intercalation of lithium in graphite mainly occurs through edge sites and only via defects on the basal planes [11-13]. A higher percentage of edge planes would therefore be advantageous for cycling at higher charge rates, and studies have shown that an increased amount of edge planes compared to basal planes reduces the charge transfer resistance [14]. Notably, a larger percentage of edge planes can also lead to a higher ICL [7]. Additionally, the surface properties can have a large effect on the thermal properties. Flaky morphology showed a much earlier onset temperature for exothermic reaction upon heating compared to round particle morphology [15]. This was attributed to an insufficient SEI formation, leaving many sites available for electrolyte reactions.

This conclusion was based on the fact that the first exothermic reaction in anode materials for lithium ion batteries is related to the conversion of meta-stable SEI species to more stable species [16], according to Eq. (4.1-4.2)

$$(CH_2OCO_2Li)_2 \rightarrow Li_2CO_3 + C_2H_4 + CO_2 + \frac{1}{2}O_2 \quad (4.1)$$

$$2Li + (CH_2OCO_2Li)_2 \rightarrow 2Li_2CO_3 + C_2H_4 \quad (4.2)$$

Some believe that the reaction in Eq. 4.2 is more likely, as no exothermic peak was observed for de-lithiated samples in the temperature range of 80-120 ^{o}C [17]. As it turns out, the state of charge (SOC) (or degree of lithiation) can have a large impact on the thermal response of the anode material, and studies have shown that there is generally a higher thermal response for samples with high state of charge (high concentration of lithium) [16, 18]. Conversion of meta-stable species by ageing at various temperatures also improved the thermal stability (increased the onset temperature for exothermic reactions) [15]. XPS studies of ageing at elevated temperatures has shown an increase in LiF species (in $LiPF_6$ containing electrolytes) with storage temperature [19]. In addition, Li_2CO_3 can also be formed according to Eq. (4.1-4.2) above [16].
It is clear that the properties of the SEI highly influence the thermal properties of the anode. The SEI is again highly influenced by surface area [5, 6] and formation conditions [20] in addition to the electrolyte solvent [21].

It is in the scope of this paper to investigate industrially supplied graphite, exposed to different milling processes and heat treatments, with regards to reversible capacity and irreversible capacity loss (ICL). The goal is to determine the non-basal to basal plane ratio using DFT studies and correlate this with the varying ICL and changes in thermal stability. It is expected that both milling type and varying heat treatment (in N_2 atmosphere) will have an effect on the cell performance. The effect of non-basal plane vs. basal plane on thermal stability has been less studied and would yield important knowledge regarding the safety of the battery, should it have an impact.

4.3 Experimental

Graphite SLP30 was used as received from TIMCAL^{TM}. Graphite Cpreme G8 and P5 were used as received from CPREME. Graphite A2/H2 and A2-2650/H2-2650, supplied by Elkem Carbon, have undergone varying degree of heat treatments (HT). Both A2/H2 and A2-2650/H2-2650 have undergone a graphitization process by heat treatment in N_2 atmosphere between 2300-3000 ^{o}C. However, for the A2-2650/H2-2650 the minimum temperature has been set at 2650 ^{o}C. The difference between A2 and H2 is mainly the milling method. The A-samples utilized an Alpine mill (jet milling) while H samples utilized a Hicom mill (high –intensity tumbling mill).

The graphite electrodes were prepared by tape casting slurries consisting of 37 g active graphite material (SLP30/G8/P5/A2/H2), 2 g PVDF (Kynar, reagent grade), 1 g Super P (TIMCAL^{TM}), and 60 g 1-methyl-2-Pyrrolidinone (Sigma-Aldrich > 99.5%) onto a 10 μm thick Cu-foil current collector from Circuit foil Luxembourg. The tape caster was a "K Control Coater" from Printcoat instruments. The casts were dried in a vacuum oven at 120 ^{o}C overnight.

The electrolytes were made using 4:3:3 or 1:2:2 weight ratio of ethylene carbonate (Sigma-Aldrich > 99 %), ethyl methyl carbonate (Merck, > 99 %), and dimethyl carbonate (Sigma-Aldrich, > 99 %) with 0.9 M $LiPF_6$ (Aldrich, >99.99 %).

The electrochemical measurements were performed on coin cells from Hohsen Corp which were assembled and sealed inside an argon-filled glove box (O_2 and H_2O < 0.1 ppm). The cells consisted of a graphite working electrode (2.01 cm^2) with a loading of about 3 mg/cm^2, separator (Celgard® 2320), and 0.75 mm thick lithium foil (1.54 cm^2) as counter electrode. All potentials are reported vs. Li/Li^+ unless otherwise specified. The cells were charged with a model 4200 potentiostat from Maccor at constant current of 10 mA/g until 5 mV vs. Li/Li^+, followed by a constant current of 5 mA/g until the current dropped to 5 mA/g to ensure the graphite was fully lithiated. The cells were then discharged with constant current of 10 mA/g until 1.5 V. The cells were then cycled between 0.005 and 1.5 V. All experiments were performed at room temperature (18-24 ^{o}C) unless otherwise specified.

Nitrogen adsorption data was recorded with Tristar 3020 from Micromeritics to obtain the BET and DFT values. The evaluation of the DFT values is embedded in the software from Micromeritics, and follow the theory by Ross and Olivier [8, 9].

Scanning electron microscopy (SEM) was performed with a Hitachi S-3400N in secondary electron mode.

Differential scanning calorimetri (DSC) measurements were performed using a DSC PerkinElmer DSC 7. The temperature range for the high temperature measurements was from 30 to 300 ^{o}C with 2.5 ^{o}C /min heating rate. 3 samples of 5 mm diameter were cut out from fully lithiated graphite electrodes (after 60 cycles of operation) and placed in gold plated stainless steel high pressure capsules (from PerkinElmer), together with 3 μl

of the same electrolyte used in that specific battery system, and completely sealed inside an argon-filled glove box (O_2 and H_2O < 0.1 ppm).

XRD measurements were performed with a D8- focus from Bruker, which uses Cu Kα radiation (λ = 1.54 Å) and a Lynxeye detector. Samples were measured relative to a Silgrain SI- standard to account for instrumental broadening [22].

4.4 Results

Fig. 4.1 through 4.7 show DFT analysis of graphite SLP30, H2, A2 (with and without HT), P5, and G8. These figures show how Nitrogen is adsorbed at different energies depending on the surface of the graphite. The adsorption energies centered around 50-60 K are generally attributed to the basal planes [8, 23] . Adsorption energies below 50 K are related to the edge/prismatic planes, while those above 60 K are related to defects. Notably, the heat treatments cause a decrease in the amount of edge planes and an increase in the amount of basal planes. There is also a peak emerging at very low adsorption potentials for the heat treated samples, while the relative amount of defects is more or less unchanged. Adsorption potentials are generally determined by the difference in the density of adsorbent constituent atoms at the interface [8]. Extended heat treatment therefore seems to decrease the density of carbons at certain sites, which would explain the peak emerging at lower adsorptive potentials (Fig. 4.3 and 4.5).

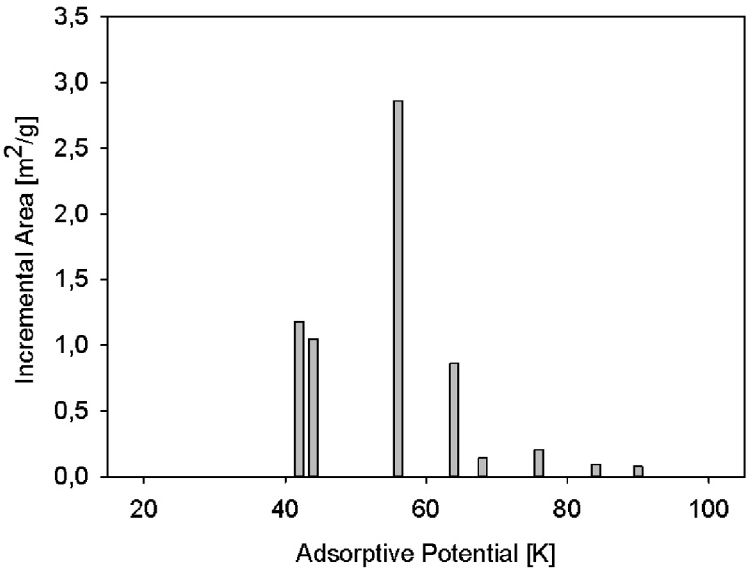

Figure 4.1. Incremental surface area as evaluated by a DFT analysis of nitrogen adsorption data for graphite SLP30.

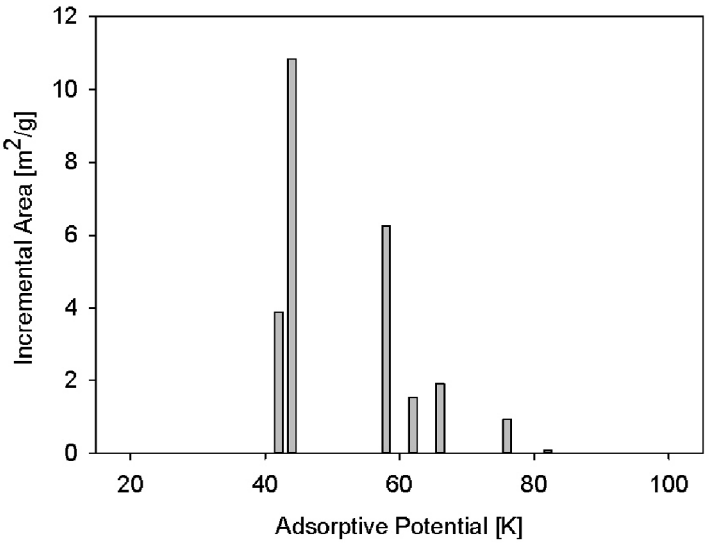

Figure 4.2. Incremental surface area as evaluated by a DFT analysis of nitrogen adsorption data for graphite A2.

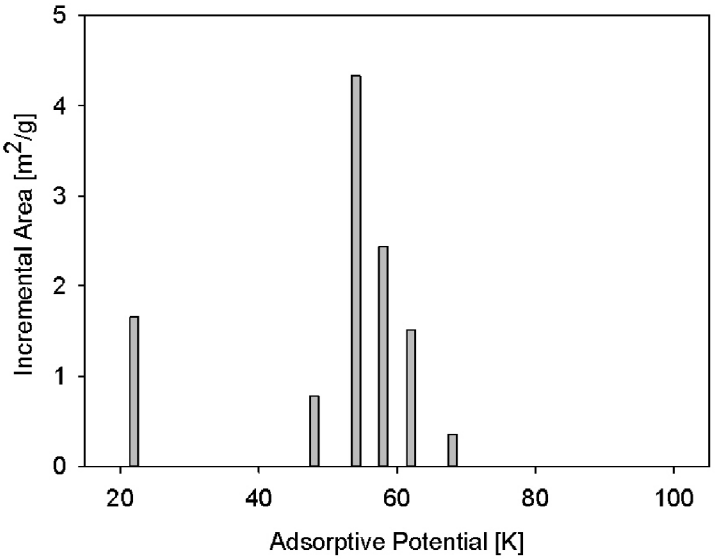

Figure 4.3. Incremental surface area as evaluated by a DFT analysis of nitrogen adsorption data for graphite A2-2650.

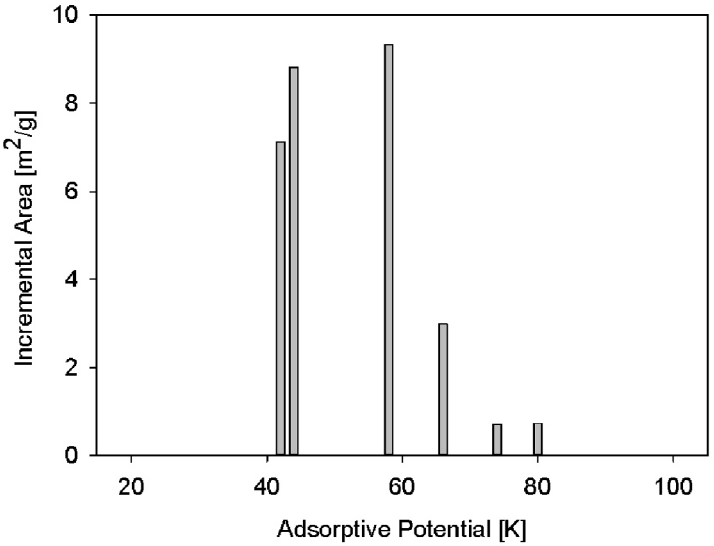

Figure 4.4. Incremental surface area as evaluated by a DFT analysis of nitrogen adsorption data for graphite H2.

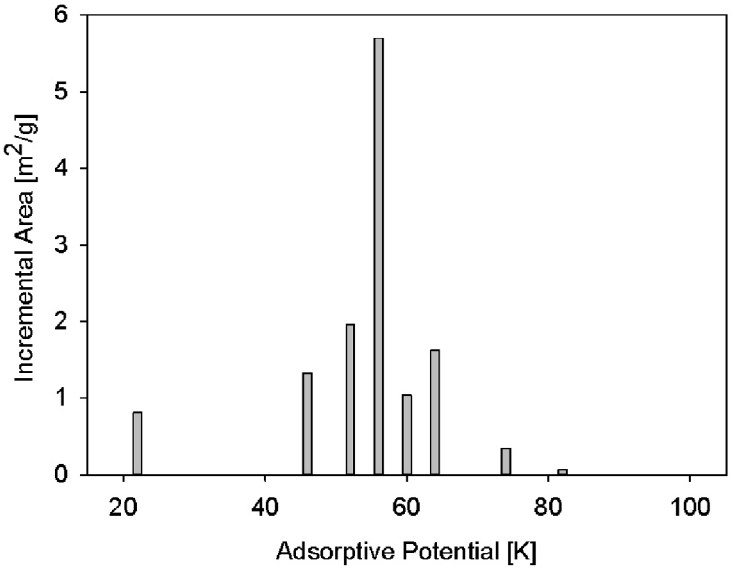

Figure 4.5. Incremental surface area as evaluated by a DFT analysis of nitrogen adsorption data for graphite H2-2650.

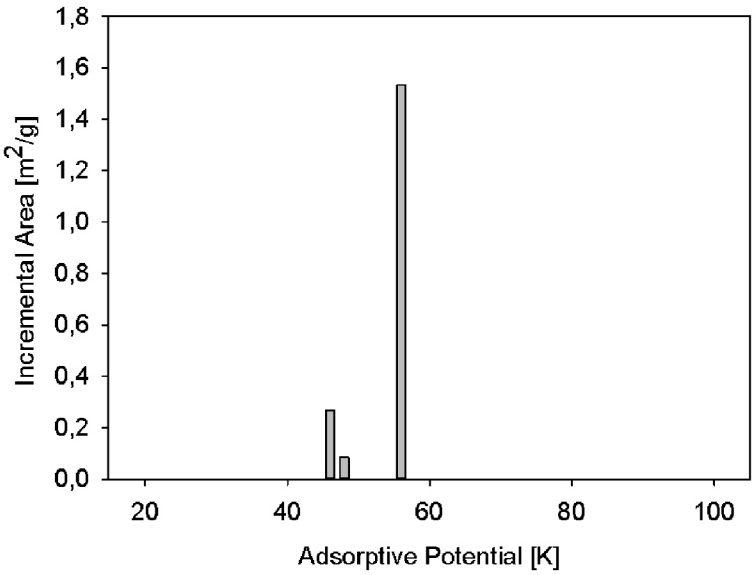

Figure 4.6. Incremental surface area as evaluated by a DFT analysis of nitrogen adsorption data for graphite G8.

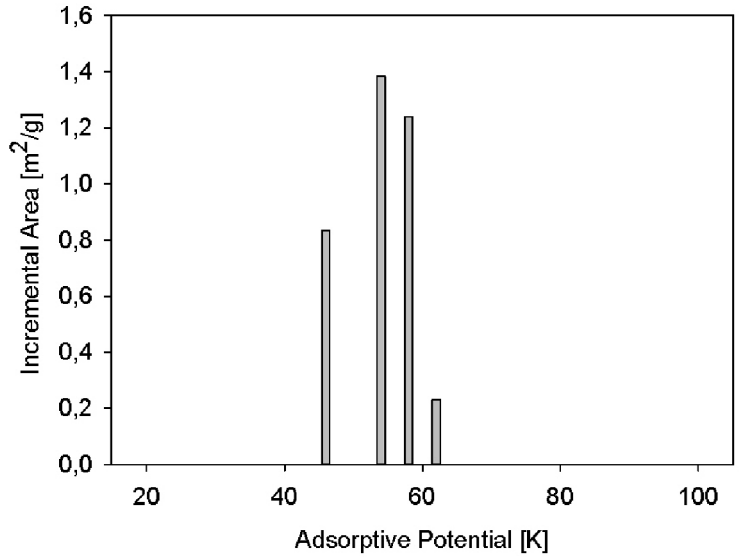

Figure 4.7. Incremental surface area as evaluated by a DFT analysis of nitrogen adsorption data for graphite P5.

Table. 4.1. Surface area, XRD and ICL data* for graphite samples in 1:2:2 EC:DMC:EMC + 0.9M $LiPF_6$ electrolyte

Graphite	ICL (mAh/g) (%)	BET surface area (m^2/g)	DFT surface area (m^2/g)	Ratio of prismatic(edge): basal plane (between 50-60 K): defect surface area (%)	d (002) (nm)	L_a (002) (nm)
SLP30	11.39±0.62	6.16	6.47	34.5:44.3:21.2	3.355	557
G8	9.77±0.068	1.79	1.88	18.6:81.4:0	-	-
P5	8.59±0.42	3.48	3.69	22.6:71.2:6.2	-	-
A2	26.62±0.70	22.52	25.42	57.9:24.6:17.5	3.363	76
A2-2650	16.48±0.18	9.68	11.07	22:61.1:16.9	3.363	102
H2	30.53±0.54	26.71	29.69	53.7:31.4:14.9	3.364	70
H2-2650	19.0±0.19	12.17	12.86	16.6:67.8:15.7	3.363	82

* Capacity data are based on the average of several samples and with a charge/discharge current of 10 mA/g (C/37.2)

BET surface area measurements, ICL, DFT and XRD values for the graphites used in this study are summarized in Table 4.1. The BET and the DFT surface areas are quite similar, although DFT surface areas give slightly higher values for all the materials. This difference in BET and DFT is consistent with similar studies, and is related to the different assumptions made in their theories [7]. These are mainly that the BET method assumes a homogeneous surface, while the DFT method assumes a hetrogeneous surface [24].

One of the main observations from the data in Table 4.1 is that the ICL seems to increase with both increasing total surface area (Fig. 4.8) and fraction of “non-basal” (edge/defect) planes (Fig. 4.9). There is in fact a linear response (except for G8 which shows some deviation from linearity) showing a correlation between a larger surface area and an increase in the ICL.

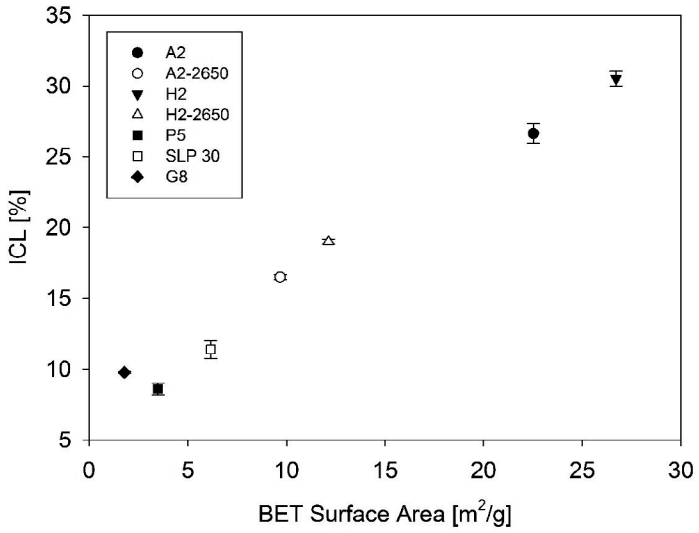

Figure 4.8. Irreversible capacity loss (ICL) vs BET surface area for different graphite samples in 1:2:2 EC:DMC:EMC + 0.9M $LiPF_6$ electrolyte.

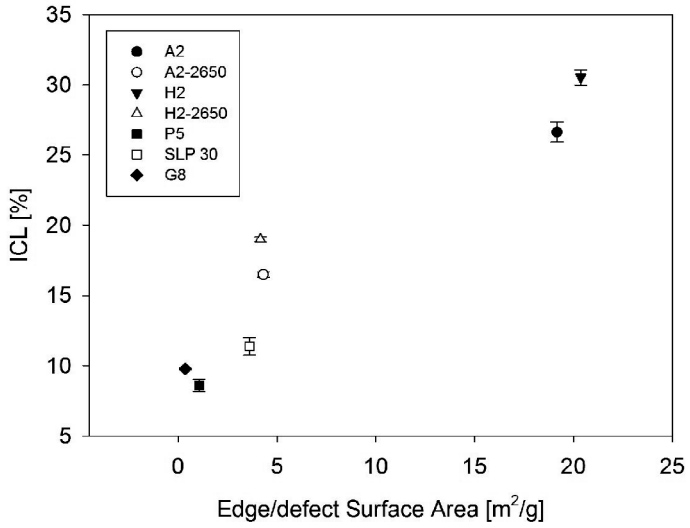

Figure 4.9. Irreversible capacity loss (ICL) vs. Edge/defect (non-basal) surface area for different graphite samples in 1:2:2 EC:DMC:EMC + 0.9M $LiPF_6$ electrolyte.

Fig. 4.10 shows the estimated amount of lithium concentration per m^2 of the total surface area for different graphite samples. The calculations are made under the assumption that most of the irreversible capacity loss (ICL) during the first cycle is due to trapping of lithium species in the SEI film and an evenly distributed SEI on edge, basal and defect sites. This assumption is not entirely correct as XPS studies have shown [25] that the SEI on the basal plane is considerably thinner and contains far less inorganic components compared to the SEI on the edge/defect planes, and therefore it is natural to assume that more lithium is trapped on edges and defects rather than basal sites. Some charge might also be lost due to solvent species co-intercalating during the first cycle, causing some exfoliation [3]. Regardless, these values should not be taken as the absolute amount of lithium, but more as an indirect way to compare the amount of lithium located on edge/basal/defect sites on the different graphite samples. The percentage of edge/basal and defects (obtained from DFT measurements) are also added to more easily illustrate how much of the total surface area these three different sites constitute.

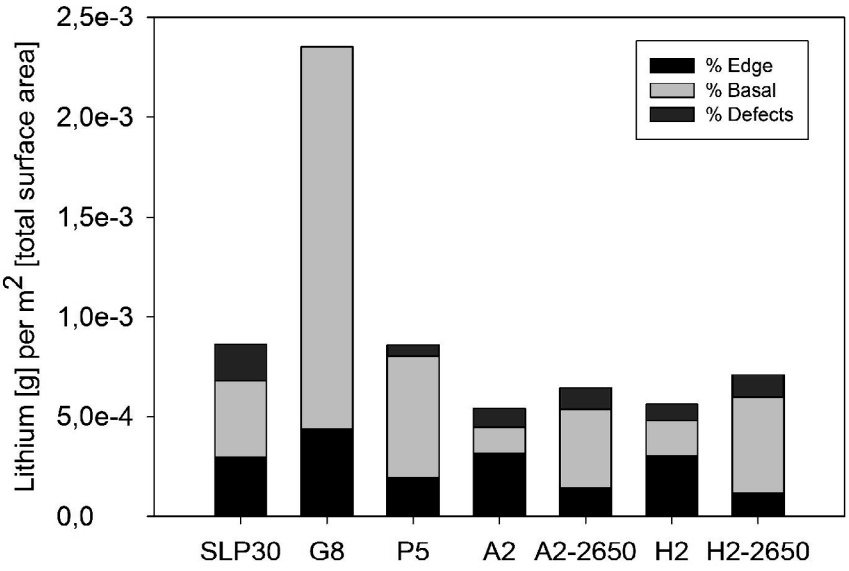

Figure 4.10. Estimated amount of lithium located on the edge/basal and defect sites of different graphite samples in 1:2:2 EC:DMC:EMC + 0.9M $LiPF_6$. Amount of lithium is estimated from ICL.

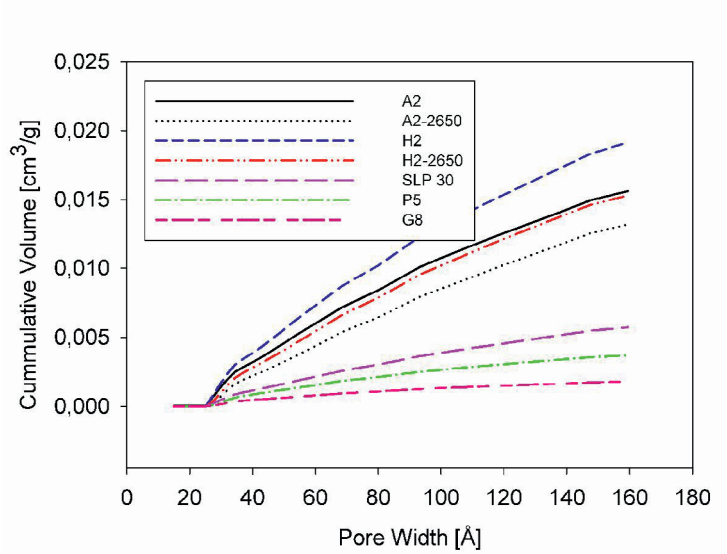

Figure 4.11. Cumulative volume vs. pore diameter for different graphite samples.

Fig. 4.11 shows cumulative pore volume as a function of pore size. It can be seen that the pore volume due to micropores as emerging from the DFT data is basically negligible, and cumulative pore volume is not significant for pores of diameter well below 2 nm. This indicates that the Li-electrolyte complexes are able to access all of the active surface area upon wetting and should be able to intercalate through exposed edge planes and defect sites [26]. There is a clear trend that both A2 and H2 experience a decrease in pore volume upon heat treatment.

Fig. 4.12 shows the thermal response of fully lithiated SLP30, P5 and A2-2650 in 1:2:2 EC:DMC:EMC + 0.9M $LiPF_6$ electrolyte. Notably, the overall heat evolved increases with increasing surface area; A2-2650 > SLP30 > P5. In Fig. 4.13 only P5 and SLP30 are plotted to illustrate a slightly lower onset peak temperature of the first exothermic reaction in P5 (around 101 ^{o}C) compared to SLP30 (around 108 ^{o}C).
To further investigate the effect of surface area on the onset peak temperature for the first exothermic reactions, graphite G8 was studied as well (Fig. 4.14). Fig 4.15 shows a magnified view of the first exothermic reactions, and as is observed, there is a clear trend with increased onset peak temperature for the first exothermic reaction with increasing surface area: SLP30 (6.16 m^2/g and onset peak temperature around 108 ^{o}C) > P5 (3.48 m^2/g and onset peak temperature around 101 ^{o}C) > G8 (1.79 m^2/g and onset peak temperature around 98 ^{o}C).

Fig. 4.16 shows the thermal response of SLP30, P5 and G8 in 4:3:3 EC:DMC:EMC + 0.9M $LiPF_6$ electrolyte. Both P5 and G8 exhibit similar thermal behavior and an onset peak temperature around 100 ^{o}C for the first exothermic reaction, which is comparable to what was observed with the electrolyte 1:2:2 EC:DMC:EMC (Fig. 4.14-4.15). However, SLP30 shows an onset temperature which is considerably higher in 4:3:3 EC:DMC:EMC compared to 1:2:2 EC:DMC:EMC. Fig. 4.17 shows a direct comparison

between these two systems. Notably a higher EC- content increases the thermal stability for SLP30, but not for G8 and P5.

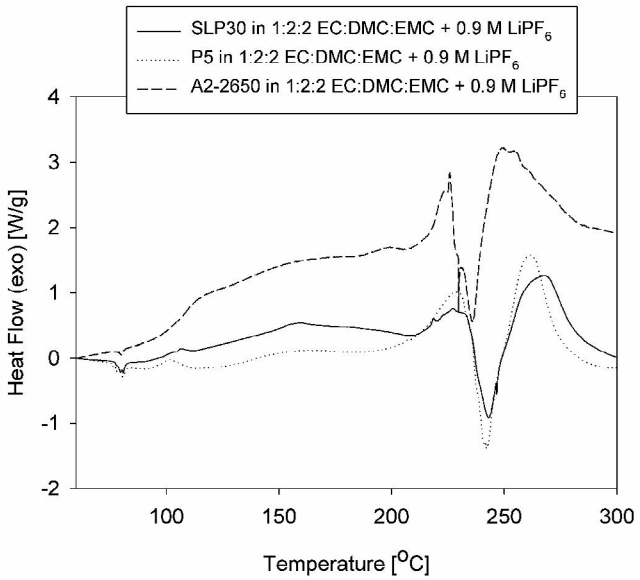

Figure 4.12. Differential scanning calorimetry for fully lithiated graphites (SLP30, P5 and A2-2650) after 60 cycles in 1:2:2 EC:DMC:EMC + 0.9M $LiPF_6$ electrolyte. The heating rate was 2.5 ^oC/min.

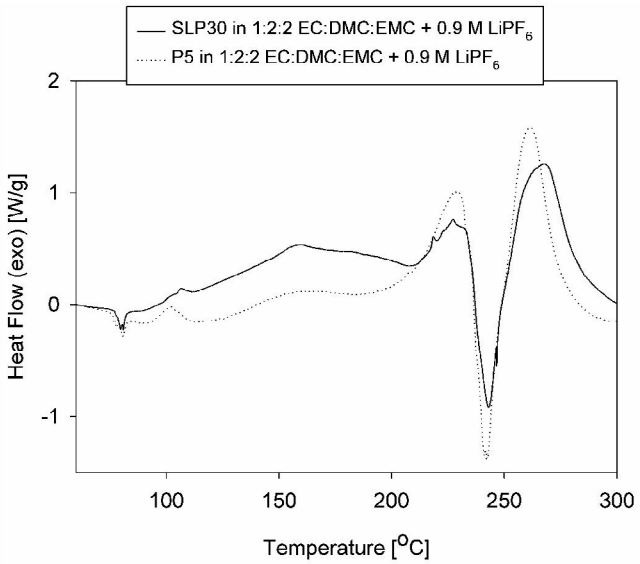

Figure 4.13. Differential scanning calorimetry for fully lithiated graphites (SLP30 and P5 after 60 cycles in 1:2:2 EC:DMC:EMC + 0.9M $LiPF_6$ electrolyte. The heating rate was 2.5 ^oC/min.

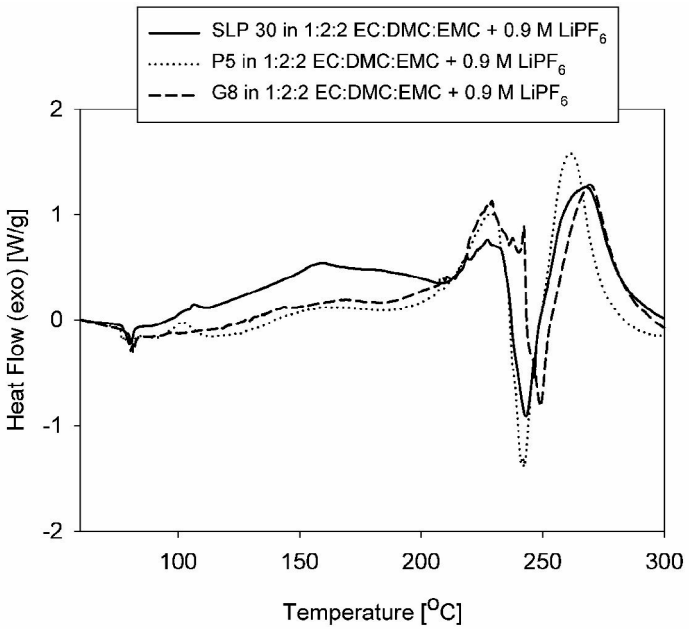

Figure 4.14. Differential scanning calorimetry for fully lithiated graphites (SLP30, P5 and G8) after 60 cycles in 1:2:2 EC:DMC:EMC + 0.9M $LiPF_6$ electrolyte. The heating rate was 2.5 ^{o}C/min.

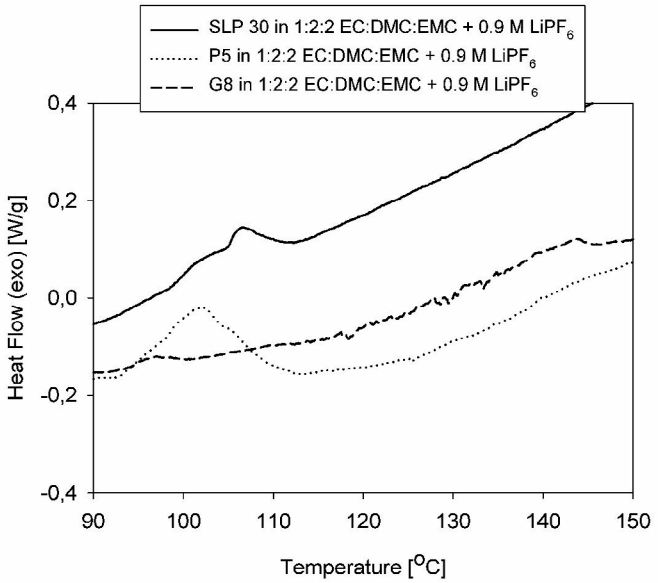

Figure 4.15. Differential scanning calorimetry for fully lithiated graphites (SLP30, P5 and G8) after 60 cycles in 1:2:2 EC:DMC:EMC + 0.9M $LiPF_6$ electrolyte, showing a magnified view of the first exothermic reaction. The heating rate was 2.5 ^{o}C/min.

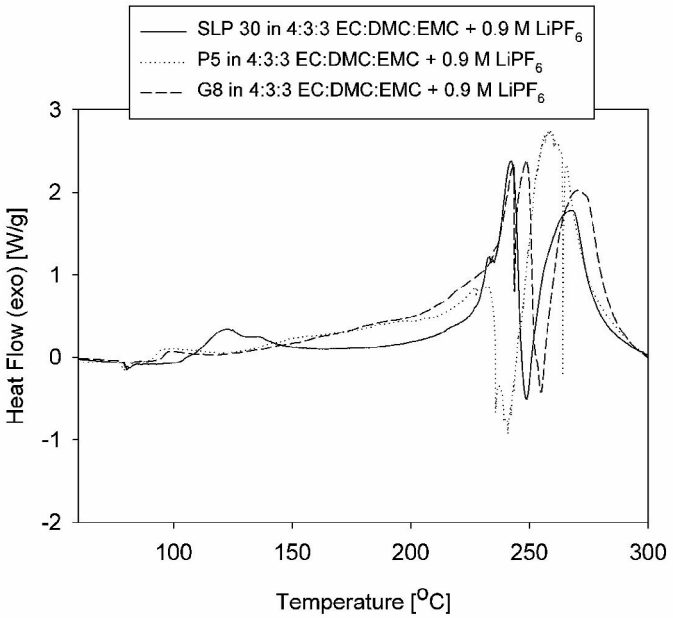

Figure 4.16. Differential scanning calorimetry for fully lithiated graphites (SLP30, P5 and G8) after 60 cycles in 4:3:3 EC:DMC:EMC + 0.9M $LiPF_6$ electrolyte. The heating rate was 2.5 °C/min.

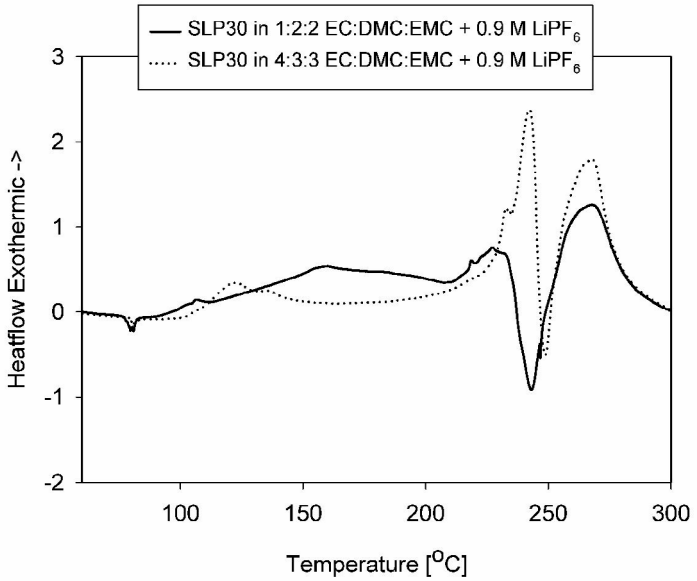

Figure 4.17. Differential scanning calorimetry for fully lithiated graphites SLP30 after 60 cycles in 1:2:2 EC:DMC:EMC + 0.9M $LiPF_6$ and 4:3:3 EC:DMC:EMC + 0.9M $LiPF_6$ electrolyte. The heating rate was 2.5 °C/min.

Fig. 4.18 show SEM images of the graphites utilized in this study, illustrating the difference in morphology. Notably, the commercial graphites, SLP30, P5 and G8 exhibit a rounder shape compared to the raw industrial graphites (A2/H2), which are flakier. This is probably the main reason why A2 and H2 show significantly higher BET surface area compared to the commercial materials.

Fig. 4.19 summarizes the capacity for the different graphites in 1:2:2 EC:DMC:EMC + 0.9M $LiPF_6$ electrolyte at C/8. Of the commercial graphites, SLP30 performs best initially, but experiencing some decay and ending up at about the same capacity as the other materials after 60 cycles at a current density of C/8. The other graphites are initially lower in capacity than SLP30, but in return seem to experience less decay. There is no notable difference between A2/H2 before and after heat treatment.

Fig. 4.20 summarizes the first cycle capacity for the different graphites in 1:2:2 EC:DMC:EMC + 0.9M $LiPF_6$ electrolyte at C/37.2 and compares it with the capacity after 62 cycles for the graphites tested with DSC (P5, G8, SLP30 and A2-2650). The first cycle capacities of the materials are all within a similar range, with a slightly higher value for SLP30 and a bit lower capacity for P5.

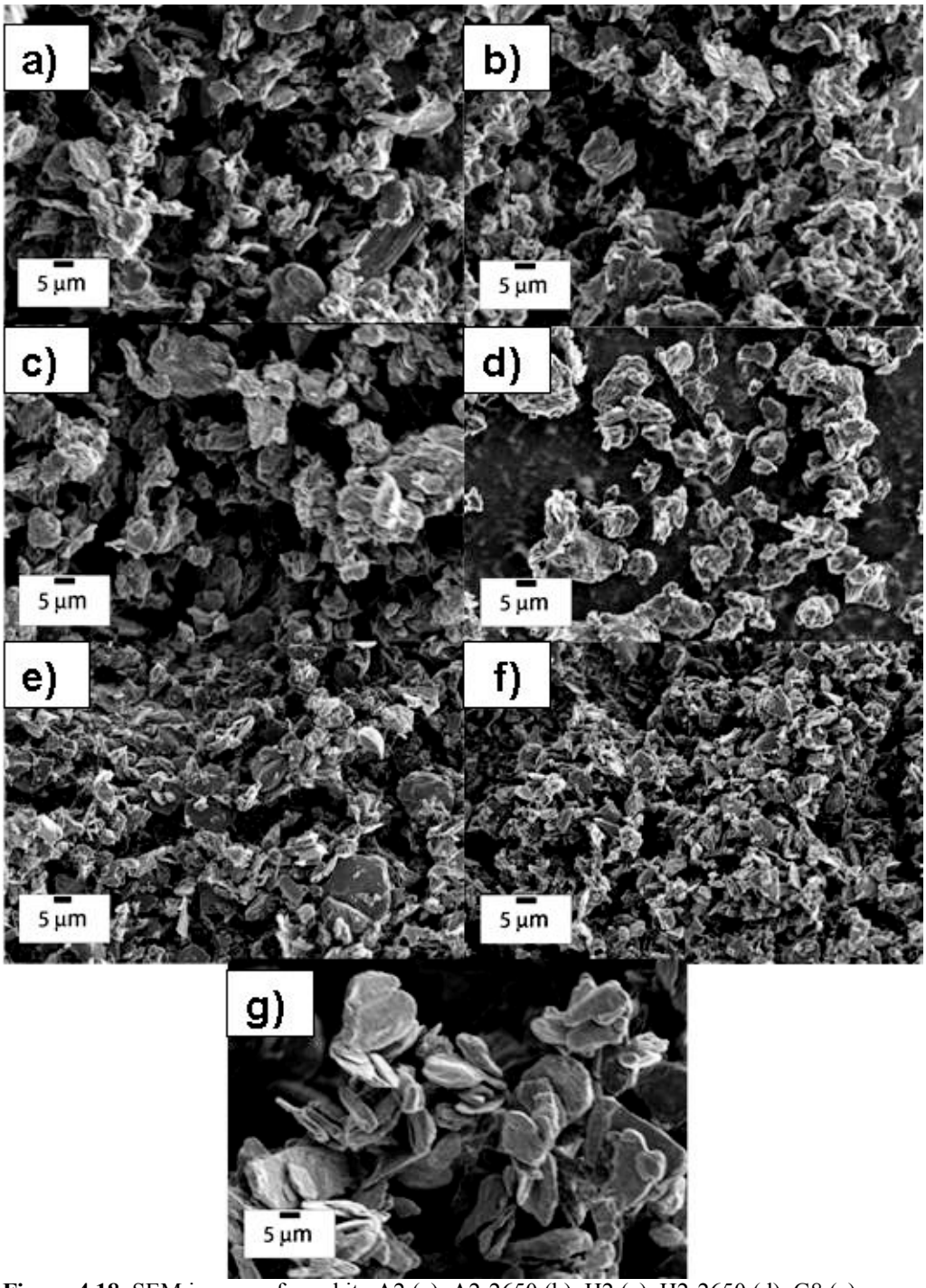

Figure 4.18. SEM images of graphite A2 (a), A2-2650 (b), H2 (c), H2-2650 (d), G8 (e), P5(f) and SLP30 (g).

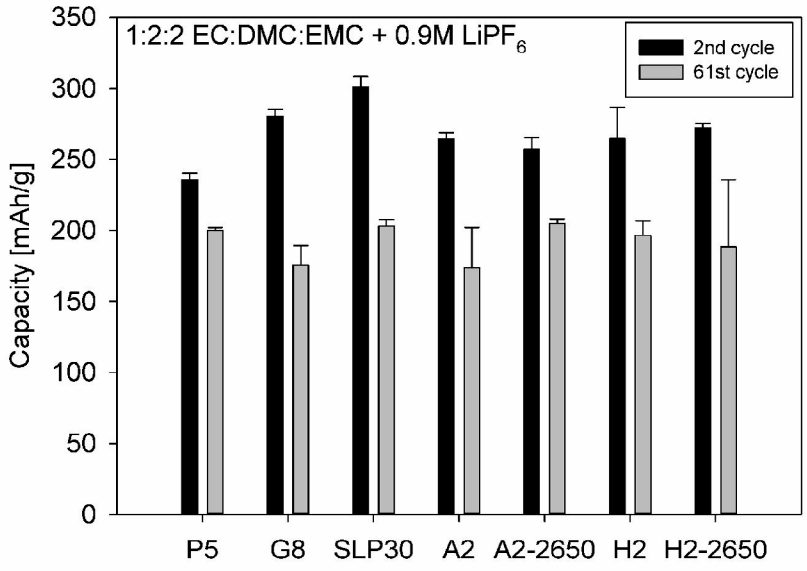

Figure 4.19. Capacity summary for the different graphites in 1:2:2 EC:DMC:EMC + 0.9M $LiPF_6$ electrolyte. Charged/discharged at C/8 (46.5 mA/g).

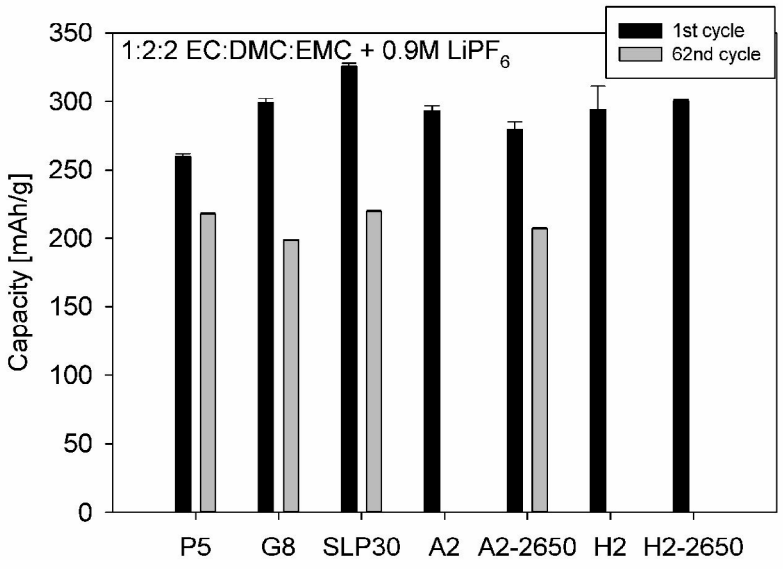

Figure 4.20. Capacity summary for the different graphites in 1:2:2 EC:DMC:EMC + 0.9M $LiPF_6$ electrolyte. Charged/discharged at C/37.2 (10 mA/g).

4.5 Discussion

Thermal stability vs. surface area
Surface area seems to affect the overall heat evolved (Fig. 4.12-4.14). This is reasonable as a larger surface area would cause more SEI to be formed, and the SEI is known to be responsible for the exothermic reactions in the temperature range from 60-230/240 ^{o}C. However, there also seems to be a lower onset temperature for the first exothermic reaction for samples with small surface area (Fig. 4.15).

It was initially believed that the ratio of basal to non-basal plane could be the main reason for this difference in onset temperature due to the fact that both thickness and composition of the SEI is expected to be different on basal planes compared to edge planes and defects. Alternatively, the total amount of lithium trapped in the SEI (estimated from ICL in Fig. 4.10) could also influence the thermal behavior. According to Fig. 4.10, G8 should exhibit significantly different thermal behavior compared to SLP30 and P5, since the amount of lithium trapped in the SEI is potentially higher due to a high ICL compared to a low surface area. The higher ICL to surface area ratio of G8 is very likely the reason why G8 has such a low peak in the initial exothermic reaction, and one could argue that G8 in fact exhibits the better properties in terms of thermal stability, even though the actual onset temperature is similar to P5.

SEM micrographs show that all three materials have similar morphology (Fig. 4.18), and it is therefore reasonable to believe that it is the amount of surface area and not the shape of the surface which is the main factor to consider in terms of thermal stability. However, it should be noted that Cpreme coats their graphite with a uniform homogenous "graphite-on-graphite" coating to reduce surface area, reducing the overall heat evolution, and thereby improving safety. It is suspected that TIMCAL^{TM} also coats their graphite SLP30 due to their smooth potato shaped morphology (Fig. 4.18). If all these commercial graphites are coated it would most likely influence their thermal properties, particularly since it is unknown whether the coating is amorphous or crystalline. It is worth mentioning that the A2/H2 graphites are un-coated and that their morphology is flakier with a less smooth surface, which results in a larger surface area compared to the commercial materials. This is also evident from the larger thermal response of graphite A2-2650 (Fig. 4.12)

Thermal stability for different electrolytes
Increasing the amount of EC in the electrolyte has seemingly negligible effect on the thermal stability of P5 and G8 (Fig. 4.16 vs. Fig 4.14), while SLP30 shows a significant change in behavior. One possibility is that SLP30 requires a higher amount of EC for stable SEI formation due to larger edge/defect surface area compared to P5/G8 (edge/defect surface area is the most active surface towards EC reduction). For SLP30 (Fig. 4.17) the electrolyte with 40 % EC showed a higher onset temperature for the first exothermic reaction compared to the electrolyte with 20 % EC, while the latter exhibited higher heat evolution in the temperature range from 120-240 ^{o}C.

The higher heat evolution can be attributed to the fact that the system with 20 % EC probably has a less compact (more porous) SEI, since it is mainly the decomposition product of EC $(CH_2OCO_2Li)_2$ and Li_2CO_3, which are regarded as the species responsible for providing a compact and passivating SEI [27]. This would allow for easier diffusion of lithium from the graphite structure to the surface, consequently causing reactions with the electrolyte to form stable species (like LiF and Li_2CO_3). This occurs until all sites are blocked [18], leading to a structural collapse around 240 ^oC, which would account for the endothermic peak (exfoliation). The remaining lithium inside the graphite structure is now allowed to react further, as well as the PVDF (which accounts for the last exothermic reaction above 250 ^oC).

The lower onset temperature of the electrolyte with 20 % EC could be explained in the same manner, by a more porous SEI. A more porous structure would, as mentioned, allow for easier reaction between intercalated lithium and the electrolyte. In the electrolyte with 40 % EC, the SEI is expected to consist of very stable passivating species and is probably more compact. There are most likely fewer sites available for reaction between intercalated lithium and the electrolyte. It is therefore reasonable that the exothermic reactions occur at higher temperatures.

Effect of additional heat treatment and milling

Additional heat treatment of the A2/H2 samples seems to have no significant effect on the long term capacity (Fig. 4.19). However from the BET/DFT measurements the HT decreases both the total surface area and edge/defect surface area, which consequently decreased the ICL (Fig. 4.8 and 4.9). The increased L_a values (Table 4.1) could be related to a slightly higher degree of crystallization, as heat treatment above 2650 °C in inert atmosphere is expected to further graphitize the material. DFT data indicate reduced amount of edge planes at the expense of the basal planes with prolonged heat treatment. No significant differences in the amount of defects are observed. The pore volume is decreased upon extended heat treatment (Fig. 4.11), which can be expected due to grain growth and Ostwald ripening. However, none of the graphites investigated here showed any pores in the micropore area (below 2 nm), which indicates that all of the material should be available to the Li-electrolyte complexes and hence active towards lithium intercalation.

According to Fig. 4.19 and 4.20 there is no significant difference in performance between the two milling types. The Highcom milled H- materials are slightly higher in capacities vs. the Alpine milled A-materials. However, the Alpine mill resulted in slightly lower BET surface areas compared to the Highcom mill, which ultimately led to slightly lower ICL. DFT measurements gave clear indication that the amount of edge planes decreased upon extended heat treatment at the expense of basal planes for both A2 and H2. Interestingly, the remaining edge planes showed significantly lower adsorption potentials which would usually mean a lower density of carbon atoms. The reason for this is unclear, but the results showed a slightly improved capacity upon cycling for heat treated A2, while the capacity for heat treated H2 upon extended cycling showed a slight decrease compared to the non-heat treated material. All in all the changes due to extended heat treatment was not significant.

4.6 Conclusion

The thermal response of graphite in lithium ion batteries show a clear correlation with total amount of surface area (according to previous studies in the literature [28]) and total heat evolved. However, commercial graphite with low surface area (G8 and P5) showed a lower onset temperature for exothermic reactions (related to conversion of meta-stable species in the SEI to more stable compounds) compared to commercial graphite with larger surface area (SLP30).

Higher relative EC content in the electrolyte led to a higher onset temperature (better thermal stability) for exothermic reactions compared to lower EC content for SLP30. There is likely a correlation between a more stable SEI (consisting of stable species like Li_2CO_3 and $(CH_2OCO_2Li)_2$) and the onset temperature. Graphites with high amounts of edge planes require more EC to ensure good SEI formation and consequently better thermal properties.

Heat treatment of industrial graphite reduced the overall surface area and caused a decrease in total pore volume and BET surface area, as investigated by DFT measurements. The heat treatment showed no significant improvement in capacity except for the apparent reduction in the overall ICL.

There seem to be a trend that ICL, amount edge/defect, and amount of EC (all related to formation of stable SEI), can influence the thermal stability. High ICL and low edge/defects area are indicative of a stable SEI with good thermal properties in terms of overall heat evolved. One of the main conclusions from the data presented here is that DFT measurements, coupled with ICL data, could be a potentially useful tool to predict thermal stability behavior of graphites in Li-ion batteries.

Acknowledgments

The Norwegian Research Council (grant number 195432/S10), SINTEF, and NTNU. The industrial partners, Elkem Carbon AS, Miljøbil Grenland AS and Carbontech Holding AS are acknowledged for their co-funding of the project.

References

1. K. Mizushima, et al., *LixCoO2 (0<x<-1): A new cathode material for batteries of high energy density.* Materials Research Bulletin, 1980. **15**(6): p. 783-789.
2. E. Peled, *The Electrochemical-Behaviour of Alkali and Alkaline-Earth Metals in Non-Aqueous Battery Systems - The Solid Electrolyte Interphase Model.* Journal of the Electrochemical Society, 1979. **126**(12): p. 2047-2051.
3. J.O. Besenhard, et al., *Filming mechanism of lithium-carbon anodes in organic and inorganic electrolytes.* Journal of power sources, 1995. **54**(2): p. 228-231.
4. D. Aurbach, et al., *On the correlation between surface chemistry and performance of graphite negative electrodes for Li ion batteries.* Electrochimica Acta, 1999. **45**(1): p. 67-86.
5. S.H. Ng, et al., *Correlations between surface properties of graphite and the first cycle specific charge loss in lithium-ion batteries.* Carbon, 2009. **47**(3): p. 705-712.
6. P. Novák, et al., *The importance of the active surface area of graphite materials in the first lithium intercalation.* Journal of power sources, 2007. **174**(2): p. 1082-1085.
7. T. Placke, et al., *Influence of graphite surface modifications on the ratio of basal plane to non-basal plane surface area and on the anode performance in lithium ion batteries.* Journal of power sources, 2011. **200**(0): p. 83-91.
8. J.P. Olivier and M. Winter, *Determination of the absolute and relative extents of basal plane surface area and "non-basal plane surface" area of graphites and their impact on anode performance in lithium ion batteries.* Journal of power sources, 2001. **97-98**: p. 151-155.
9. J.P. Olivier and S. Ross, *On Physical Adsorption. XVI. The Physical Interaction of H2, D2, CH4, and CD4 with Graphite.* Proceedings of the Royal Society of London. Series A. Mathematical and Physical Sciences, 1962. **265**(1323): p. 447-454.
10. F. Joho, et al., *Relation between surface properties, pore structure and first-cycle charge loss of graphite as negative electrode in lithium-ion batteries.* Journal of power sources, 2001. **97-98**: p. 78-82.
11. T. Tran and K. Kinoshita, *Lithium intercalation deintercalatation behaviour of basal and edge planes of highly oriented pyrolytic-graphite and graphite powder.* Journal of Electroanalytical Chemistry, 1995. **386**(1-2): p. 221-224.
12. Y. NuLi, J. Yang, and Z. Jiang, *Intercalation of lithium ions into bulk and powder highly oriented pyrolytic graphite.* Journal of Physics and Chemistry of Solids, 2006. **67**(4): p. 882-886.
13. A. Funabiki, M. Inaba, and Z. Ogumi, *A.c. impedance analysis of electrochemical lithium intercalation into highly oriented pyrolytic graphite.* Journal of power sources, 1997. **68**(2): p. 227-231.
14. Y. Yamada, K. Miyazaki, and T. Abe, *Role of Edge Orientation in Kinetics of Electrochemical Intercalation of Lithium-Ion at Graphite.* Langmuir. **26**(18): p. 14990-14994.

15. E.P. Roth and D.H. Doughty, *Thermal abuse performance of high-power 18650 Li-ion cells.* Journal of power sources, 2004. **128**(2): p. 308-318.
16. M.N. Richard and J.R. Dahn, *Accelerating rate calorimetry study on the thermal stability of lithium intercalated graphite in electrolyte I. Experimental.* Journal of the Electrochemical Society, 1999. **146**(6): p. 2068-2077.
17. O. Haik, et al., *On the Thermal Behavior of Lithium Intercalated Graphites.* Journal of the Electrochemical Society, 2011. **158**(8): p. A913-A923.
18. H. Yang, et al., *Investigations of the exothermic reactions of natural graphite anode for Li-ion batteries during thermal runaway.* Journal of the Electrochemical Society, 2005. **152**(1): p. A73-A79.
19. A.M. Andersson and K. Edstrom, *Chemical Composition and Morphology of the Elevated Temperature SEI on Graphite.* Journal of the Electrochemical Society, 2001. **148**(10): p. A1100-A1109.
20. S.S. Zhang, K. Xu, and T.R. Jow, *Optimization of the forming conditions of the solid-state interface in the Li-ion batteries.* Journal of power sources, 2004. **130**(1-2): p. 281-285.
21. K. Kanamura, et al., *Morphology and chemical-compositions of surface-films of lithium deposited on a Ni substrate in nonaqueous electrolytes.* Journal of Electroanalytical Chemistry, 1995. **394**(1-2): p. 49-62.
22. N. Iwashita, et al., *Specification for a standard procedure of X-ray diffraction measurements on carbon materials.* Carbon, 2004. **42**(4): p. 701-714.
23. J. Olivier, Adsorption of carbons, 2008: p. CH7.
24. J. Olivier and M. Winter, *Determination of the absolute and relative extents of basal plane surface area and "non-basal plane surface" area of graphites and their impact on anode performance in lithium ion batteries.* Journal of power sources, 2001. **97-8**: p. 151-155.
25. E. Peled, et al., *Effect of carbon substrate on SEI composition and morphology.* Electrochimica Acta, 2004. **50**(2-3): p. 391-395.
26. H.T. Zhou, M.A. Einarsrud, and F. Vullum-Bruer, *High capacity nanostructured Li2FexSiO4/C with Fe hyperstoichiometry for Li-ion batteries.* Journal of power sources. **235**: p. 234-242.
27. D. Aurbach, et al., *New insights into the interactions between electrode materials and electrolyte solutions for advanced nonaqueous batteries.* Journal of power sources, 1999. **81**: p. 95-111.
28. F. Joho, P. Novak, and M.E. Spahr, *Safety aspects of graphite negative electrode materials for lithium-ion batteries.* Journal of the Electrochemical Society, 2002. **149**(8): p. A1020-A1024.

5. Temperature effects on graphite capacity for various electrolytes used in lithium ion batteries

5.1 Summary

The performance of graphite electrodes in various ethylene carbonate and propylene carbonate based electrolytes at temperatures below room temperature has been studied, and compared to electrodes cycled at room temperature with the same electrolyte. Electrodes cycled at low temperature showed increased capacity fade as compared to electrodes cycled at room temperature. Differential scanning calorimetry (DSC) has been employed to investigate phase transitions at lower temperature and safety issues at elevated temperatures. Based on these results, as well as the results from cycling, suitable electrolytes, able to work in a wide temperature range, could be identified. The stability of the graphite electrode upon extended cycling was found to increase with the amount of EC. This was verified by the fact that an electrolyte with 40 % EC outperformed one with 20 % EC after more than 200 deep discharge cycles, although the one with 20 % EC was initially better. Addition of PC to a multi-component system, making the total amount of cyclic carbonates 40 % (i.e. 20 % EC and 20 % PC), increased the liquid temperature range of the electrolyte, and showed long term stability comparable to the electrolyte with 20 % EC. However, the addition of PC reduced the capacity considerably at i.e. 0 ^{o}C, and also led to very high initial irreversible capacity loss.

Highlights

We have investigated the graphite capacity for various electrolyte systems.
The electrolyte systems have been evaluated by differential scanning calorimetry.
Electrochemical performance has been evaluated.
Low temperature cycling of graphite exhibited more degradation compared to cycling at room temperature.

Keywords; Lithium ion battery, graphite, low temperature cycling, differential scanning calorimetry, non-aqueous electrolyte

5.2 Introduction

In order for Li-ion batteries (LIB) to be a competitive alternative to the internal combustion engine in vehicles, significant improvements in cost, cycle life, power density and safety are required. In addition, it is of vital importance that the temperature window of LIB is increased, ensuring good performance of the LIB in electric vehicles (EV) in cold and warm climates. Graphite is the dominating choice as anode material, due to low cost and availability, combined with high capacity and reasonably stable performance. The most common electrolyte choice with graphite has been a mixture of linear carbonates, such as diethylene carbonate (DEC), dimethyl carbonate (DMC) and ethyl methyl carbonate (EMC), with cyclic carbonates, such as ethylene carbonate (EC) and propylene carbonate (PC). Ethylene carbonate (EC) is always added due to its ability to form a protective film, commonly called the solid electrolyte interphase (SEI) [1], during the first cycle of operation. The SEI layer is crucial for the stable operation of graphite anodes, as the intercalation potential lies below the electrochemical potential window of the electrolyte. In fact, the replacement of PC with EC was one key to success for the first commercialization of LIBs, as PC causes exfoliation of the graphite, leading to significant capacity loss during cycling.

The main factors affecting the electrochemical performance of graphite at low temperature are; i) Properties of the SEI ii) the reduction of electrolyte conductivity upon reduction of the temperature [2], iii) low lithium ion diffusion in the carbon anode [3]. SEI properties and poor SEI formation can be largely related to electrolyte choice as it is generally considered that Li_2CO_3 or $(CH_2OCO_2Li)_2$ (which is the major decomposition product of EC) are superior with regards to graphite passivation and stability for long term operation [4]. Studies on optimizing formation conditions for the SEI showed that good ionic conductivity resulted in poor SEI stability, and vice versa [5], meaning that species providing good long term stability of graphite (Li_2CO_3 or $(CH_2OCO_2Li)_2$) also caused a higher interfacial resistance compared to the more soluble SEI species. However, the more soluble species will not passivate the SEI properly and consequently will lead to more solvent reduction (capacity fade) upon cycling. One disadvantage of using EC is that it has a high melting point which causes a drop in conductivity and poor performance at low temperatures. PC on the other hand has a much lower melting point compared to EC. In a study comparing 3:7 EC:EMC and 1:1:3 EC:PC:EMC in full cells, the cell with PC containing electrolyte was found to have a lower capacity at room temperature, but a lower relative loss in the temperature range 0 to -20 ^{o}C. This was attributed to a higher ionic conductivity through the SEI film at low temperatures, as determined by impedance spectroscopy, compared to EC based electrolytes [6]. When attempting to decrease the overall melting point of a binary electrolyte system, it was found that the best results were achieved by mixing species with similar melting points and molecular structure [7]. DEC was found to have the least effect on the electrolyte liquidus temperature, even though pure DEC is among the electrolyte solvents with the lowest melting point.

Mixing of EC with PC (species of similar molecular structure) would presumably result in a significant decrease of the melting point and consequently improve the low

temperature properties. However, a mixture of EC and PC alone would result in a solution with very high viscosity due to the high dielectric constant of both these solvents. The addition of linear carbonates is necessary to improve properties like viscosity, wettability and conductivity. For example, a high EC content is known to cause higher anodic polarization (due to higher film resistance through the SEI) and is therefore also more susceptible towards lithium plating [8], but it provides a more stable SEI, which is necessary for cycle life. The higher polarization caused by the EC content could be related to the de-solvation energy [9-12], which has been shown to be the major energy-consuming step and the largest contributor to the overall charge transfer resistance [13]. The high affinity of EC towards the lithium ion contributes to a higher de-solvation energy which would cause increased electrode resistance and poorer transport properties of Li-ions through the SEI. Hence, decreasing the amount of EC in the solution would force more linear carbonates (which have lower affinity) to solvate the lithium. This would presumably result in lower charge transfer resistance and higher diffusion through the SEI, giving a battery with high performance and rate capability. However, this would be at the expense of long term stability, as EC is very important for the formation of a stable SEI film.

Many studies have tried to improve the capacity fading at lower temperature by developing electrolytes with high conductivities and good solid electrolyte interphase formation [14-18]. It is generally agreed upon that conductivity plays an important part with regards to low temperature operation, as it will generally decrease upon cooling due to lower mobility of electrolyte species. Conductivity measurements on electrolytes with high EC content even reported no conductivity at -10 ^{o}C, which was believed to be due to the solidification of the EC component [19]. Bulk conductivity measurements for multi-component (ternary/quaternary) systems containing several alkyl carbonates showed much better low temperature conductivity compared to binary solutions [20]. To achieve this high conductivity at low temperatures, they used DEC and esters in a multi-component system. The importance of using additives, like vinylene carbonate (VC), has also been highlighted due to the incompatibility of some of these components with graphite, as DEC, while providing improved low temperature conductivity, is known to reduce the stability of the graphite anodes [18] and provide poor SEI stability (affecting the cycle life). Also some esters have shown reactivity towards the anode (causing degradation) [17], while others in fact showed promising results towards low temperature operation down to -60 ^{o}C [14]. These good results were primarily achieved by fixing the EC-content to 20 % and the ester co-solvent to 20 %.

Development of low temperature electrolytes is important from a safety aspect as well. Good transport properties can prevent lithium plating by minimizing the polarization occurring at lower temperatures due to decreased kinetics and conductivity. Lithium plating was recently investigated in various electrolyte compositions (high/low EC content and with/without VC additive) [8], showing a correlation between a highly resistive SEI film and lithium plating. Surface modification (carbon coating with chemical vapor deposition (CVD)) was found to suppress lithium deposition to some extent compared to samples without coating [21]. This was also attributed to good transport properties through the SEI.

In this study the effect of EC and the addition of PC to a multi-component system have been investigated. The electrolyte compositions investigated were selected from those typically found in the literature [6, 14, 20, 22], and are expected to work in a wide temperature range. In addition, one commonly applied (in laboratory experiments) binary electrolyte was included for comparison (1:1 EC:DEC). The various electrolytes were evaluated based on reversible and irreversible capacity in the temperature range 0 to 40 ^{o}C, capacity fade after repeated cycles, as well as differential capacity curves providing the shifts of intercalation potentials. Thermal stability of cycled electrodes was determined by differential scanning calorimetry (DSC). The DSC analysis performed at high temperatures for the graphite anodes, after the SEI is formed, can provide important information about the safety of the different electrolytes as it is often the heat development on the anode that initiates further (and more energetic) exothermic reactions on the cathode, leading to thermal runaway [23].

Our goal is to determine whether 20 % EC is sufficient to provide formation of a stable film on the graphite surface and investigate the effect of more EC on lower temperature cycling. An addition of PC to an EC:DMC:EMC system would presumably decrease the solidus temperature, thereby keeping the electrolyte in a liquid state at much lower temperatures. The effect of adding PC has been investigated, both thermally and electrochemically, to investigate if the benefits of improved low temperature properties can make up for the expected exfoliation caused by the PC based electrolytes. Causes of loss of capacity at low temperatures will be investigated by electrochemical techniques (impedance spectroscopy and differential capacity curves). Finally, we would like to investigate if there is any additional degradation occurring during the low temperature cycling of graphite compared to room temperature cycled cells. We also report on an interesting phenomenon, where the final stage formation of 1:1 EC:DEC + 1 % VC electrolyte disappears upon cycling at lower temperatures, only to reappear after cycling at elevated temperature.

5.3 Experimental

Graphite SLP30 was used as received from TIMCAL^{TM}. The graphite electrodes were prepared by tape casting a slurry consisting of 37 g SLP30, 2 g poly-vinylidene fluoride (PVDF) (Kynar, reagent grade), 1 g Super P carbon black (TIMCAL^{TM}), and 60 g 1-methyl-2-Pyrrolidinone (NMP) (Sigma-Aldrich, > 99 %) onto a 10 µm thick Cu-foil current collector from Circuit foil Luxembourg. The tape caster was a "K Control Coater" from Printcoat instruments. The casts were dried in a vacuum oven at 120 ^{o}C overnight.

The electrolytes were made using varying amounts (in weight %) of ethylene carbonate (Sigma-Aldrich, > 99 %), diethyl carbonate (Aldrich, > 99 %), vinylene carbonate (VC) (Aldrich, 97 %), ethyl methyl carbonate (Merck, > 99 %), ethyl acetate (Sigma-Aldrich, 99,8 %), dimethyl carbonate (Sigma-Aldrich, > 99 %) and propylene carbonate (Sigma-Aldrich, 99,7 %) with 0.9 M $LiPF_6$ (Aldrich, > 99.99 %), as presented in Table 5.1.

Table 5.1. Electrolyte compositions

Electrolyte	Electrolyte amount
1:1 EC:DEC 0.9 M $LiPF_6$ +1 % VC	30 µl
1:1:3 EC:PC:EMC 0.9 M $LiPF_6$	30 µl
1:1:3 EC:EA:EMC 0.9 M $LiPF_6$	30 µl
2:2:3:3 EC:PC:DMC:EMC 0.9 M $LiPF_6$	30 µl
1:2:2 EC:DMC:EMC 0.9 M $LiPF_6$	30 µl
4:3:3 EC:DMC:EMC 0.9 M $LiPF_6$	30 µl

Reduction/oxidation of graphite was recorded with a model 4200 potentsiostat from Maccor connected to a temperature chamber also supplied by Maccor. Before low temperature cycling and DSC measurements all cells were cycled galvanostatically at 10 mAh/g between 5 and 1500 mV, followed by four cycles at 46.5 mAh/g to ensure complete SEI formation. The temperature cycles followed a program summarized in Fig. 5.1, where the coin cells rested for 2 hours at each temperature to ensure a uniform temperature in the cell during cycling. Electrochemical impedance spectroscopy (EIS) was performed using a Zahner IM6 potentsiostat with a frequency range from 5 mHz to 1 MHz with an amplitude of 5 mV.

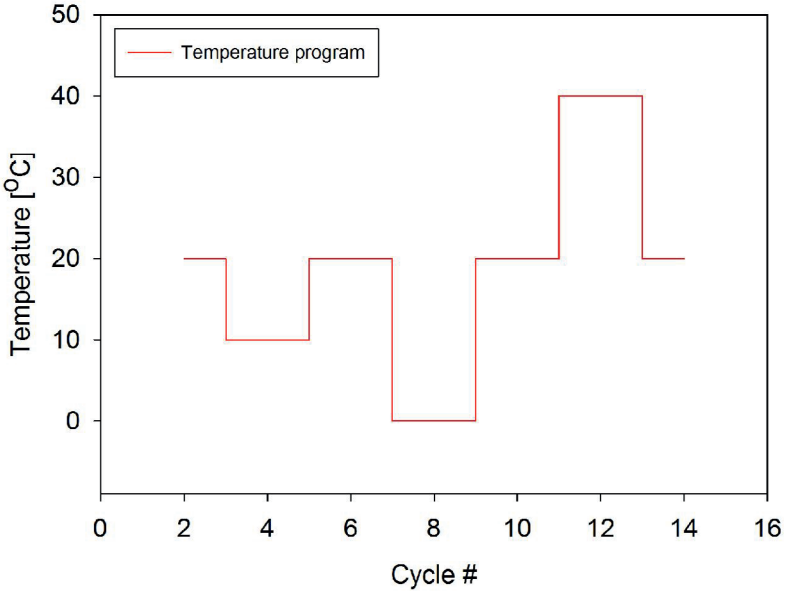

Figure 5.1. Temperature program used during reduction/oxidation curves of coin cells with graphite/lithium half-cells

The reduction/oxidation curves were acquired using graphite/lithium half-cells assembled as coin cells provided by Hohsen Corp. For the electrochemical impedance a three-electrode cell of the model "HS-3E test cell" by Hohsen Corp was used. The cells were assembled in inert atmosphere inside an argon-filled glove-box (O_2 and H_2O < 0.1 ppm). The cells consisted of a graphite working electrode (2.01 cm^2) with a loading of about 3-4 mg/cm^2, a 20 µm thick separator (Celgard® 2320), a 0.75 mm thick lithium foil (1.54 cm^2) as counter electrode, and a lithium strip as reference electrode. All potentials are reported vs. Li/Li^+ unless otherwise specified.

For the differential scanning calorimetri (DSC) measurements a DSC Q100 from TA Instruments was used for the low temperature analyses while a PerkinElmer DSC 7 was used for the high temperature analyses. The temperature range for the high temperature measurements was from 30 to 300 ^oC with 2.5 ^oC /min heating rate. For the high temperature testing 3 samples of 5 mm diameter were cut out from fully lithiated graphite electrodes obtained from disassembled coin cells. They were then placed in gold plated stainless steel high pressure capsules (from PerkinElmer), together with 3 µl of the same electrolyte used in that specific battery system, and completely sealed. The low temperature measurements were performed by cooling down to -85 ^oC before heating up to 50 ^oC with a heating rate of 5 ^oC/min. All sample preparation was done inside a glove box to keep the atmosphere inert. For the low temperature testing, 5 µl of pure electrolyte was placed in a Tzero aluminium sample pan (from TA instruments), which was hermetically sealed.

5.4 Results

Table 5.2 summarizes the initial charge capacity and the irreversible capacity loss (ICL) of the different electrolyte compositions. In the table we also see the capacity after the coin cells were subjected to temperature variations.

Table 5.2. Summary of electrolyte performance at a constant current 10 mAh/g before and after the coin cells were subjected to temperature variations
(Standard deviations for n = 4 unless otherwise specified)

Electrolyte	1st Lithiation Capacity (mAh/g)	ICL (%)	Lithiation capacity after 17 temperature cycles (mAh/g) (n = 2)	Percentage capacity retained after 17 temperature cycles (%)
1:1 EC:DEC 0.9 M $LiPF_6$ +1 % VC	392 ± 9.21	13.02 ± 0.2	315 ± 0.1	92.4
1:1:3 EC:PC:EMC 0.9 M $LiPF_6$	459 ± 25.0	26.74 ± 3.2	278 ± 5.1	83.4
1:1:3 EC:EA:EMC 0.9 M $LiPF_6$	378 ± 12.8	11.67 ± 0.9	15 ± 1.7	4.59
2:2:3:3 EC:PC:DMC:EMC 0.9 M $LiPF_6$	470 ± 20.7	30.68 ± 2.2	285 ± 9.2	87.3
1:2:2 EC:DMC:EMC 0.9 M $LiPF_6$	377± 12.4	11.39 ± 0.3	311 ± 4.2	92.3
4:3:3 EC:DMC:EMC 0.9 M $LiPF_6$	377± 12.0	12.12 ± 0.5	304 ± 2.2	91.7

In Fig. 5.2a the low temperature DSC curves of various electrolytes are plotted. We can identify that the liquid to solidus transition temperature for the pure electrolyte of 1:1 EC:DEC + 1 % VC + 0.9 M $LiPF_6$ is around 10 ^oC (Fig. 5.2b), which is most likely the EC component solidifying. The 4:3:3 EC:DMC:EMC + 0.9 M $LiPF_6$ electrolyte does not have an endothermic peak until around -10 ^oC , while the remaining electrolytes show no sign of a solidus transition until around -30 ^oC and/or lower.

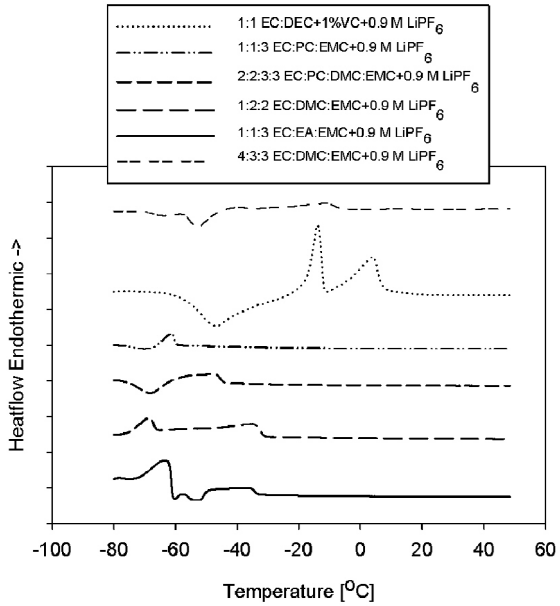

Figure 5.2a. DSC response of pure electrolytes. Endothermic peaks are upwards.

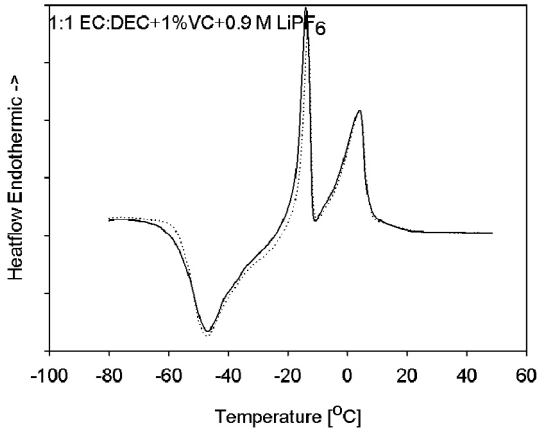

Figure 5.2b. DSC response of electrolyte 1:1 EC:DEC + 1 % VC + 0.9 M $LiPF_6$. Endothermic peaks are upwards.

Fig. 5.3a shows the high temperature DSC curves for fully lithiated graphite electrodes, after they were subjected to cycling between 0 and 40 ^{o}C (at C/8). The electrolyte containing ethyl acetate (EA) exhibited the earliest onset temperature for exothermic reaction, followed by 1:1 EC:DEC + 0.9 M $LiPF_6$ +1 % VC. The remaining four electrolytes displayed similar onset temperatures around 115-125 ^{o}C. Fig. 5.3b compares the thermal response of room temperature cycled graphite vs. low temperature cycled graphite in 4:3:3 EC:DMC:EMC + 0.9 M $LiPF_6$ electrolyte. No apparent difference can be observed.

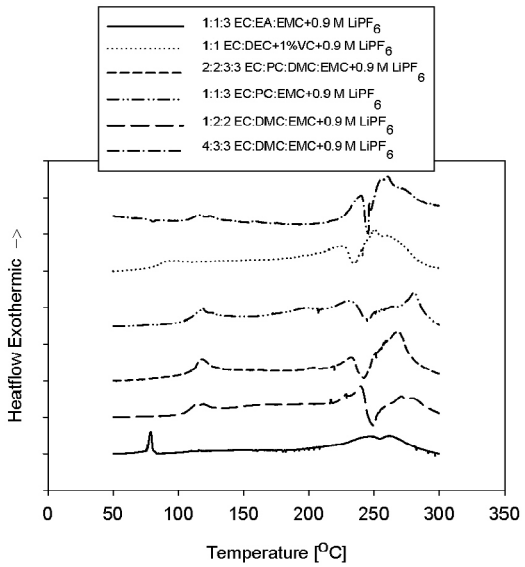

Figure 5.3a. DSC response of electrolytes after SEI formation and subjected to temperature cycles in fully lithiated samples of SLP30. Exothermic peaks are upwards.

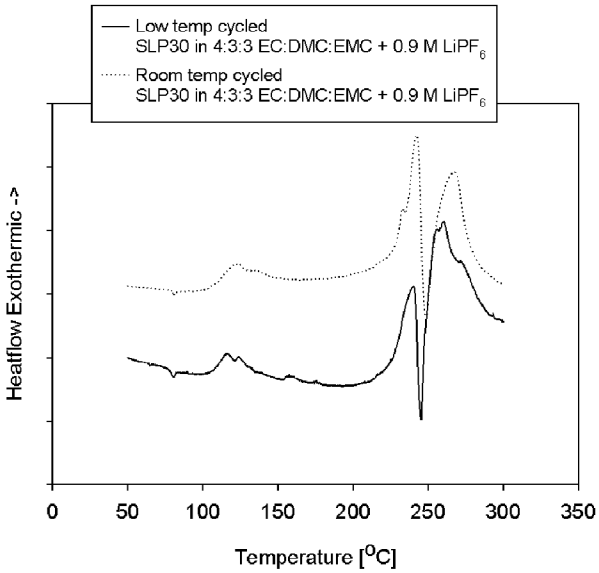

Figure 5.3b. DSC response of fully lithiated room temperature cycled graphite SLP30 (dotted line) vs. fully lithiated temperature cycled SLP30 (solid line) in 4:3:3 EC:DMC:EMC + 0.9 M $LiPF_6$ electrolyte. Exothermic peaks are upwards.

Table 5.3 summarizes and compares the capacity after extended cycling at room temperature for three different electrolytes. These electrolytes were selected to compare the effect of 20 % EC with 40 % (1:2:2 EC:DMC:EMC + 0.9 M $LiPF_6$ vs. 4:3:3 EC:DMC:EMC + 0.9 M $LiPF_6$) and to investigate the effect achieved by replacing some EC with PC (2:2:3:3 EC:PC:DMC:EMC + 0.9 M $LiPF_6$). According to the data, 40 % EC improved the stability compared to 20 % EC. The 4:3:3 EC:DMC:EMC + 0.9 M $LiPF_6$ electrolyte was notably better in terms of extended cycling.
Replacement of 20 % EC with PC (overall 40 % cyclic carbonates) in the 2:2:3:3 EC:PC:DMC:EMC + 0.9 M $LiPF_6$ electrolyte showed comparable results to 1:2:2 EC:DMC:EMC + 0.9 M $LiPF_6$ electrolyte with respect to extended cycling.

Table 5.3. Summary of electrolyte performance at a constant current of 10 mAh/g (C/37.2) after extended cycling (at C/8 and C/4 in room temperature)
(Standard deviations for n = 4 unless otherwise specified)

Electrolyte	1st De-lithiation capacity (mAh/g)	De-lithiation capacity after 61 cycles (mAh/g)	ICL (%)	Percentage capacity retained after 61 cycles (n = 3)	Percentage capacity retained after 213 cycles (n = 3)
SLP30- 2:2:3:3 EC:PC:DMC:EMC 0.9 M $LiPF_6$	332 ± 5.9	238 ± 7.6	28.10 ± 5.5	**71.7 %**	192 ± 4.9 (57.8 %)
SLP30- 4:3:3 EC:DMC:EMC 0.9 M $LiPF_6$ (n=3)	331 ± 3.8	269 ± 2.7	12.01 ± 0.1	**81.3 %**	217 ± 7.1 (65.8 %)
SLP30- 1:2:2 EC:DMC:EMC 0.9 M $LiPF_6$	326 ± 2.2	232 ± 1.2	11.69 ± 0.1	**71.2 %**	183 ± 4.9 (56.1 %)

Fig. 5.4 summarizes the cycling capacity in Table 5.3 for three different electrolytes (1:2:2 EC:DMC:EMC + 0.9 M $LiPF_6$, 2:2:3:3 EC:PC:DMC:EMC + 0.9 M $LiPF_6$, 4:3:3 EC:DMC:EMC + 0.9 M $LiPF_6$) at C/37.2 rate.
Fig. 5.5 compares the cycle capacity for the same electrolyte systems, but at a cycling rate of C/8. Here, the difference between 1:2:2 EC:DMC:EMC + 0.9 M $LiPF_6$ and 2:2:3:3 EC:PC:DMC:EMC + 0.9 M $LiPF_6$ and 4:3:3 EC:DMC:EMC + 0.9 M $LiPF_6$ is marginal, but 4:3:3 EC:DMC:EMC + 0.9 M $LiPF_6$ is slightly better after 61 cycles (232 mAh/g) compared to the other two electrolytes.

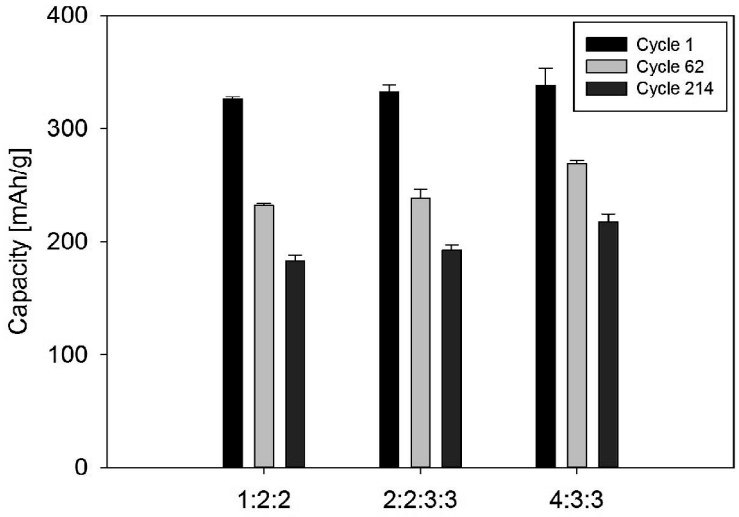

Figure 5.4. Cycle capacity at C/37.2 for different electrolytes (1:2:2 EC:DMC:EMC + 0.9 M $LiPF_6$, 2:2:3:3 EC:PC:DMC:EMC + 0.9 M $LiPF_6$, 4:3:3 EC:DMC:EMC + 0.9 M $LiPF_6$) with graphite SLP30/Lithium half-cells at room temperature.

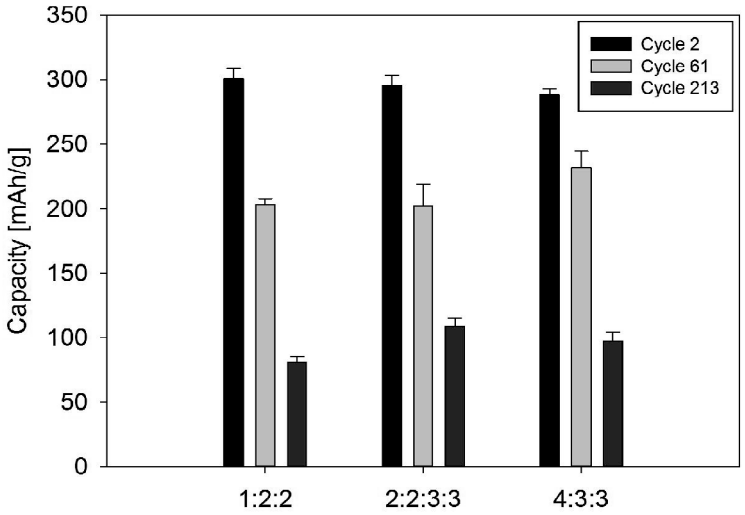

Figure 5.5. Cycle capacity at C/8 for different electrolytes (1:2:2 EC:DMC:EMC + 0.9 M $LiPF_6$, 2:2:3:3 EC:PC:DMC:EMC + 0.9 M $LiPF_6$, 4:3:3 EC:DMC:EMC + 0.9 M $LiPF_6$) with graphite SLP30/Lithium half-cells at room temperature.

The de-lithiation capacities at different temperatures for all the investigated electrolytes are plotted in Fig. 5.6. The red line and the right y-axis show the temperature at which the cells were cycled. The best 0 ^{o}C capacities are found with 4:3:3 EC:DMC:EMC + 0.9 M $LiPF_6$ (172 mAh/g) and 1:2:2 EC:DMC:EMC + 0.9 M $LiPF_6$ (169 mAh/g) as electrolyte (Fig. 5.6a) and e), respectively). The other electrolytes, 2:2:3:3 EC:PC:DMC:EMC + 0.9 M $LiPF_6$, 1:1:3 EC:EA:EMC + 0.9 M $LiPF_6$, 1:1:3 EC:PC:EMC + 0.9 M $LiPF_6$ and 1:1 EC:DEC + 1 % VC + 0.9 M $LiPF_6$ (Fig. 5.6 b), c), d) and f), respectively) all exhibited similar, but lower capacities at 0 ^{o}C (99-116 mAh/g). Notably, the electrolyte containing the ester co-solvent (1:1:3 EC:EA:EMC + 0.9 M $LiPF_6$) in Fig 5.6 d), fails after cycling at 40 ^{o}C.

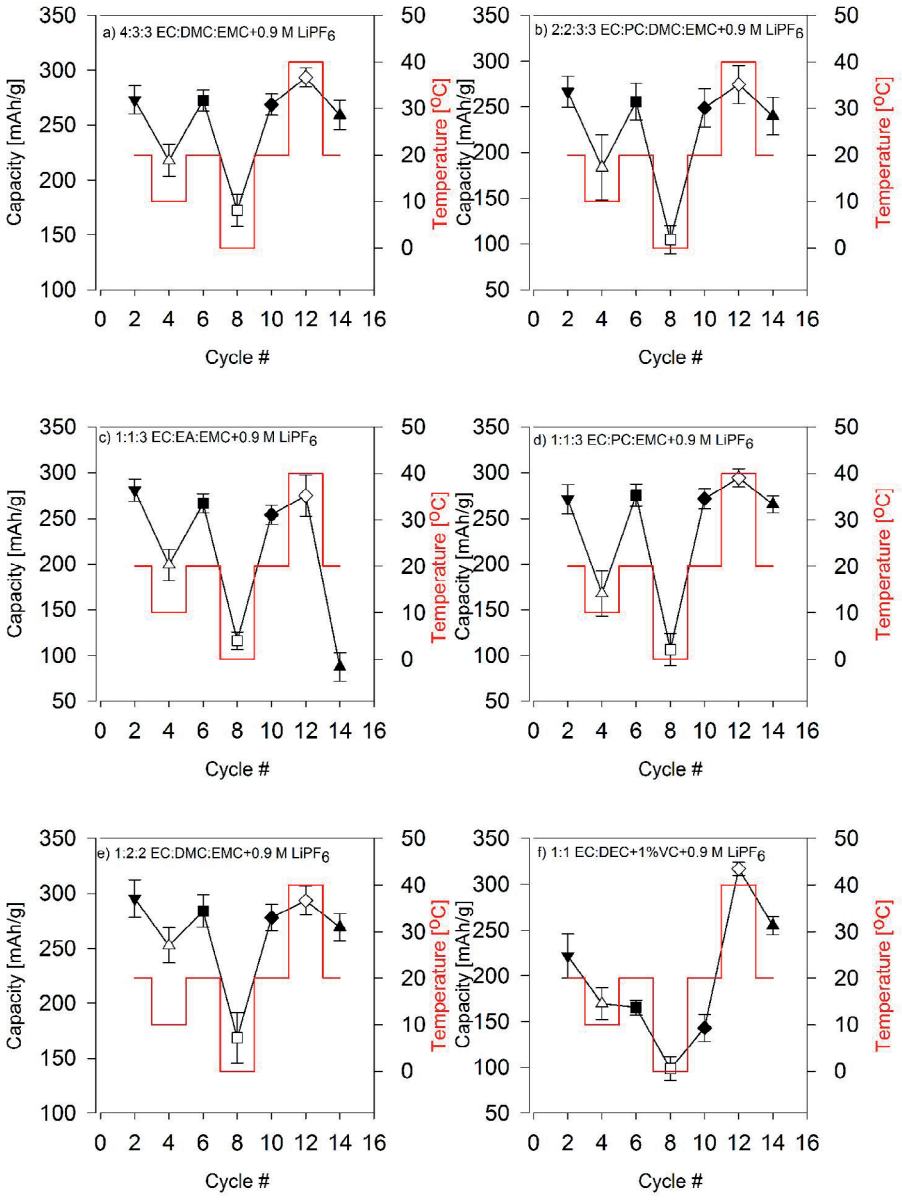

Figure 5.6. Graphite SLP30/lithium half-cells cycled at C/8 for different electrolytes at various temperatures. a) 4:3:3 EC:DMC:EMC + 0.9 M $LiPF_6$ b) 2:2:3:3 EC:PC:DMC:EMC + 0.9 M $LiPF_6$ c) 1:1:3 EC:EA:EMC + 0.9 M $LiPF_6$ d) 1:1:3 EC:PC:EMC + 0.9 M $LiPF_6$ e) 1:2:2 EC:DMC:EMC + 0.9 M $LiPF_6$ f) 1:1 EC:DEC + 1 % VC + 0.9 M $LiPF_6$.

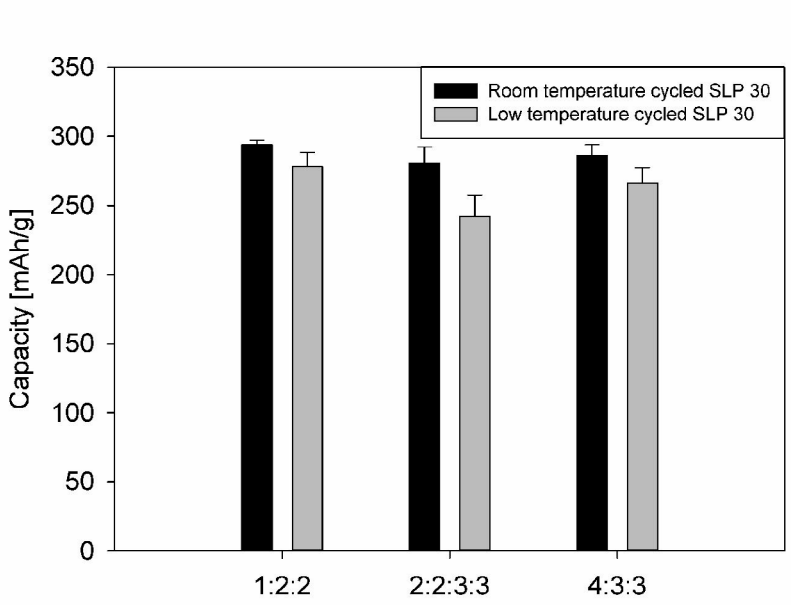

Figure 5.7. Capacity (at C/37.2) remaining after 17 cycles. Comparison of room temperature cycled (black) graphite SLP30 and low temperature cycled (grey) graphite SLP30. The capacity data are obtained at 20 ^{o}C after cycling with different electrolytes (1:2:2 EC:DMC:EMC + 0.9 M $LiPF_6$, 2:2:3:3 EC:PC:DMC:EMC + 0.9 M $LiPF_6$, 4:3:3 EC:DMC:EMC + 0.9 M $LiPF_6$).

Fig. 5.7 compares graphite SLP30 cycled at room temperature with those exposed to low temperature cycling in Fig. 5.6. The capacities are compared after 17 cycles. The figure indicates a higher degradation for the cells exposed to temperature cycles compared to cells cycled at room temperature.

Fig. 5.8 compares differential capacity plots for 1:2:2 EC:DMC:EMC + 0.9 M $LiPF_6$ electrolyte, before and after temperature cycling, to investigate if there are any changes in the peak positions (which would indicate a change of polarization) after being subjected to temperature cycling . No significant difference is observed.

Fig. 5.9 compares the differential capacity plots for 1:2:2 EC:DMC:EMC + 0.9 M $LiPF_6$ at different temperatures. For 20 ^{o}C there are peaks, indicative of stage formation in graphite, observed around 0.2, 0.1 and 0.05 V. According to Fig. 5.9 these all shift with temperature. To investigate how large these shifts can be from 20 ^{o}C to 0 ^{o}C, Fig. 5.10 shows a magnified view of the first intercalation potential. The shift is here observed to be about 0.0284 V from 20 to 0 ^{o}C.

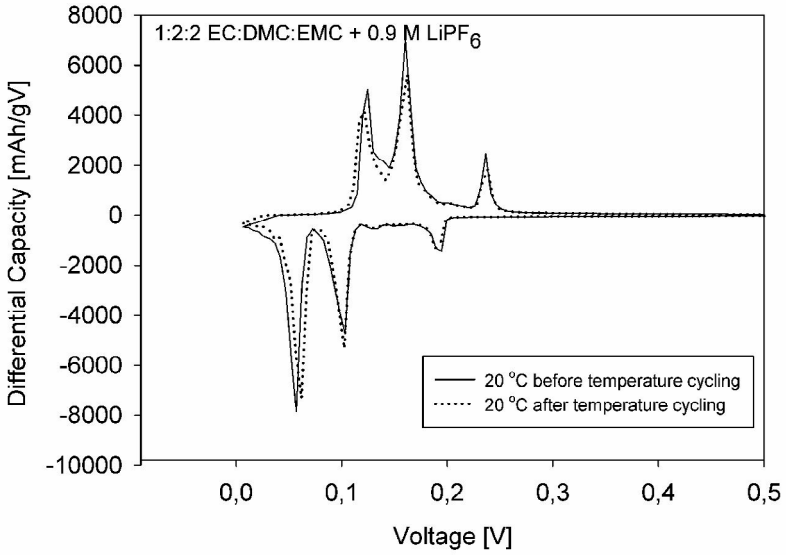

Figure 5.8. Differential capacity curves of graphite SLP30/lithium half-cell cycled at C/8 at 20 °C , before and after temperature cycles (cycle # 2 and 14 in Fig. 5.6e), in 1:2:2 EC:DMC:EMC in 0.9 M $LiPF_6$.

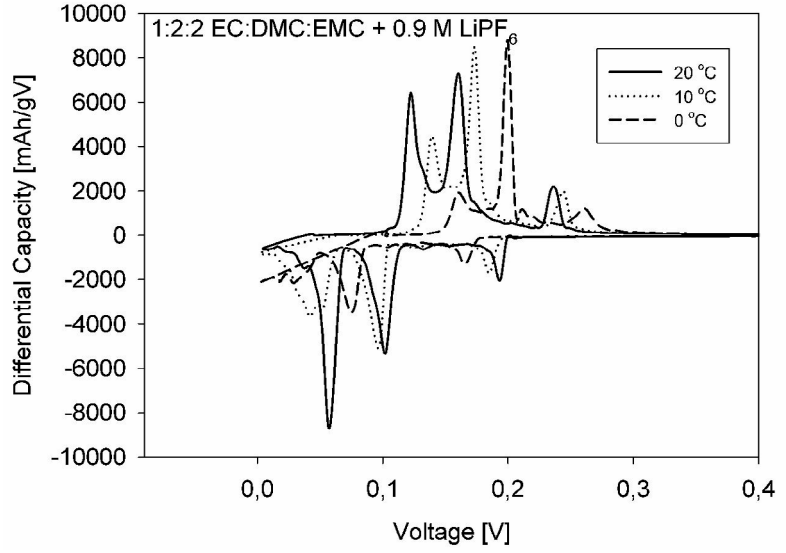

Figure 5.9. Differential capacity curves of graphite SLP30/lithium half-cell cycled at C/8 at 20, 10 and 0 °C in 1:2:2 EC:DMC:EMC in 0.9 M $LiPF_6$ (Cycle # 2, 4 and 8 in Fig. 5.6e).

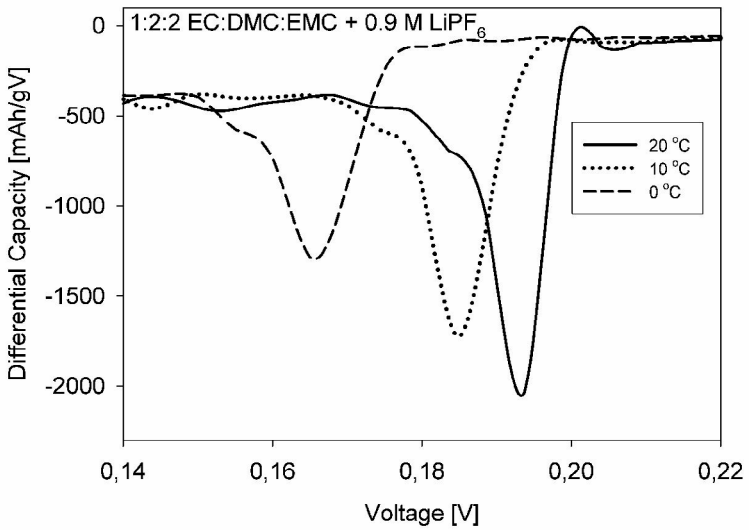

Figure 5.10. Differential capacity curves of graphite SLP30/lithium half-cell cycled at C/8 at 20, 10 and 0 °C in 1:2:2 EC:DMC:EMC in 0.9 M $LiPF_6$ (Cycle # 2, 4 and 8 in Fig. 5.6e), showing a magnified view of the first intercalation potential.

In Fig. 5.11 the EIS at different temperature in 1:2:2 EC:DMC:EMC in 0.9 M $LiPF_6$ electrolyte is plotted, which is the basis for the conductivity values in Fig. 5.12. Here the conductivity of 1:2:2 EC:DMC:EMC in 0.9 M $LiPF_6$ are calculated from high frequency intercept of EIS (Fig. 5.11) with the general formula, $\kappa = L/(R_e A)$, where κ is conductivity, L is the thickness of the electrode (including separator if added), R_e is the high frequency intercept related to the electrolyte resistance, and A is the surface area of the electrode. Notably, the values in Fig. 5.12 are one order of magnitude lower than reported bulk values for similar electrolyte systems [20].

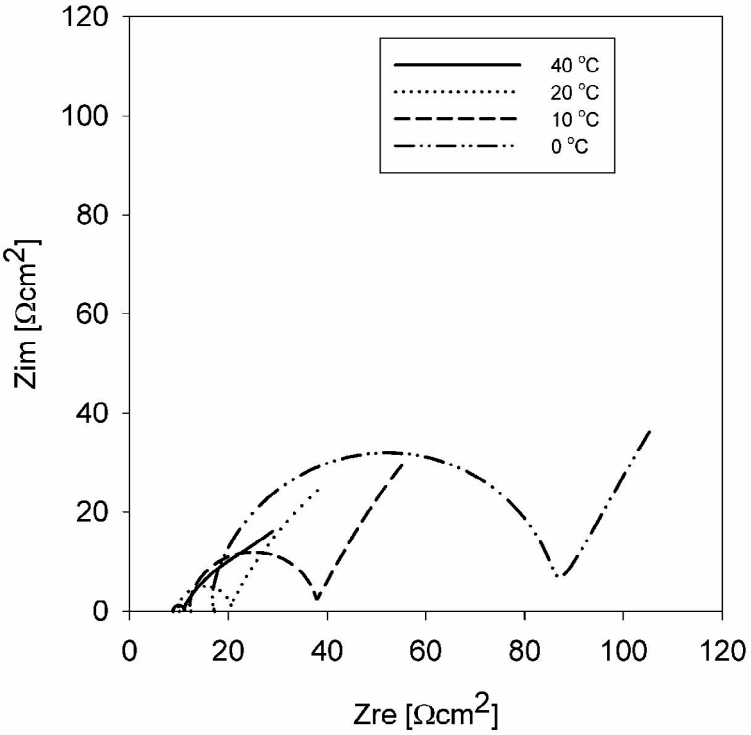

Figure 5.11. EIS of graphite SLP30/lithium half-cell cycled in 1:2:2 EC:DMC:EMC in 0.9 M $LiPF_6$ at 40, 20, 10 and 0 ^{o}C.

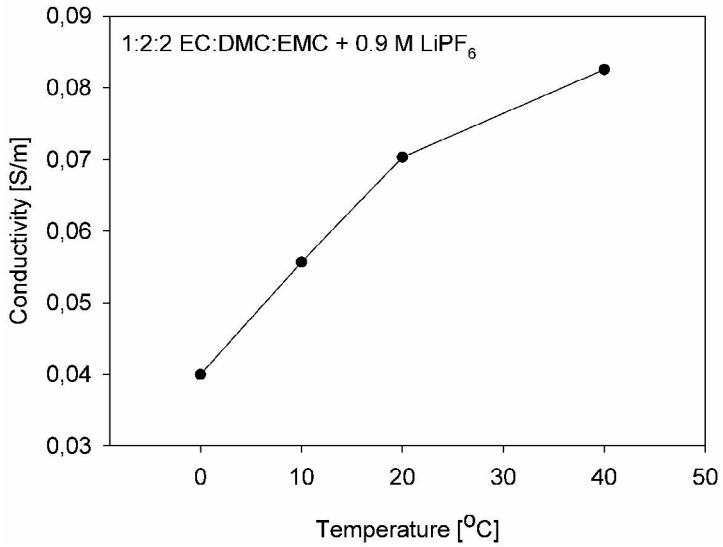

Figure 5.12. Conductivity measurements from EIS of graphite SLP30/lithium half-cell cycled in 1:2:2 EC:DMC:EMC in 0.9 M $LiPF_6$. Estimated from the high frequency intercept, which in addition to electrolyte resistance, includes the resistance across the separator and current collector.

Fig. 5.13 shows the differential capacity from Fig. 6f at 20, 10 and 0 ^{o}C in 1:1 EC:DEC 0.9 M $LiPF_6$ +1 % VC (Cycle # 2, 4 and 8 in Fig 5.6f). This electrolyte exhibited irreversible behavior after being cycled at lower temperatures, therefore it warranted further investigation by differential capacity plots. We observe a shift in intercalation potentials with decreasing temperature. The final stage formation (occurring around 0.05 V for 20 ^{o}C) disappears with decreasing temperature.

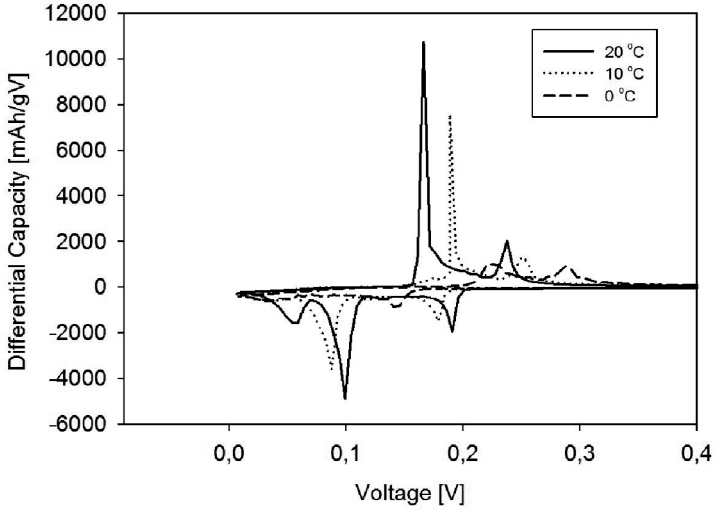

Figure 5.13. Differential capacity plots of graphite SLP30/lithium half-cell cycled at C/8 at 20, 10 and 0 °C in 1:1 EC:DEC 0.9 M $LiPF_6$ +1 % VC (Cycle # 2, 4 and 8 in Fig. 5f).

Fig. 5.14 shows the differential capacity from Fig. 5.6f at 20 °C after 10 °C, and 20 °C after 40 °C in 1:1 EC:DEC 0.9 M $LiPF_6$ +1 % VC (Cycle # 6 and 14 in Fig 5.6f). Most notably is the reappearance of the peak at the final intercalation potential after cycling at 40 °C, which disappeared with decreasing temperature (Fig. 5.13).

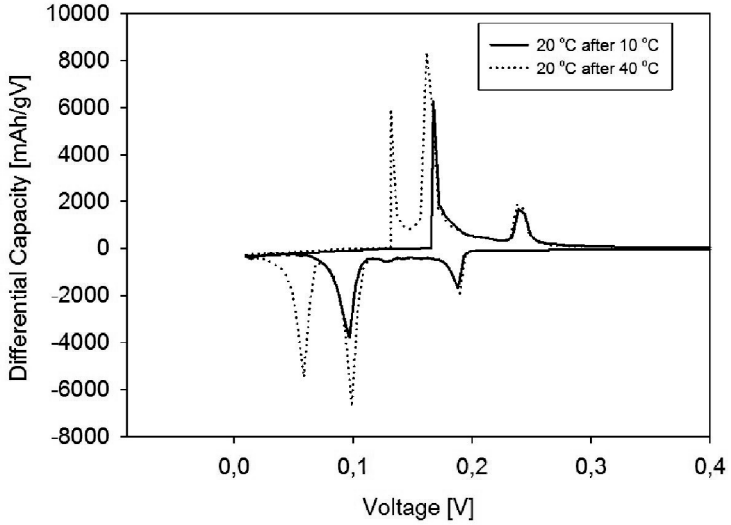

Figure 5.14. Differential capacity plot of graphite SLP30/lithium half-cell cycled at C/8 at 20 °C after cycling at 10 °C, and at 20 °C after cycling at 40 °C in 1:1 EC:DEC 0.9 M $LiPF_6$ +1 % VC (Cycle # 6 and 14 in Fig 5.6f).

5.5 Discussion

Addition of PC and effect of % EC

From Table 5.2 it is apparent that the electrolytes containing PC exhibit a higher initial capacity loss compared to the electrolytes without PC. This is expected, and normally attributed to exfoliation during the initial charge due to lithium species solvated by PC, co-intercalating into the graphite structure before a protective SEI is formed by solvent reduction. However, after a protective SEI is formed, the capacity start to stabilize (as seen in Table 5.3, which shows extended cycling of 2:2:3:3 EC:PC:DMC:EMC + 0.9 M $LiPF_6$, 1:2:2 EC:DMC:EMC + 0.9 M $LiPF_6$ and 4:3:3 EC:DMC:EMC + 0.9 M $LiPF_6$ at room temperature, and Fig. 5.4) and the electrolytes with PC (containing 40 % cyclic carbonates) show comparable stability with the electrolyte with only 20 % cyclic carbonates (1:2:2 EC:DMC:EMC + 0.9 M $LiPF_6$). The electrolyte with 40 % EC (4:3:3 EC:DMC:EMC + 0.9 M $LiPF_6$) showed highest stability. Notably, at higher C-rates (see Fig. 5.5) the electrolytes perform more or less the same.

The reason for the improved stability of the electrolytes with 40 % cyclic carbonates could be related to the initial formation of the SEI and the amount of cyclic species in the electrolyte (assuming the amount is sufficient to fully solvate the lithium ions). Since both EC and PC have a greater affinity towards solvation of lithium compared to the linear carbonates (DEC, DMC and EMC), lithium ions will prefer the cyclic carbonates as long as the amount of cyclic carbonates is sufficient to ensure complete solvation. Recent studies on the solvation sheath have shown how the ratio and amount of cyclic/linear carbonates could have an impact on which species are preferentially reduced to form the SEI [9, 10]. Specifically, they saw an increase in activation energy when the amount of EC was sufficient to fully solvate the lithium ions, which in this case occurred at about 30 % EC. The higher activation energy required with increased EC content explains why the electrolyte with more EC performed worse at higher C-rate (Fig. 5.5).

Thermal behavior

A very thorough study on liquid-solid phase diagrams of organic carbonates was performed by Ding *et al.* [7, 24, 25] and from the ternary diagram of the EC/DMC/EMC systems it is expected that, for the 4:3:3 EC:DMC:EMC electrolyte, the EC component may start to precipitate when cycled at 0 ^{o}C (due to high EC content). These studies were performed without the addition of electrolyte salt, but our results with low temperature DSC of 4:3:3 EC:DMC:EMC + 0.9 M $LiPF_6$ electrolyte (Fig. 5.2a), indicates that this electrolyte remains a liquid until -10 ^{o}C. In general, the low temperature DSC (Fig. 5.2a), show that most of the electrolytes remain in the liquid state until around -30 ^{o}C and below. The exception is the 4:3:3 EC:DMC:EMC + 0.9 M $LiPF_6$ electrolyte, which stays liquid until -10 ^{o}C and 1:1 EC:DEC +1 % VC + 0.9 M $LiPF_6$ (Fig. 5.2b), which starts to solidify already at 10 ^{o}C. The replacement of 20 % EC with PC in this electrolyte decreased the solidus temperature to below -40 ^{o}C (as seen by 2:2:3:3 EC:PC:DMC:EMC + 0.9 M $LiPF_6$ electrolyte in Fig. 5.2a).

In the high temperature DSC (Fig. 5.3a), obtained with cycled and fully lithiated graphite electrodes, we observe that the 1:1:3 EC:EA:EMC + 0.9 M $LiPF_6$ electrolyte shows the earliest onset temperature for exothermic reaction, at around 80 ^oC, followed by 1:1 EC:DEC +1 % VC + 0.9 M $LiPF_6$ at around 90 ^oC. For the remaining four electrolytes the first exothermic reaction peaks appear around 120 ^oC. The electrolyte with EA fails after cycling at 40 ^oC (Fig. 5.6c), which fits well with the early onset temperature observed in the DSC data. If the internal resistance and current is sufficiently high the local temperature within the cell could reach the temperature at which this electrolyte exhibits exothermic behavior. This electrolyte would thus not be suitable for practical battery applications.

Low temperature effects
From the de-lithiation capacities at the different temperatures in Fig. 5.6, 1:2:2 EC:DMC:EMC 0.9 M $LiPF_6$ and 4:3:3 EC:DMC:EMC + 0.9 M $LiPF_6$ show the highest performance in terms of capacity of all the tested electrolytes after being subjected to low temperature cycling. Even though 1:2:2 EC:DMC:EMC 0.9 M and 4:3:3 EC:DMC:EMC + 0.9 M $LiPF_6$ display the best capacity according to Fig. 5.6, it is important to recall that 4:3:3 EC:DMC:EMC + 0.9 M $LiPF_6$ also exhibits the best capacity upon extended cycling at room temperature, according to Table 5.3 and Fig. 5.4.

Fig. 5.7 compares graphite SLP30 cycled at room temperature with those exposed to low temperature cycling (Fig. 5.6). This data suggest that there is indeed a detrimental effect from cycling at low temperature compared to room temperature. There is nothing to suggest that the amount of EC cause any additional losses compared to the other electrolytes. The higher capacity loss of the low temperature cycled cells seems to be more or less independent of the electrolyte (at least the ones tested here). That would indicate that either there is; less active area available, a change in the SEI occurring in all the electrolytes responsible for decreased capacity, or perhaps the transport properties are decreased (electrolyte conductivity, charge transfer). Decreased active area could be either due to exfoliation or blocking of pathways due to deposition of solid lithium in the solid electrolyte from the increased electronic conductivity of the solid electrolyte, which has been reported to occur at elevated temperatures [1]. If there was any decrease in transport properties one would expect a polarization of the electrode potential consistent with a shift in the differential capacity curves, which we did not observe (Fig. 5.8). Any changes in the SEI are difficult to investigate but at least the thermal properties of room temperature cycled graphite and low temperature cycled graphite seem to be more or less unchanged (Fig. 5.3b).
There is also an increased probability of lithium plating at lower temperature which would affect the capacity either by facilitating SEI formation or pressure build-up due to electrolyte decomposition. The latter would cause exfoliation and explains the increased capacity loss from the low temperature cycled cells.

Conductivity measurements (Fig. 5.12) obtained by EIS in electrolyte 1:2:2 EC:DMC:EMC in 0.9 M $LiPF_6$, was, as previously mentioned, one order of magnitude lower than reported bulk values for similar electrolyte systems [20]. However, the changes in conductivity with temperature ($\Delta\kappa$) are somewhat similar: And if one takes

into account the effective conductivity, which is given by $\kappa_{eff} = \kappa\varepsilon/\tau$, where ε is the porosity and τ is the tortuosity (choosing a porosity of 0.4 and a tortuosity of 3) the values for conductivity are very close to the ones obtained from EIS. Tortuosity values of 3 are quite high, but similar values have been observed in lithium battery composite electrodes [26]. Conductivity measurements are taken from the high frequency intercept, which in our system can include both the resistance from the current collector (and wires) and the resistance across the separator, although contributions from wires and current collector are generally quite low, the contribution from the separator cannot be ignored. In our study a 20 μm thick separator was used with porosity close to 40 %, which is about the same as the porosity of the graphite electrode. Therefore a porosity factor of 0.4 is reasonable, and due to the geometry of the graphite, with the possibility of different sizes and shapes creating a complex transport route for lithium, a tortuosity factor of 3 is also within reason.

The estimated potential shift based on the conductivity measurements alone (Fig. 5.12) are in the order of 0.002 V. The actual potential shift (Fig. 5.10) from 20 to 0 ^{o}C, which is estimated to around 0.0284 V, could thus not be explained merely by changes in conductivity and its variation with temperature, since it is over one order of magnitude lower than the observed shift. Certainly, one must consider other contributing factors as well, such as charge transfer, de-solvation energy and lithium transport through the SEI.

Binary electrolyte effects

From the DSC data in Fig. 5.2b there is an endothermic peak, around 10 ^{o}C, indicating a phase transition from liquid to solid phase. The 1:1 EC:DEC + 0.9 M $LiPF_6$ + 1 % VC electrolyte has the highest onset temperature for solidification starting around 10 ^{o}C, which could explain the poor capacity exhibited by this electrolyte at 0 ^{o}C (Fig. 5.6f), but not the fact that the capacity is not retained when heated back to 20 ^{o}C. By comparing the differential capacity at different temperatures (Fig. 5.13) and at 20 ^{o}C after cycling at 10 ^{o}C and 40 ^{o}C (Fig. 5.14), it is observed that the final stage intercalation (initially occurring around 0.05-0.06 V according to Fig. 5.13) disappears with decreasing temperature, only to reappear after cycling at 40 ^{o}C (Fig. 5.14). The first and second intercalation potential, as seen by peaks around 0.19 V and 0.1 V in Fig. 5.14, occur at the same potential at 20 ^{o}C (after cycling at 10 ^{o}C and 40 ^{o}C, respectively). Since no shift is observed, it is reasonable to believe that the disappearance of the final stage formation (around 0.05 V) has nothing to do with decreased kinetics or conductivity, as one would expect to see a shift in all the peaks if this were the case (as with decreasing temperature in Fig. 5.9).

These results suggest that something is happening during low temperature cycling that inhibits the final stage formation, which requires a certain activation energy to regain its initial capacity, exemplified in this case by cycles at 40 ^{o}C. This behavior could be explained by the DEC component taking a more active role in the solvation sheath around the lithium ions when part of the EC component becomes solidified. Cycling in pure DEC has shown lack of sufficient SEI film formation, and no typical intercalation peaks are observed [27]. Cycling in pure DEC does therefore not intercalate lithium without the use of co-solvents [28, 29]. This has been explained by the fact the solubility makes the DEC reduction unable to form a proper SEI [30]. Only after a sufficient amount of energy is supplied will the solidified EC component become a

liquid again and take part in the solvation and de-solvation process, restoring the capacity. Another possibility would be that when the EC component is solidified, it either traps some lithium on the surface or it might block some active sites, rendering certain areas unavailable for intercalation until the EC component becomes liquefied again (at around 40 ^{o}C). If lithium ions are trapped during this solidification, a slight shift in intercalation steps 3 and 2 would be expected due to decreased conductivity. However it is a possibility that this shift is too small to be observed, or that the ratio of EC to linear carbonates is such that the loss of conductivity from presumed lithium trapping is compensated for by a higher ratio of linear carbonates, reducing the viscosity of the solution, and thus making it easier for the remaining lithium ions to move through the solution. This behavior is not observed for the other electrolytes (Fig. 5.6a-e).

5.6 Conclusion

The charge/discharge curves at the different temperatures and the long term cycling indicates that by replacing 20 % EC with PC, making the total amount of cyclic carbonates 40 %, the initial capacity loss would increase due to exfoliation, but the long term stability would be comparable to an electrolyte with only 20 % EC. Addition of PC increased the liquid range of the electrolyte, effectively increasing the low temperature operating range.

The amount of EC compared to total surface area is very important for the stability of the graphite surface, and a larger amount of EC did indeed lead to increased long term stability for slow cycling. However, this was not the case at higher C-rates due to the increased de-solvation energy of electrolytes with large amounts of cyclic carbonates.
The polarization observed when cycling at different temperatures, which is one of the main reasons of the capacity loss, could not be explained by loss of conductivity with temperature alone. Other effects, such as charge transfer resistance, lithium transport properties through the SEI and increased de-solvation energy are most likely all contributing, and the total increase of the electrode resistance, as obtained from impedance spectroscopy, was found to agree well with the observed shifts in the peaks of the differential capacity curves. The relative contributions of these processes could however not be determined from the impedance spectra, as this exhibited only one large, depressed semi-circle.

It was also concluded that low temperature cycling caused more degradation compared to room temperature cycling, but showed no signs of affecting the thermal stability. The capacity loss is most likely related to the increased probability of lithium plating. This can cause losses either by facilitating SEI formation or by electrolyte decomposition, followed by a pressure build-up and exfoliation.

The electrolyte with EA experiences cell failure due to extended cycling or cycling at elevated temperatures. The binary electrolyte with EC:DEC exhibited a capacity loss at 10 ^{o}C which is only retrievable after supplying an activation energy in the form of cycling at elevated temperatures (40^{o}C). This was believed to be due to solidification of EC, and corresponding increase in de-solvation energy or blocking of active surface area, rendering certain areas of graphite unavailable, until it was liquefied again.

Acknowledgments

The Norwegian Research Council (grant number 195432/S10), SINTEF, and NTNU. The industrial partners, Elkem Carbon AS, Miljøbil Grenland AS and Carbontech Holding AS are acknowledged for their co-funding of the project.

References

1. E. Peled, *The Electrochemical-Behaviour of Alkali and Alkaline-Earth Metals in Non-Aqueous Battery Systems - The Solid Electrolyte Interphase Model.* Journal of the Electrochemical Society, 1979. **126**(12): p. 2047-2051.
2. G. Park, et al., *The study of electrochemical properties and lithium deposition of graphite at low temperature.* Journal of power sources. **199**(0): p. 293-299.
3. C.-K. Huang, et al., *The Limits of Low-Temperature Performance of Li-Ion Cells.* Journal of the Electrochemical Society, 2000. **147**(8): p. 2893-2896.
4. D. Aurbach, et al., *New insights into the interactions between electrode materials and electrolyte solutions for advanced nonaqueous batteries.* Journal of power sources, 1999. **81**: p. 95-111.
5. S.S. Zhang, K. Xu, and T.R. Jow, *Optimization of the forming conditions of the solid-state interface in the Li-ion batteries.* Journal of power sources, 2004. **130**(1-2): p. 281-285.
6. S.S. Zhang, et al., *Effect of propylene carbonate on the low temperature performance of Li-ion cells.* Journal of power sources, 2002. **110**(1): p. 216-221.
7. M.S. Ding, et al., *Liquid/solid phase diagrams of binary carbonates for lithium batteries part II.* Journal of the Electrochemical Society, 2001. **148**(4): p. A299-A304.
8. M.C. Smart and B.V. Ratnakumar, *Effects of Electrolyte Composition on Lithium Plating in Lithium-Ion Cells.* Journal of the Electrochemical Society, 2011. **158**(4): p. A379-A389.
9. K. Xu, et al., *Solvation Sheath of Li+ in Nonaqueous Electrolytes and Its Implication of Graphite/Electrolyte Interface Chemistry.* The Journal of Physical Chemistry C, 2007. **111**(20): p. 7411-7421.
10. K. Xu, *"Charge-Transfer" Process at Graphite/Electrolyte Interface and the Solvation Sheath Structure of Li+ in Nonaqueous Electrolytes.* Journal of the Electrochemical Society, 2007. **154**(3): p. A162-A167.
11. T. Abe, et al., *Lithium Ion Transfer at the Interface between Lithium-Ion-Conductive Solid Crystalline Electrolyte and Polymer Electrolyte.* Journal of the Electrochemical Society, 2004. **151**(11): p. A1950-A1953.
12. T. Abe, et al., *Solvated Li-Ion Transfer at Interface Between Graphite and Electrolyte.* Journal of the Electrochemical Society, 2004. **151**(8): p. A1120-A1123.
13. K. Xu, A. von Cresce, and U. Lee, *Differentiating Contributions to "Ion Transfer" Barrier from Interphasial Resistance and Li+ Desolvation at Electrolyte/Graphite Interface.* Langmuir. **26**(13): p. 11538-11543.
14. M.C. Smart, et al., *Lithium-Ion Electrolytes Containing Ester Cosolvents for Improved Low Temperature Performance.* Journal of the Electrochemical Society, 2010. **157**(12): p. A1361-A1374.
15. M.C. Smart, et al., *Improved low-temperature performance of lithium-ion cells with quaternary carbonate-based electrolytes.* Journal of power sources, 2003. **119**: p. 349-358.

16. M.C. Smart, et al., *Performance characteristics of lithium ion cells at low temperatures.* Ieee Aerospace and Electronic Systems Magazine, 2002. **17**(12): p. 16-20.
17. M.C. Smart, B.V. Ratnakumar, and S. Surampudi, *Use of Organic Esters as Cosolvents in Electrolytes for Lithium-Ion Batteries with Improved Low Temperature Performance.* Journal of the Electrochemical Society, 2002. **149**(4): p. A361-A370.
18. M.C. Smart, B.V. Ratnakumar, and S. Surampudi, *Electrolytes for low-temperature lithium batteries based on ternary mixtures of aliphatic carbonates.* Journal of the Electrochemical Society, 1999. **146**(2): p. 486-492.
19. A. Ohta, et al., *Relationship between carbonaceous materials and electrolyte in secondary lithium-ion batteries.* Journal of power sources, 1995. **54**(1): p. 6-10.
20. D. Yaakov, et al., *On the Study of Electrolyte Solutions for Li-Ion Batteries That Can Work Over a Wide Temperature Range.* Journal of the Electrochemical Society, 2010. **157**(12): p. A1383-A1391.
21. N. Gunawardhana, et al., *Suppression of lithium deposition at sub-zero temperatures on graphite by surface modification.* Electrochemistry Communications. **13**(10): p. 1116-1118.
22. B.K. Mandal, et al., *New low temperature electrolytes with thermal runaway inhibition for lithium-ion rechargeable batteries.* Journal of power sources, 2006. **162**(1): p. 690-695.
23. H. Maleki, et al., *Thermal stability studies of Li-ion cells and components.* Journal of the Electrochemical Society, 1999. **146**(9): p. 3224-3229.
24. M.S. Ding, *Liquid-Solid Phase Diagrams of Ternary and Quaternary Organic Carbonates.* Journal of the Electrochemical Society, 2004. **151**(5): p. A731-A738.
25. M.S. Ding, K. Xu, and T.R. Jow, *Liquid-Solid Phase Diagrams of Binary Carbonates for Lithium Batteries.* Journal of the Electrochemical Society, 2000. **147**(5): p. 1688-1694.
26. D. Kehrwald, et al., *Local Tortuosity Inhomogeneities in a Lithium Battery Composite Electrode.* Journal of the Electrochemical Society, 2011. **158**(12): p. A1393-A1399.
27. M.E. Spahr, et al., *Exfoliation of Graphite during Electrochemical Lithium Insertion in Ethylene Carbonate-Containing Electrolytes.* Journal of the Electrochemical Society, 2004. **151**(9): p. A1383-A1395.
28. D. Aurbach, et al., *The study of electrolyte-solutions based on ethylene and diethyl carbonates for the rechargeable Li batteries.2. Graphtie-electrodes.* Journal of the Electrochemical Society, 1995. **142**(9): p. 2882-2890.
29. Y. Ein-Eli, S.F. McDevitt, and R. Laura, *The superiority of asymmetric alkyl methyl carbonates.* Journal of the Electrochemical Society, 1998. **145**(1): p. L1-L3.
30. D. Aurbach, et al., *Identification of surface-films formed on lithium in propylene carbonate solutions.* Journal of the Electrochemical Society, 1987. **134**(7): p. 1611-1620.

6. Electrochemical impedance spectroscopy of porous graphite electrode for lithium ion batteries

6.1 Summary

Electrochemical impedance spectroscopy (EIS) has been employed to study the complex system of porous graphite anodes used in lithium ion batteries. A typical impedance response shows two semicircles, as well as a low frequency response related to intercalation, and eventually a blocking response. Many attribute the high frequency semi-circle in impedance spectra to the film formation (commonly called SEI) on the graphite and the middle frequency semi-circle to charge transfer resistance. Two semi-circles are not always observed in the graphite/electrolyte system. By appropriate selection of the graphite surface and electrolyte we were able to distinguish the two semi-circles, the results of which are reported here. The effect of temperature shows that the resistance associated with the middle frequency arc is far more temperature dependent than that of the high-frequency arc. The activation energy for the middle-frequency arc emerging from Arrhenius plots was estimated to be 67 kJ/mol, which agrees with activation energies reported for the de-solvation process. The increase of the resistances of both the high and middle frequency resistance in this study suggest that processes related to film formation and charge transfer resistance are coupled, and no clear separation of these processes can be made. Capacity fade during cycling is related to the increase of these resistances. Diffusion coefficients were extracted from the spectra.

Highlights

We have investigated the impedance response of a porous graphite electrode with the aim to investigate the relative contributions from the film and charge transfer resistance with regards to resistance increase in the cell.

Keywords; Lithium ion battery, Graphite, EIS

6.2 Introduction

Graphite is currently the most attractive choice as anode material in lithium ion batteries (LIB). The main factor influencing the performance of the graphite anode in LIB's, is the formation and properties of the so called solid electrolyte interphase (SEI) [1]. The formation of the SEI causes initial losses due to trapping of lithium species in the film, which are irreversible and normally termed irreversible capacity losses (ICL). However, this film is very important for the structural stability of graphite, as it protects against co-intercalation of solvent species, which would introduce additional stresses on the graphene sheets, and corresponding damage of the particle surface (a process often called "exfoliation"). This exposes new area to the electrolyte available for further electrolyte reduction and consequently higher irreversible capacity losses (ICL).

Electrochemical impedance spectroscopy (EIS) has often been employed in studies of the electrochemical performance of graphite electrodes, due to the possibility of resolving contributions from the various irreversible losses, like mass transport limitations, ionic and electronic resistivities, charge transfer resistance etc. The SEI film is known to grow as a function of time [2] as long as the potential is lower than the reduction potential of the electrolyte used. The resistance increase caused by the SEI is one of the main reasons why lithium battery capacity fades with time [3]. It will also have very different properties depending on initial cycling rate, electrolyte composition, temperature during cycling and surface properties of the graphite used [4], which can complicate things further.

Fig. 6.1. shows a typical impedance response from a porous graphite anode, showing that the electrode resistance may be resolved into two semi-circles. In most lithium ion battery research the high frequency (HF) arc is attributed to the SEI film and the middle frequency (MF) to the actual charge transfer occurring on the surface, following the model proposed by Aurbach [5]. The solution resistance, R_e, can be found from the intercept of the curve with the x-axis. Usually this resistance also includes the resistance from the current collector, wiring, and separator. In accordance with the model developed by Aurbach [5], the equivalent circuit in Fig. 6.2 is commonly used in the literature in the fitting of impedance measurement [6-10], where the high frequency arc is attributed to the SEI film and the middle frequency is due to charge transfer, followed by a diffusion process.

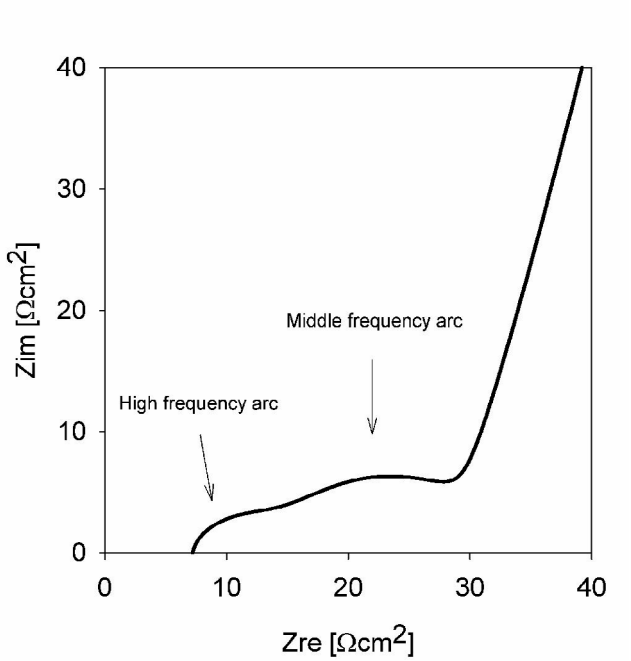

Figure 6.1. Nyquist plot of graphite G8 (from Cpreme) in 4:3:3 EC:EMC:DMC + 0.9 M $LiPF_6$ electrolyte, illustrating the high and middle frequency arcs.

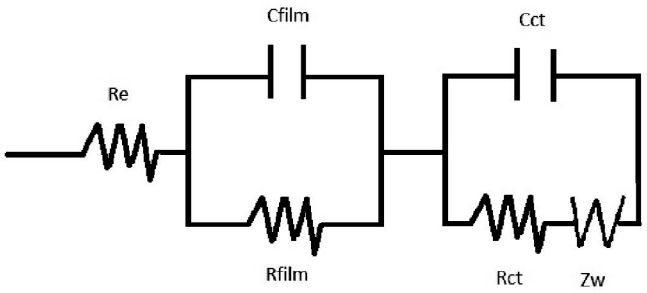

Figure 6.2. EQC most commonly used in fitting of a graphite/electrolyte interphase used in lithium ion batteries. R(RC)(C(RW)).

However it is still debated which arc should be attributed to the SEI and which one is due to charge transfer resistance. Studies of the initial charge (EIS at different potentials) showed that the HF arc was independent of potential [11, 12], which indicated that this arc had nothing to do with charge transfer. It was therefore concluded that this must be related to the surface film (SEI) [12], leaving the potential dependent middle frequency arc to charge transfer resistance. However some authors also attribute the HF arc to the electrode/current collector interface, precisely because its resistance

does not depend on potential, but rather seemed to be dependent on the geometric surface area (and not the active surface area) [9]. This was argued in a study [13], based on the fact that the HF semi-circle showed no increase during formation of the SEI, suggesting that the HF arc could be related to contact problems (graphite/electrolyte or graphite/graphite). Thus, the HF arc could not be due to the SEI, but most likely is a combination of contact problems and bulk properties [13]. The literature therefore seems much divided in its view of the HF arc as it seems far more complex than initially believed.

In addition, the interpretation of the middle frequency arc (commonly related to charge transfer resistance), is not as straight forward as previously believed. Some claim that this "charge transfer resistance" should also take into account de-solvation processes [7, 14-16] and that the de-solvation energy is actually the largest contributor to the overall activation energy at the interface [17].

The diffusion element, Zw, is also not as straight forward. The common approach is to estimate the diffusion coefficient from the low frequency region employing the traditional Warburg approach. This method is valid if the low frequency slope is close to 45 ^{o} , which is typical behavior of Warburg impedance [18], and we are in the semi-infinite region of the low frequency area. If these criteria's are met, one can estimate the diffusion coefficient according to the high frequency limit region in Meyers [19] (a model that was first derived by Ho [20] for planar films). This method requires knowledge of how the open circuit potential varies with lithium concentration, ($\partial U/\partial c_s$), a value which can be obtained from potenitiostatic curves of lithiation. Accurate estimates of ($\partial U/\partial c_s$) is also one of the major limitations with this method, as this value is very dependent on the state of charge (SOC) (which is further discussed in Chapter 7).

However, for the cases where the slope is not linear and 45^{o}, alternative methods are more commonly used. An example would be the modified EIS method [21] by which, the diffusion coefficients at 25 ^{o}C in graphite were estimated to be in the range from $1.12\cdot10^{-10}$ to $6.51\cdot10^{-11}$ cm^2/s, at 0 and 30 % SOC, respectively, assuming spherical diffusion. Other models describing porous intercalation electrodes are those by Meyers [19], Sunde [22, 23], and La. Mantia [24]. We have used MATLAB (from Mathworks) to employ a model developed by Sunde [22, 23], in our estimations. With this method you fix all known values for physical parameters such as electrode thickness and state of charge and then allow the program to minimize the complex nonlinear least squares (CNLS) object function in order fit the experimental curves and estimate the remaining unknowns. The method fits the experimental data by minimizing the object function. Similar procedures have been used by La Mantia [24], and recently by Zavalis et.al [25, 26].

We have assumed, as in previous similar studies [21], that the diffusion coefficient in the electrolyte is not significant. However, one should be aware of that models employing the modified EIS method showed a significant increase in the accuracy of the solid state diffusion with increasing solution diffusions [27]. These results explains

why previous studies [28] were only able to estimate the solid phase diffusion if it the solid phase diffusion was low enough.

In this work, impedance spectroscopy was utilised for investigation of various phenomena related to graphite electrode, including initial SEI formation, effect of temperature, as well as degradation of the electrode during deep cycles. Since the literature is diverging on the matter of the HF arc and the MF arc and their relation to charge transfer processes or film formation, one aim was to investigate this further. By evaluating the resistance of the HF and MF arcs, as a function of number of cycles, it should be possible to see a resistance increase for only one of the semicircles, which then would be related to the growth of the SEI (which is known to increase with time [2]). The charge transfer process is not expected to increase as much as a function of time. This would allow us to identify which resistance is due to the SEI and which is due to the charge transfer resistance.

However, our initial studies show that no such distinction is possible, as both resistances increased with cycling. The results indicate that the transport of lithium from the electrolyte solution, through the SEI and into the graphite is more complex than pure transport across the SEI, followed by a charge transfer. Either the SEI takes a more active role in both resistance contributions, or the charge transfer is more influenced by the SEI (i.e. by changing number of active sites), or by the de-solvation process.

6.3 Experimental

Graphite SLP30 was used as received from TIMCAL^{TM} and graphite G8 as received from Cpreme. The SLP30 and G8 graphite electrodes were prepared by tape casting a slurry consisting of 37 g SLP30 or G8, 2 g PVDF (Kynar), 1 g Super P (TIMCAL^{TM}), and 60 g 1-methyl-2-Pyrrolidinone (Aldrich) onto a 10 μm thick Cu-foil current collector from Circuit foil Luxembourg. The tape caster was a "K Control Coater" from Printcoat instruments. The casts were then dried in a vacuum oven at 120 ^{o}C overnight. The thickness of the dried casts was about 70 μm.

The electrolytes were made using varying amounts (in weight %) of ethylene carbonate (Sigma-Aldrich, > 99 %), diethyl carbonate (Aldrich, > 99 %), vinylene carbonate (VC) (Aldrich, 97 %), ethyl methyl carbonate (Merck, > 99 %), and dimethyl carbonate (Sigma-Aldrich, > 99 %) with 0.9 M $LiPF_6$ (Aldrich, > 99.99 %)

The electrochemical measurements for the impedance were performed using a three-electrode cell of the model "HS-3E test cell" by Hohsen Corp. The cells were assembled in inert atmosphere inside an argon-filled glove-box (O_2 and H_2O < 0.1 ppm) and consisted of a graphite working electrode (2.01 cm^2) with a loading of about 3 mg/cm^2, separator (Celgard® 2320), 0.75 mm thick lithium foil (1.54 cm^2) as counter electrode, and a lithium strip as a reference electrode. All potentials are reported vs. Li/Li^+ unless otherwise specified. Initial SEI formation was formed galvanostatically with a model 4200 potentiostat from Maccor. Initial current of 10 mAh/g, cycled between 5 and 1500 mV, followed by four reduction/oxidation cycles, at a constant current of 46.5 mAh/g, to ensure complete SEI formation. Electrochemical impedance was performed with Zahner IM6 potentiostat. The frequency was varied from 5-10 mHz to 1 MHz with an amplitude of 5 mV. All experiments were performed at room temperature (18-24 ^{o}C) unless otherwise specified.

6.4 Results

Fig. 6.3 shows EIS of graphite SLP30 during the first cycle in 1:1 EC:DEC + 1% VC + 0.9M $LiPF_6$ electrolyte. Fig. 6.4 shows the differential capacity for the same system during initial intercalation of lithium ions into graphite. The inset in Fig. 6.4 is a magnified view of the initial solution reduction related to the reduction of solvent species (SEI formation). This reduction occurs at 0.8 V according to the figure. Lithium intercalation proceeds in various intercalation stages [29]. These can be observed as peaks at 0.18 V, 0.08 V and 0.05 V in Fig. 6.4. The changes in the impedance response upon cycling in Fig. 6.3 can be related to reduction of electrolyte species and formation of the solid electrolyte interphase around 1000 and 500 mV.

Most notably we observe a resistance decrease upon lowering the potential. There is also a shift in the characteristic frequency upon approaching the potential where lithium intercalation begins, a behaviour previously observed in the literature [11]. This resistance decrease is more clearly observed in Fig. 6.5, showing the impdance at 1.5 V before and after SEI formation. Here it is also clear that the electrolyte resistance (high frequency intercept) seems to decrease after SEI formation.

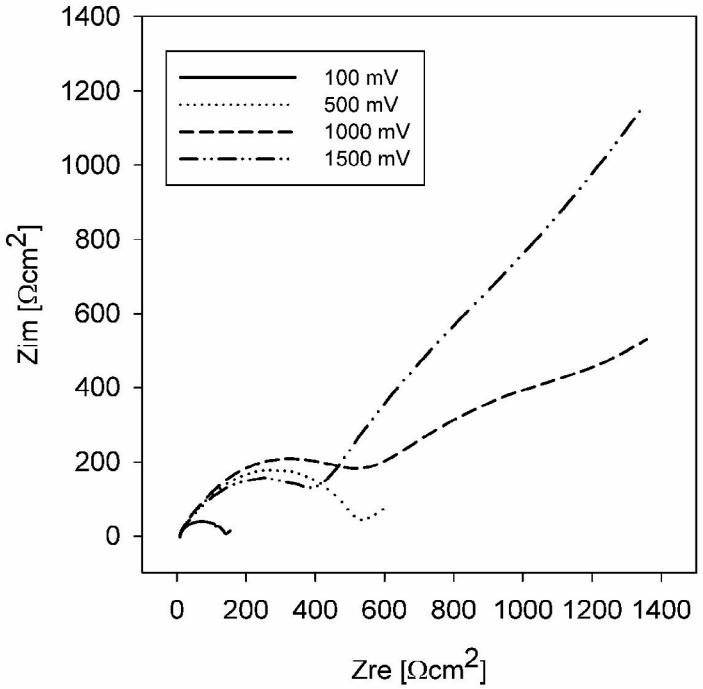

Figure 6.3. Electrochemical impedance spectroscopy of graphite SLP30 in 1:1 EC:DEC + 1% VC + 0.9M $LiPF_6$ electrolyte.

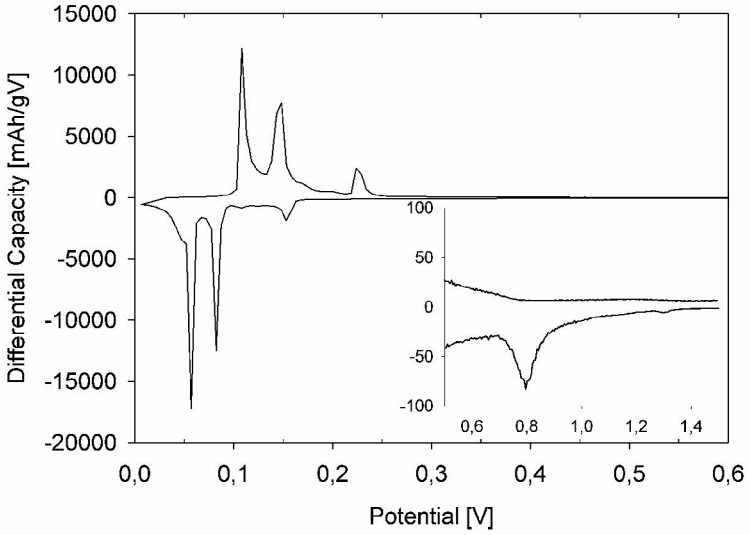

Figure 6.4. Differential capacity during the initial cycle of graphite SLP30 in 1:1 EC:DEC + 1% VC + 0.9 M $LiPF_6$ electrolyte at 10 mAh/g. The inset is a magnified view of the high potential region.

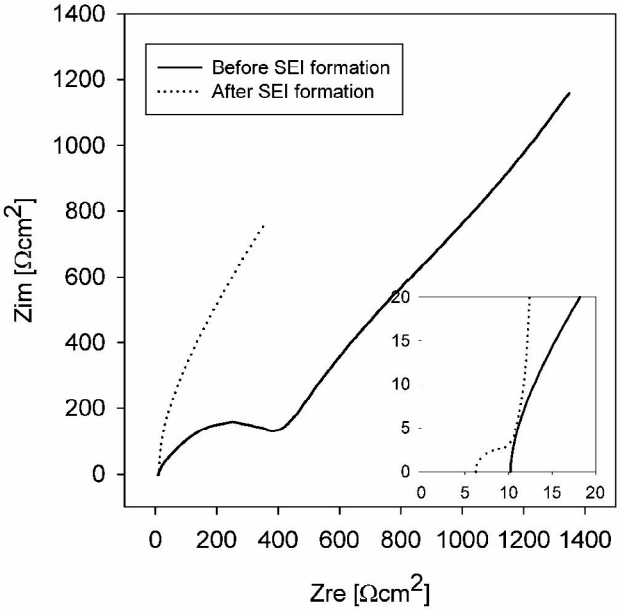

Figure 6.5. Nyquist plot at 1.5 V for graphite SLP30 in 1:1 EC:DEC + 1% VC + 0.9 M $LiPF_6$ electrolyte before and after SEI formation. The inset is a magnified view of the high frequency region.

In comparison, Fig. 6.6, shows the impedance before and after SEI formation for graphite G8. We observed the same resistance decrease here, both for the depressed semi-circle and electrolyte resistance. Notably, the inset in Fig. 6.6 shows the emergence of two semi-circles, in comparison with only the one for SLP30 (inset in Fig. 6.5).
According to the differential capacity plot of G8 in Fig. 6.7, there are no significant reactions before around 0.8 V, which is the solvent reduction. According to this figure lithium intercalation starts around 0.16 V. During the first cycle, there can be a reduction of trace O_2 around 2.0 V (forming insoluble lithium oxide), followed by trace elements of water reducing around 1.5 V (forming LiOH) , followed by salt and solvent reduction between 1.6-1.5 V and down to 0.5 V [30]. However, no significant response is observed in either Fig. 6.4 or 6.7, until around 0.7-0.8 V. The impedance response at 1500 mV, could be attributed to adsorption processes, as was successfully modelled by La Mantia [24]. But one cannot rule out the fact that solvated lithium species have already started to co-intercalate at this potential.

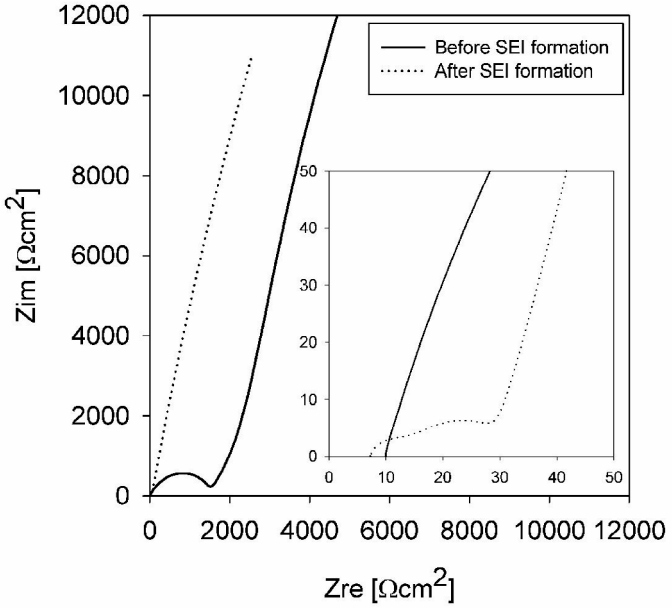

Figure 6.6. Nyquist plot at 1.5 V for graphite G8 in 4:3:3 EC:DMC:EMC + 0.9 M $LiPF_6$ electrolyte before and after SEI formation. The inset is a magnified view of the high frequency region.

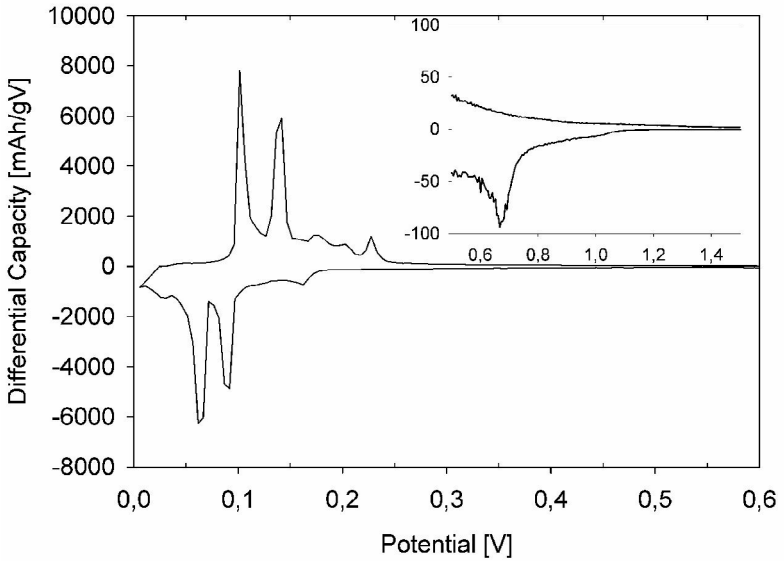

Figure 6.7. Differential capacity during the initial cycle of graphite G8 in 4:3:3 EC:DMC:EMC + 0.9 M $LiPF_6$ electrolyte at 10 mAh/g. The inset is a magnified view of the high potential region.

The two semi-circles observed with graphite G8, allows for further studies of how the HF semi-circle (usually attributed to the SEI film) and MF semi-circle of a porous graphite electrode changes with time and temperature. Notably, this separation of two circles has also been observed previously in literature of two similar electrodes with different electrolyte salt [31]. In that study this was related to different resistivity of the SEI film, (allowing for the separation of two time constants) due to differences in the properties of the SEI formed with the two salts.

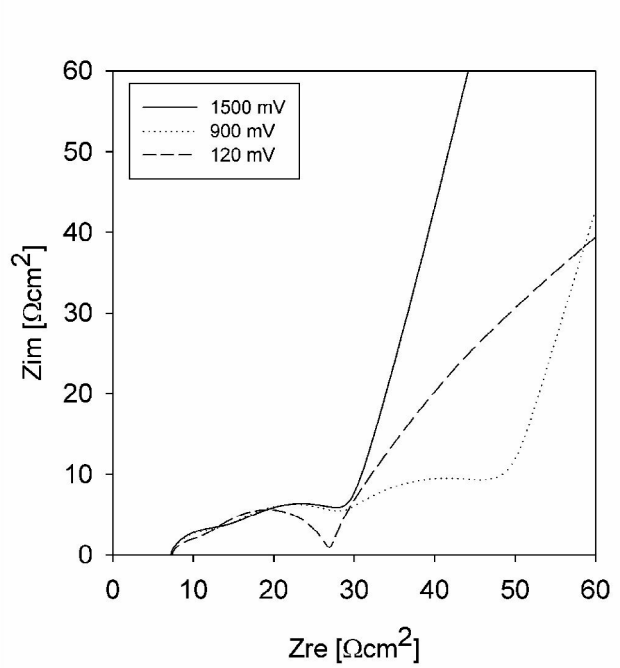

Figure 6.8. EIS of graphite G8 at various potentials in 4:3:3 EC:DMC:EMC + 0.9 M $LiPF_6$ electrolyte.

Fig. 6.8 shows the impedance response of G8 at three different potentials. We choose to fit the high and middle frequency range separate from the low frequency range, using conventional circuits, as in Fig. 6.9. This is almost the same circuit as in Fig. 6.2, except the diffusion element related to the low frequency range has been removed. ZSimpWin software (from Princeton applied research) was used in the fitting procedure.

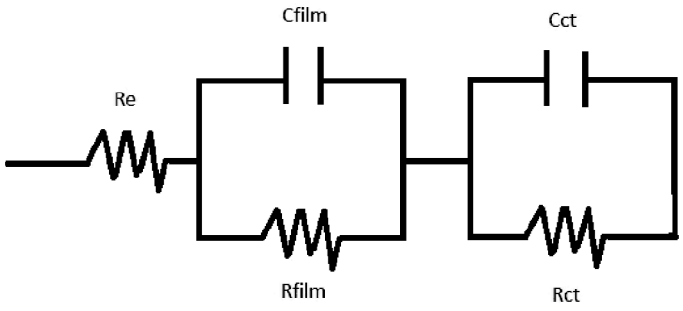

Figure 6.9. EQC emloyed in the fitting of the high and middle frequency area. R(RC)(RC).

After the fit is made it becomes possible to evaluate the respective resistances, for examples as function of number of cycles. The resistance increase, especially due to the SEI, is believed to be one of the main reasons why battery capacity fades with time. In Fig. 6.10, a typical EIS at 0.12 V of G8 is fitted with an equivalent circuit similar to Fig. 6.9. Notably, the capacitance (C) is sometimes replaced by a constant phase element (Q), to provide a better fit. The physical meaning of a constant phase element is debated [32-35], but some say that it may fit well with a system which has a distribution of time constants [35]. This description fits well with a heterogeneous graphite surface, with varying film thickness and composition. Therefore, the use of a constant phase element can be justified. The HF resistance (R_{hf}), MF resistance (R_{mf}), and the electrolyte resistance (R_e) has been plotted as a function of number of cycles in the cell in Fig. 6.11.

Fig. 6.12 shows the same EIS fit at 0.9 V. Notably, here it is possible to separate an additional semi-circle, the low frequency resistance (R_{lf}). Also here these resistances seem to increase with increasing number of cycles (Fig. 6.13)

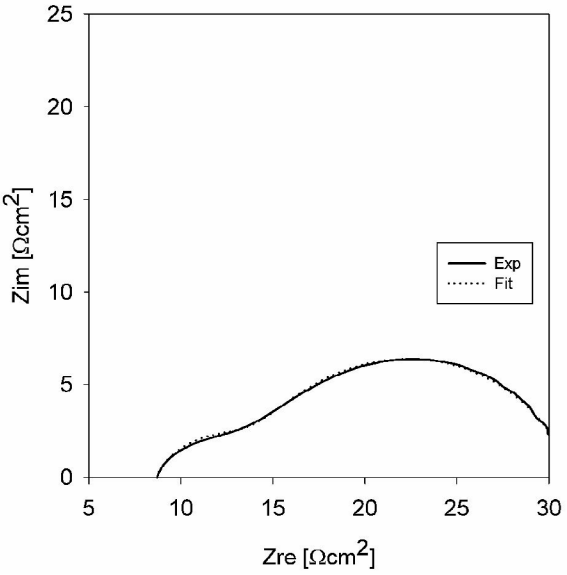

Figure 6.10. EIS graphite G8 at 0.12V in 4:3:3 EC:DMC:EMC + 0.9 M $LiPF_6$ electrolyte after initial SEI formation. Data is fitted with Zsimpwin using a R(RC)(RC) circuit element.

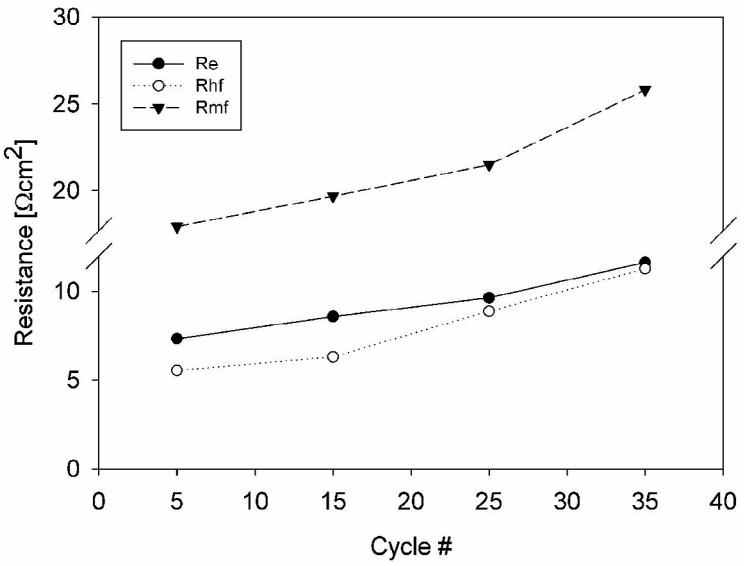

Figure 6.11. R_{hf}, R_{mf} and Re at 0.12 V of graphite G8 in 4:3:3 EC:DMC:EMC + 0.9 M $LiPF_6$ electrolyte as function of cell cycles.

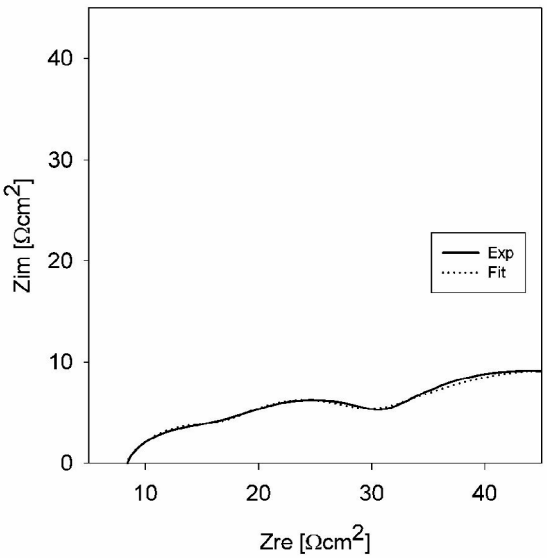

Figure 6.12. EIS graphite G8 at 0.9V in 4:3:3 EC:DMC:EMC + 0.9 M $LiPF_6$ electrolyte after intital SEI formation. Data is fitted with Zsimpwin using a R(RC)(RC)(RC) element.

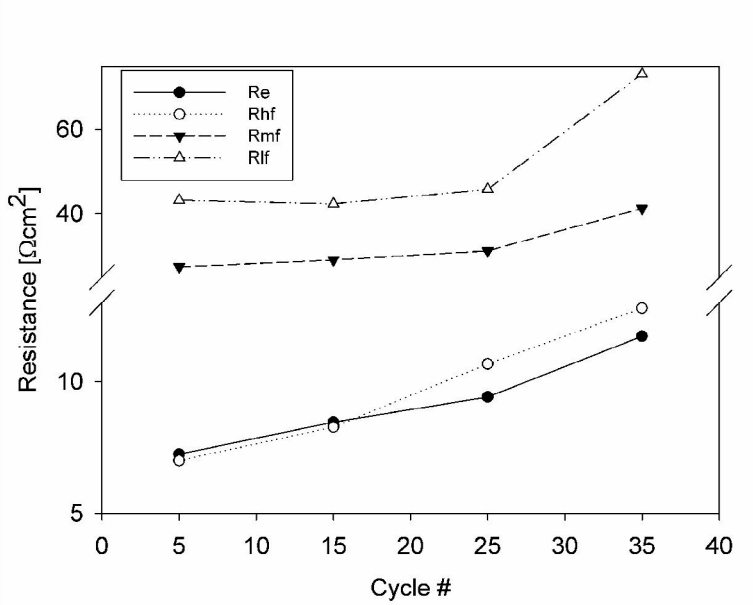

Figure 6.13. R_{hf}, R_{mf} and R_e at 0.9 V of graphite G8 in 4:3:3 EC:DMC:EMC + 0.9 M $LiPF_6$ electrolyte as function of cell cycles.

In Fig. 6.14 the impedance spectra as a function of temperature are plotted. The fitted resistances in Fig. 6.15 allows for a more clear separation of the contribution to the HF semi-circle and the MF semi-circle as a function of temperature. From this it becomes quite clear that it is the middle frequency arc (MF), which in literature is attributed to charge transfer processes, is increasing the most upon temperature decrease.

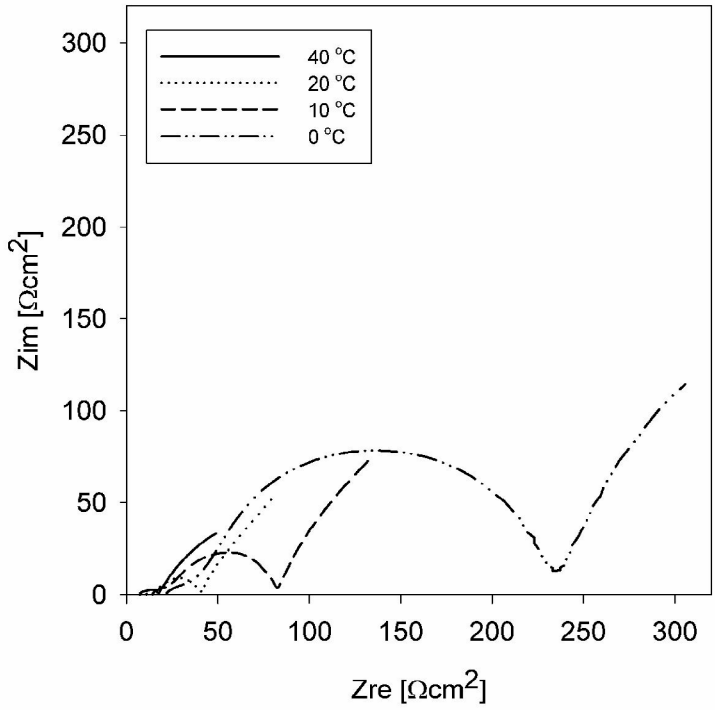

Figure 6.14. EIS response of graphite G8 in 4:3:3 EC:DMC:EMC + 0.9 M $LiPF_6$ electrolyte at 40, 20, 10, and 0 ^{o}C.

From the values in Fig. 6.15, it is possible to estimate the activation energy from the contribution of the HF and MF resistances using an Arrhenius expression following the method by Abe et.al [15, 16], as shown in Fig. 6.16. Notably, the values at 40 ^{o}C deviate from linearity, and were therefore removed to achieve a better fit. From the slopes in Fig. 6.16, an activation energy of 67.1 kJ/mol was estimated from the MF resistances and 39.1 kJ/mol from the HF resistances. The MF activation energy is similar to studies of binary electrolytes with 40 % EC content [14].

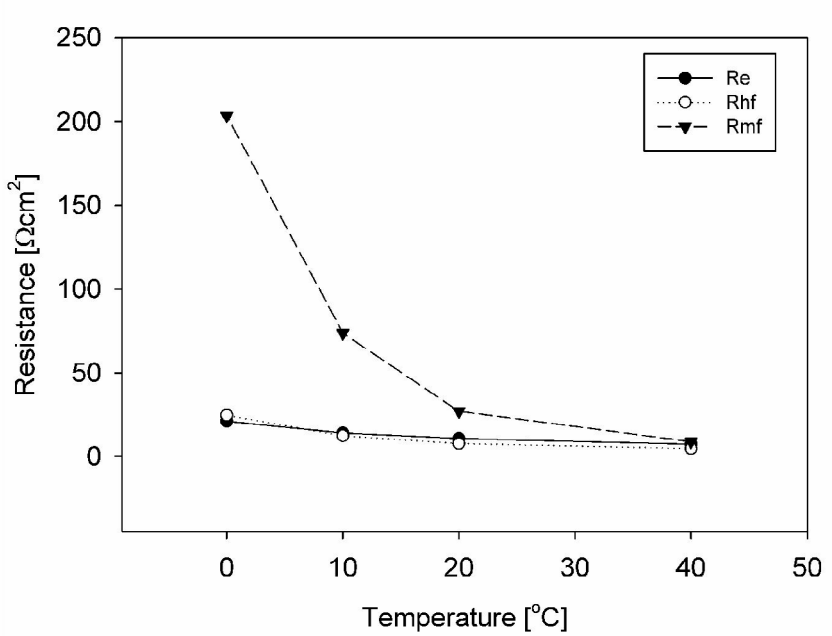

Figure 6.15. R_{hf}, R_{mf} and R_e at 0.12 V of graphite G8 in 4:3:3 EC:DMC:EMC + 0.9 M $LiPF_6$ electrolyte as function of temperature.

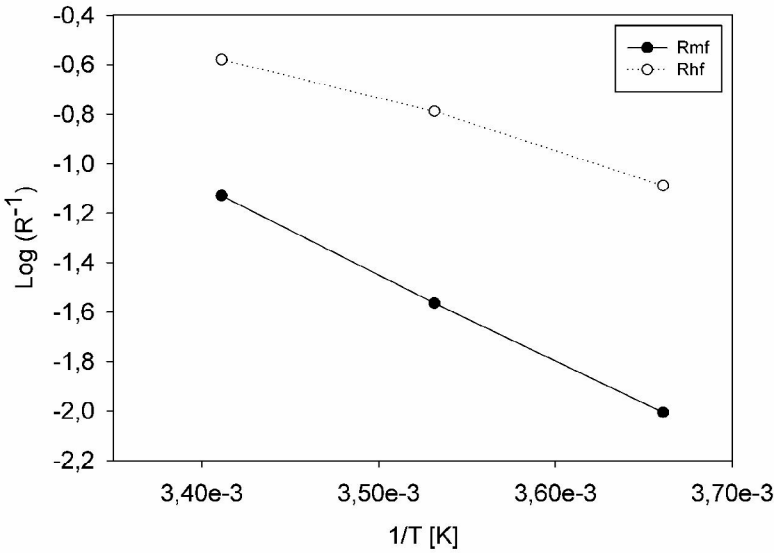

Figure 6.16. Arrhenius plot for high and middle frequency resistances.

Fig. 6.17 shows how the cell capacity varies as a function of number of cycles for the system in question. Notably, the capacity experiences an initial increase before decaying over time. The initial increase is related to SEI formation during the initial cycles.

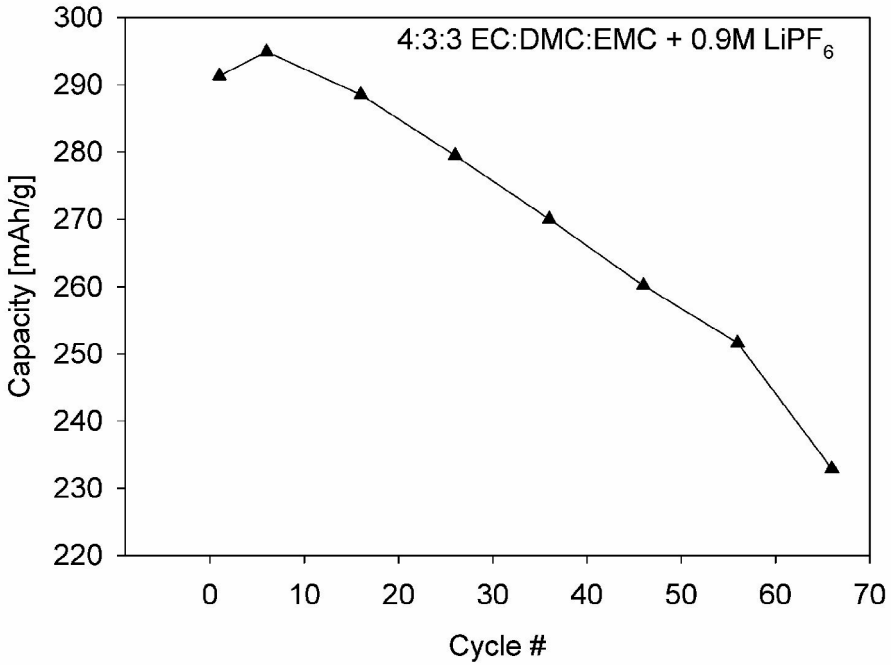

Figure 6.17. Capacity of graphite G8 in 4:3:3 EC:DMC:EMC + 0.9 M $LiPF_6$ electrolyte as function of cell cycles at 10 mAh/g.

Diffusion coefficients were estimated at 0.12 and 0.9 V using both the traditional Warburg approach from the semi-infinite region and by using the porous intercalation model, as previously discussed [19, 22, 23]. As seen in Fig. 6.18, the diffusion coefficients at 0.12 V were estimated to $8.5 \cdot 10^{-10}$ cm^2/s with Warburg and $1.5 \cdot 10^{-9}$ cm^2/s with porous intercalation model. At 0.9 V the values were estimated to $3.9 \cdot 10^{-8}$ cm^2/s (semi-infinite) and $1.4 \cdot 10^{-8}$ cm^2/s (porous).

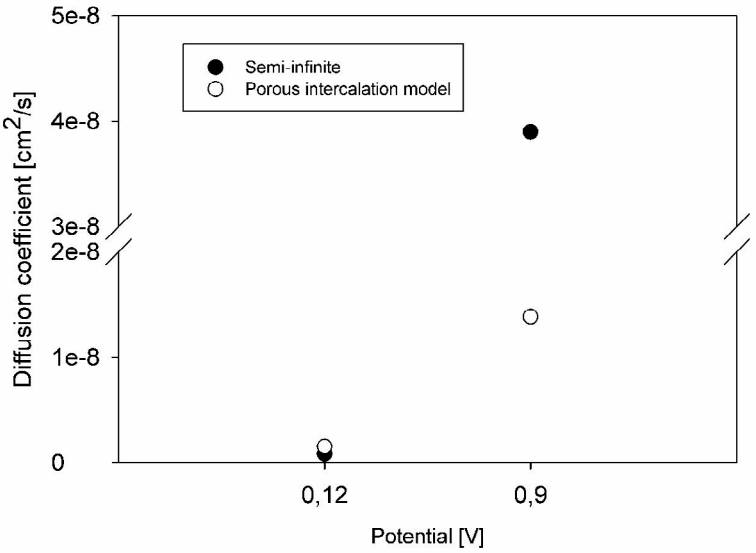

Figure 6.18. Diffusion coefficients at 0.12 and 0.9 V for graphite G8 in 4:3:3 EC:DMC:EMC + 0.9 M $LiPF_6$ electrolyte at 20 ^oC. Estimated from the high frequency semi-infinite region and using porous intercalation model.

6.5 Discussion

Impedance spectra obtained during the initial cycle, as shown in Fig. 6.3, shows how the resistance decreases upon SEI formation. This reduction of the resistance illustrates the improved kinetics of electrolyte reduction once the film formation process is initiated. Notably, the decrease in resistance after SEI formation for both SLP30 and G8 (Fig. 6.5 and Fig. 6.6) could explain why the initial capacity in Fig. 6.17 increases slightly during the first 5 cycles, before eventually decreasing with further cycling. This indicates that it takes roughly 5 cycles for a complete SEI film to form. Further decay in capacity in Fig. 6.17, is due to the resistance increase in the cell. The reduced electrolyte resistance (inset in Fig. 6.5 and Fig. 6.6) from before and after SEI formation is likely due to time difference between the spectra obtained before and after SEI formation. The impedance measurement obtained after SEI formation indicate therefore that electrolyte resistance and/or contact resistance is improved, the former possibly due to better soaking of the separator with time and passage of current.
Notably, we observed the emergence of two semi-circles for graphite G8, in Fig. 6.6, compared with SLP30, in Fig. 6.5. Further investigation of the relative contributions of the two semi-circles revealed the following: Both the high frequency area and middle frequency area experienced resistance increase upon cycling (Fig. 6.11) at 0.12 V. The same behavior was observed at 0.9 V (Fig. 6.13), only here a third semi-circle appeared as well. It is possible that this semi-circle is related to an increase in charge transfer resistance, previously observed in literature [6]. Another possible explanation is that it is related to the reduction of electrolyte species, since we are close to the potential where this is known to occur (Fig. 6.4 and 6.7). The resistance increase upon cycling for both the high frequency resistance (believed to be due to SEI) and middle frequency resistance (believed to be due to charge transfer) suggests that they are both somehow related to the SEI. Had there been a clear separation one would not expect a resistance increase for the charge transfer process with cycling, as this is mainly affected by other factors (such as potential, temperature and exchange current density).

Investigations of the effect of temperature on the impedance spectra (Fig. 6.14) revealed that the middle frequency resistance is far more influenced by the temperature compared to the high frequency resistance (Fig. 6.15). The activation energy from the Arrhenius plot in Fig. 6.16 was estimated to a value of 67.1 kJ/mol for the middle frequency arc. This values is very similar to what is expected of electrolyte with 40 % cyclic carbonates [14]. This has been related to de-solvation energy and suggests that the middle frequency arc may also be significantly affected by the de-solvation process [7, 14-16].

The diffusion coefficient estimated from the low frequency area gives reasonable results (Fig. 6.18). Differences between lithiated (0.12 V) and de-lithiated states (0.9 V) in these systems are reasonable, as a lower diffusion coefficient in a de-lithiated state would be expected due to easier lithium ion transport. Differences between the two methods are expected as the porous model provides better fit with the curvature in the low frequency region. However they are quite similar and within reasonable values for what is expected.

There is a slight deviation at 0.9 V between the traditional Warburg approach and the porous intercalation model. This is expected as the traditional Warburg approach requires knowledge on the open circuit potential varies with lithium concentration, ($\partial U/\partial c_s$). The slope is very steep at this high potential, which may cause inaccurate estimates. In addition the Warburg approach is also more applicable in cases where low frequency slope is close to 45^o, which is the case at 0.12 V, but not at 0.9 V. Therefore we rely more on the estimates provided by the porous intercalation model. In addition, the values obtained are notably smaller than what is expected for solution diffusion (around 10^{-6} cm^2/s [36]), which would improve the accuracy of our solid phase diffusion estimates, as it is less likely that there is an influence from solution diffusion. The assumption that solution diffusion is negligible is therefore reasonable.

6.6 Conclusion

Impedance spectra of SLP30 show only one semi-circle at all potentials. This suggests that the processes occurring in this system have similar time constants. By changing the surface of the graphite (from SLP30 to G8) and/or electrolyte the impedance spectra could be resolved into two semi-circles close to the intercalation potential. These were termed high frequency (HF) arc and middle frequency (HF) arc. This separation allowed for further study of how these resistances evolved with time/cycling.

The middle frequency resistance was found to have the strongest temperature dependence. This resistance increased exponentially with decreasing temperature. Arrhenius plots revealed an activation energy of around 67.1 kJ/mol, which is in accordance with similar studies [7, 14-16], and indicate a contribution from de-solvation energy.

The estimated diffusion coefficient, based on fit to a porous intercalation model for the G8 graphite, was $1.5 \cdot 10^{-9}$ cm^2/s at 0.12 V (medium SOC), which is in good agreement with values reported in the literature, and reasonable for solid state diffusion. The values obtained at 0.9 V (low SOC) were one order of magnitude higher, as expected.

All the resistances extracted from the impedance spectra in this study increased with time/cycling. Hence, the common belief that the HF arc and the MF arc are related to the surface film and the charge transfer resistance, respectively, do not hold. If this was the case it would have been reasonable to expect that the resistance attributed to charge transfer would remain constant with time/cycling. There is no foreseeable reason why the charge transfer should change, and therefore this resistance must contain contributions from both the surface film and the charge transfer resistance. These results suggest that the SEI takes a more active role in both resistance contributions, or that the charge transfer is more influenced by the SEI (i.e. by a de-solvation process or by changing the available surface area).

Acknowledgments

The Norwegian Research Council (grant number 195432/S10), SINTEF, and NTNU. The industrial partners, Elkem Carbon AS, Miljøbil Grenland AS and Carbontech Holding AS are acknowledged for their co-funding of the project.

References

1. E. Peled, *The Electrochemical-Behaviour of Alkali and Alkaline-Earth Metals in Non-Aqueous Battery Systems - The Solid Electrolyte Interphase Model.* Journal of the Electrochemical Society, 1979. **126**(12): p. 2047-2051.
2. A.J. Smith, et al., *A High Precision Coulometry Study of the SEI Growth in Li/Graphite Cells.* Journal of the Electrochemical Society, 2011. **158**(5): p. A447-A452.
3. M. Broussely, et al., *Main aging mechanisms in Li ion batteries.* Journal of power sources, 2005. **146**(1-2): p. 90-96.
4. P. Verma, P. Maire, and P. Novák, *A review of the features and analyses of the solid electrolyte interphase in Li-ion batteries.* Electrochimica Acta, 2010. **55**(22): p. 6332-6341.
5. M.D. Levi and D. Aurbach, *Simultaneous measurements and modeling of the electrochemical impedance and the cyclic voltammetric characteristics of graphite electrodes doped with lithium.* Journal of Physical Chemistry B, 1997. **101**(23): p. 4630-4640.
6. S.S. Zhang, K. Xu, and T.R. Jow, *EIS study on the formation of solid electrolyte.* Electrochimica Acta, 2006. **51**(8-9): p. 1636-1640.
7. K. Xu, *"Charge-Transfer" Process at Graphite/Electrolyte Interface and the Solvation Sheath Structure of Li+ in Nonaqueous Electrolytes.* Journal of the Electrochemical Society, 2007. **154**(3): p. A162-A167.
8. Q. Zhuang, et al., *Studies of the first lithiation of graphite materials by electrochemical impedance spectroscopy.* Chinese Science Bulletin, 2006. **51**(9): p. 1055-1059.
9. Y.C. Chang and H.J. Sohn, *Electrochemical impedance analysis for lithium ion intercalation into graphitized carbons.* Journal of the Electrochemical Society, 2000. **147**(1): p. 50-58.
10. A. Funabiki, M. Inaba, and Z. Ogumi, *A.c. impedance analysis of electrochemical lithium intercalation into highly oriented pyrolytic graphite.* Journal of power sources, 1997. **68**(2): p. 227-231.
11. A. Martinent, et al., *Three-electrode button cell for EIS investigation of graphite electrode.* Journal of power sources, 2001. **97-8**: p. 83-86.
12. A. Funabiki, M. Inaba, and Z. Ogumi, *Ac impedance analysis of electrochemical lithium intercalation into highly oriented pyrolytic graphite.* Journal of power sources, 1997. **68**(2): p. 227-231.
13. M. Holzapfel, et al., *First lithiation and charge/discharge cycles of graphite materials, investigated by electrochemical impedance spectroscopy.* Journal of Electroanalytical Chemistry, 2003. **546**(0): p. 41-50.
14. K. Xu, et al., *Solvation Sheath of Li+ in Nonaqueous Electrolytes and Its Implication of Graphite/Electrolyte Interface Chemistry.* The Journal of Physical Chemistry C, 2007. **111**(20): p. 7411-7421.
15. T. Abe, et al., *Lithium Ion Transfer at the Interface between Lithium-Ion-Conductive Solid Crystalline Electrolyte and Polymer Electrolyte.* Journal of the Electrochemical Society, 2004. **151**(11): p. A1950-A1953.

16. T. Abe, et al., *Solvated Li-Ion Transfer at Interface Between Graphite and Electrolyte.* Journal of the Electrochemical Society, 2004. **151**(8): p. A1120-A1123.
17. K. Xu, A. von Cresce, and U. Lee, *Differentiating Contributions to Ion Transfer Barrier from Interphasial Resistance and Li+ Desolvation at Electrolyte/Graphite Interface.* Langmuir, 2010. **26**(13): p. 11538-11543.
18. J.O.M. Bockris, A.K.N. Reddy, and M.E. Gamboa-Aldeco, *Modern Electrochemistry 2A*. 2 ed. 2000.
19. J.P. Meyers, et al., *The Impedance Response of a Porous Electrode Composed of Intercalation Particles.* Journal of the Electrochemical Society, 2000. **147**(8): p. 2930-2940.
20. C. Ho, I.D. Raistrick, and R.A. Huggins, *Application of AC techniques to the study of lithium diffusion in tungsten trioxide thin-films.* Journal of the Electrochemical Society, 1980. **127**(2): p. 343-350.
21. P. Yu, et al., *Determination of the Lithium Ion Diffusion Coefficient in Graphite.* Journal of the Electrochemical Society, 1999. **146**(1): p. 8-14.
22. S. Sunde, et al., *Impedance analysis of nanostructured iridium oxide electrocatalysts.* Electrochimica Acta, 2010. **55**(26): p. 7751-7760.
23. S. Sunde, et al., *An Impedance Model for a Porous Intercalation Electrode with Mixed Conductivity.* Journal of the Electrochemical Society, 2009. **156**(8): p. B927-B937.
24. F. La Mantia, et al., *Impedance spectroscopy on porous materials: A general model and application to graphite electrodes of lithium-ion batteries.* Electrochimica Acta, 2008. **53**(12): p. 4109-4121.
25. T.G. Zavalis, et al., *Aging in lithium-ion batteries: Model and experimental investigation of harvested LiFePO4 and mesocarbon microbead graphite electrodes.* Electrochimica Acta. **110**(0): p. 335-348.
26. M.H. Kjell, et al., *Electrochemical Characterization of Lithium Intercalation Processes of PAN-Based Carbon Fibers in a Microelectrode System.* Journal of the Electrochemical Society. **160**(9): p. A1473-A1481.
27. Q. Guo, et al., *Estimation of Diffusion Coefficient of Lithium in Carbon Using AC Impedance Technique.* Journal of the Electrochemical Society, 2002. **149**(3): p. A307-A318.
28. M. Doyle, J.P. Meyers, and J. Newman, *Computer simulations of the impedance response of lithium rechargeable batteries.* Journal of the Electrochemical Society, 2000. **147**(1): p. 99-110.
29. J. Besenhard and H. Fritz, *The electrochemistry of black carbons.* Angewandte Chemie. International edition in English, 1983. **22**(12): p. 950-975.
30. D. Aurbach, et al., *The electrochemistry of noble metal electrodes in aprotic organic solvents containing lithium salts.* Journal of electroanalytical chemistry and interfacial electrochemistry, 1991. **297**(1): p. 225-244.
31. D. Aurbach, et al., *The study of electrolyte-solutions based on ethylene and diethyl carbonates for the rechargeable Li batteries.2. Graphtie-electrodes.* Journal of the Electrochemical Society, 1995. **142**(9): p. 2882-2890.
32. B. Hirschorn, et al., *Constant-Phase-Element Behavior Caused by Resistivity Distributions in Films*, in *Corrosion*, D.C. Hansen, A. Alfantazi, and V.J. Gelling, Editors. p. 77-94.

33. B. Hirschorn, et al., *Constant-Phase-Element Behavior Caused by Resistivity Distributions in Films I. Theory.* Journal of the Electrochemical Society. **157**(12): p. C452-C457.
34. B. Hirschorn, et al., *Determination of effective capacitance and film thickness from constant-phase-element parameters.* Electrochimica Acta. **55**(21): p. 6218-6227.
35. G.J. Brug, et al., *The analysis of electrode impedances complicated by the presence of a constant phase element.* Journal of electroanalytical chemistry and interfacial electrochemistry, 1984. **176**(1-2): p. 275-295.
36. C. Capiglia, et al., *Li-7 and F-19 diffusion coefficients and thermal properties of non-aqueous electrolyte solutions for rechargeable lithium batteries.* Journal of power sources, 1999. **81**: p. 859-862.

7. Electrochemical impedance spectroscopy of a porous graphite electrode used for Li-ion batteries with EC/PC based electrolytes

This chapter is published in ECS Transactions [1]. *Layout may have been changed to improve readability, but the text and figures remain the same*

7.1 Summary

Electrochemical impedance spectroscopy has been employed to investigate different electrolyte compositions used for lithium-ion batteries. Diffusion coefficients in ethylene carbonate (EC) was estimated to be in order of 10^{-7}-10^{-11} cm^2/s, depending on the state of charge (SOC), and propylene carbonate (PC) based electrolytes has been estimated to be in the order 10^{-10}-10^{-11} cm^2/s. Lithium bis(oxalato) borate (LiBOB) was used as an additive in the PC electrolytes to prevent exfoliation

7.2 Introduction

Lithium-ion batteries (LIB) are and have been an important power source for portable electronic applications for many years, but they have not been widely used for large scale applications like electrical vehicles (EV). The main reasons for this are safety issues, cycle life, cost, irreversible capacity loss (ICL), and poor thermal stability. Graphite has been the main choice for anode material in lithium ion batteries mainly because of its low cost and availability. It is therefore the material of choice for the current investigations.

Many of the problems of LIB are related to the formation of a solid electrolyte interphase [2] (also called SEI layer) on the anode. SEI is a passivating film that forms during the first cycle of operation and consists mainly of decomposed species from the electrolyte. Its formation is important, as it protects the graphite from exfoliation. However, SEI is also the reason for most of the ICL since electrolyte species are trapped in the SEI film, and it can slow down or partially hinder diffusion of Li ions to and from the anode. In addition, the exothermic decomposition of the SEI at elevated temperatures contributes to decreased thermal stability of the battery and can cause thermal runaway.

With regards to thermal stability the choice of electrolyte is very important. Ethylene carbonate (EC) based electrolytes are often a common choice. Unfortunately, EC does not work well at low temperatures as it solidifies and the conductivity drops to practically zero [3]. Propylene carbonate (PC) based electrolytes on the other hand, can operate at much lower temperatures than EC. The drawback of using PC is that it does not protect the graphite as well as EC against exfoliation, which causes a large capacity loss of the anode. LiBOB was therefore used as an electrolyte additive to help protect the graphite against exfoliation [4].

In this study, electrochemical impedance spectroscopy has been employed to find values for the diffusion coefficient estimated from the high frequency area. We have used a mathematical model previously developed by Meyers et.al [5], describing porous intercalation electrodes.

The goal has been to optimize this method to make it a valuable tool for quick characterization of different LIB systems with special attention towards electrolyte composition and its effect on SEI formation, which again influences the thermal stability.

7.3 Experimental

Graphite SLP30 was used as received from TIMCAL^{TM}. The SLP30 graphite electrodes were prepared by tape casting a slurry consisting of 37 g SLP30, 2 g PVDF (Kynar), 1 g Super P (TIMCAL^{TM}), and 60 g 1-methyl-2-Pyrrolidinone (Aldrich) onto a 10 μm thick Cu-foil current collector from Circuit foil Luxembourg. The tape caster was a "K Control Coater" from Printcoat instruments. The casts were then dried in a vacuum oven at 120 ^{o}C overnight. The thickness of the casts was about 60 μm.

The electrolytes were made using varying amounts (see Table 7.1) of ethylene carbonate (Sigma-Aldrich), diethyl carbonate (Aldrich), vinylene carbonate (VC) (Aldrich) and propylene carbonate (Sigma-Aldrich) with either 1 M $LiPF_6$ (Aldrich, >99.99%) or 1 M (0.95 $LiPF_6$ + 0.05 LiBOB) where Lithium bis-(oxalato) borate (Chemetall) contributed 5 wt% and $LiPF_6$ 95 wt%.

The electrochemical measurements for the impedance and cyclic voltammetry were performed using a three- electrode cell of the model "HS-3E test cell" by Hohsen Corp. The cells assembled in inert atmosphere inside an argon-filled glove-box (O_2 and H_2O < 0.1 ppm). The cells consisted of a graphite working electrode (2.01 cm^2) with a loading of about 3 mg/cm^2, separator (Celgard® 2320), 0.75 mm thick lithium foil (1.54 cm^2) as counter electrode, and a lithium strip as a reference electrode. All potentials are reported vs. Li/Li^+ unless otherwise specified. Cyclic and linear voltammetry, and electrochemical impedance were performed using a Reference 600 potentsiostat from Gamry instruments. The initial intercalation processes were performed by cyclic voltammetry at 0.2 mV/s between 0.005 and 1.5 V. Impedance measurements were performed at 100 and 1500 mV. The frequency was varied from 10 mHz to 1 MHz with an amplitude of 5 mV. All experiments were performed at room temperature (18-24 ^{o}C) unless otherwise specified

7.4 Results and discussion

Fig. 7.1 illustrates a typical Nyquist plot from impedance measurements at 1500 mV before cycling.

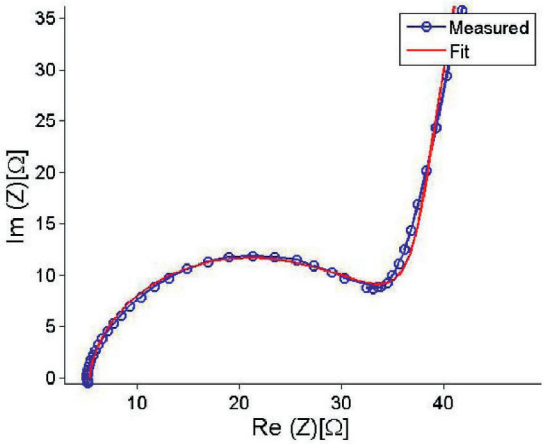

Figure 7.1. Electrochemical impedance spectroscopy of graphite SLP30 at 1500 mV before cycling(made by TIMCAL^{TM}). The fit is based on the single particle model presented by Meyers et al.[5].

The diffusion coefficients are estimated from the high frequency area of the impedance plots. From Meyers et al. [5] it was found that the faradaic impedance for a single particle with a resistive film formation in the high frequency area can be described by Eq. 7.1.

$$Z_{faradaic} \approx R_{ct,1} + R_{part}/\sqrt{(2\Omega)}(1-j) = R_{ct,1} + (-\partial U/\partial c_s)(1/F)(2\omega D_s)^{-1/2}(1-j) \qquad (7.1)$$

From Eq. 7.1 it becomes clear that a plot of either the real or the imaginary part of the impedance vs. $\omega^{-1/2}$ will give a straight line for the high frequency area. Fig. 7.2 is a plot of the real and imaginary part of the impedance vs. $\omega^{-1/2}$ for graphite SLP30 in in 1:1 EC:DEC 1M $LiPF_6$ electrolyte at 1500 mV.

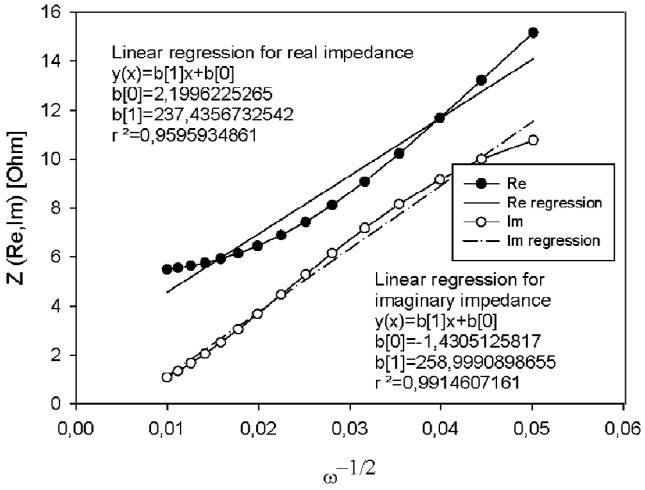

Figure 7.2. Electrochemical impedance spectroscopy of graphite SLP30 at 1500 mV in 1:1 EC:DEC 1M $LiPF_6$ electrolyte at 1500 mV.

According to Eq. 7.1 the data points for the real and imaginary part should be linear. It is clear from Fig. 2 that this is not the case. The imaginary part is in general more linear than the real part and was therefore used as the basis of our analysis. Sunde et al. [6] argues that it is better to base the impedance results on the imaginary part rather than the real part but that it is necessary to estimate the magnitude inductances disturbing the data at high frequency. In future work these inductances should be estimated and consequently subtracted.

With knowledge of how the concentration of intercalating species varies with the open circuit potential we can extract the diffusion coefficients from the slopes in Fig. 2 by combining it with Eq. 7.1. Table 7.1 summarizes different diffusion coefficients found by this approach. The measurements are done with three different electrolyte compositions and at two different potentials to investigate the difference in a sample with low and high state of charge (SOC).

Table 7.1 Diffusion coefficient with various electrolytes at 1500 and 100 mV

Potential/ Electrolyte	1:1 EC:DEC 1M $LiPF_6$	1:1 EC:DEC 1M $LiPF_6$ + 1% VC	1:1 PC:DEC + 1 M (0.95 $LiPF_6$ + 0.05 LiBOB)
1500 mV	$9.38 \cdot 10^{-7}$ cm^2/s	$1.9 \cdot 10^{-8}$ cm^2/s	$1.69 \cdot 10^{-10}$ cm^2/s
100 mV	$6.95 \cdot 10^{-11}$ cm^2/s	$1.51 \cdot 10^{-10}$ cm^2/s	$5.02 \cdot 10^{-11}$ cm^2/s

From Table 7.1 we see that for all the samples the diffusion coefficients are lower for high SOC (100mV). This is reasonable since the lithium ions will face greater resistance

in a lithiated sample compared to a de-lithiated sample. The sample with PC electrolyte shows considerably lower diffusion coefficients both at high and low SOC. Here, the addition of LiBOB did not protect the graphite completely from exfoliation. This can be seen in Fig. 7.3, where the area under the CV curve during the second cycle is far smaller than the initial cycle, indicating significant charge loss (most likely due to exfoliation).

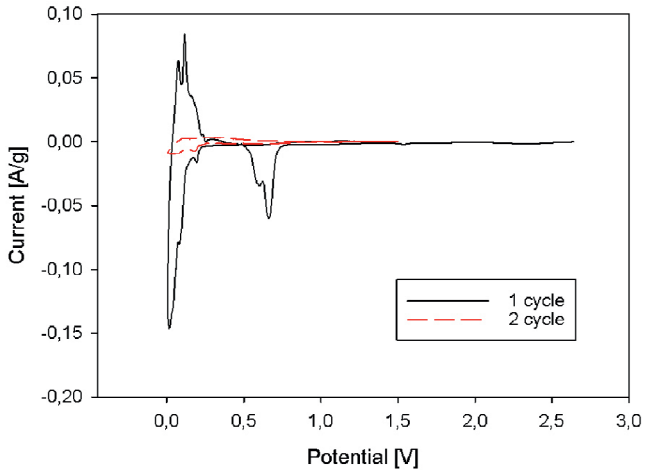

Figure 7.3. CV of graphite SLP30 for 1 M (0.95 $LiPF_6$ + 0.05 LiBOB) dissolved in 1:1 PC:DEC cycled at 0.01 mV/s.

The addition of VC yields a slightly lower diffusion coefficient at low SOC than the electrolyte without VC, but a higher diffusion coefficient at high SOC. This may be explained by VC initially adsorbing on the surface of the graphite, inhibiting the diffusion slightly, but as we go down in potential and the SOC is increasing, VC helps the diffusion indirectly by creating a more stable SEI layer and a more ordered structure. It is however difficult to conclude anything since these values are very similar and could be within experimental uncertainties

It should be mentioned that the extraction of diffusion coefficients by this method is very sensitive to the rate of change of the potential as a function of Li concentration in the graphite ($-\partial U/\partial c_s$ in Eq. 7.1). This value will naturally be very large when the graphite is de-lithiated and become smaller as the SOC is increasing. In addition, since we are extracting the data from the high frequency area, we are only investigating the outer surface of the graphite particles and not the solid state diffusion to the centre of the particle. This may cause complications since at the surface we also have the SEI layer. Further investigations are therefore needed to take this into account and separate these effects.

7.5 Conclusion

Diffusion coefficients estimated from the high frequency area of the impedance plots for graphite SLP30 in various electrolytes has been presented. The value for how the open circuit potential varies with lithium concentration ($\partial U/\partial c_s$) is very dependent on SOC and therefore may cause uncertainties in the data, especially at low SOC where this value is very large and may change rapidly. Disturbances in the impedance data due to inductances should be estimated and corrected for in future work to ensure higher accuracy of the calculations.

Reasonable diffusion coefficients have been found for graphite SLP30. This method proves to be a useful tool when the goal is to compare different electrolyte compositions and perhaps also how various additives affect the transport mechanism at different SOC. In conclusion this is a useful technique that allows us to study the surface diffusion of graphite particles. However care must be taken when interpreting the data as inductances and the $\partial U/\partial c_s$ slope may cause erroneous results. Therefore the calculated diffusion coefficients should be regarded as estimates rather than exact values.

Acknowledgments

The Norwegian Research Council (grant number 195432/S10), SINTEF, and NTNU. The industrial partners, Elkem Carbon AS, Miljøbil Grenland AS and Carbontech Holding AS are acknowledged for their co-funding of the project.

References

1. C.E.L. Foss, et al., *Electrochemical Impedance Spectroscopy of a Porous Graphite Electrode Used for Li-Ion Batteries with EC/PC Based Electrolytes.* ECS Transactions, 2012. **41**(21): p. 1-6.
2. E. Peled, *The Electrochemical-Behaviour of Alkali and Alkaline-Earth Metals in Non-Aqueous Battery Systems - The Solid Electrolyte Interphase Model.* Journal of the Electrochemical Society, 1979. **126**(12): p. 2047-2051.
3. A. Ohta, et al., *Relationship between carbonaceous materials and electrolyte in secondary lithium-ion batteries.* Journal of power sources, 1995. **54**(1): p. 6-10.
4. C. Taubert, et al., *LiBOB as Electrolyte Salt or Additive for Lithium-Ion Batteries Based on LiNi_0.8Co_0.15Al_0.05O_/Graphite.* Journal of the Electrochemical Society, 2010. **157**(6): p. A721-A728.
5. J.P. Meyers, et al., *The Impedance Response of a Porous Electrode Composed of Intercalation Particles.* Journal of the Electrochemical Society, 2000. **147**(8): p. 2930-2940.
6. S. Sunde, et al., *Impedance analysis of nanostructured iridium oxide electrocatalysts.* Electrochimica Acta, 2010. **55**(26): p. 7751-7760.

8. Summary and main conclusions

The initial part of this work aimed to investigate the effect of surface properties, employing a relatively new technique (DFT) to investigate the ratio of edge/basal planes and defect surface area of graphite, and relate this to their electrochemical and thermal properties. In the investigation of surface properties by DFT and thermal behavior the main results indicate a strong correlation between thermal response and BET surface area. However, contrary to the initial hypothesis, the thermal initiation of exothermic reactions was not significantly affected by the ratio of edge/basal planes. However, the ratio of high ICL combined with low surface area showed promising thermal properties with respect to heat evolution.

The main conclusions regarding thermal stability are that a larger surface area caused a higher thermal response related to a higher amount of SEI on the surface. The first exothermic reaction is very dependent on the SEI. A high ICL, which would indicate a large of amount of SEI, generally caused a higher thermal response in terms of more evolved heat. However a high ICL combined with a low surface area indicated a graphite surface which was highly passivating, and this seemed to be very beneficial with regards to total heat evolved. A high EC content caused the exothermic response to initiate at higher temperatures for graphite SLP30. However, this was not the case for G8 and P5. The reason for this was due to the total edge/defect surface area in relation with the total amount of EC in the solution. G8 and P5 have far less edge/defects sites available for EC reduction, and probably reached a saturation point already with small amount of EC in the electrolyte. SLP30, which has far more edge/defect sites compared to G8 and P5, showed improved thermal stability with a higher EC content, which then is related to far better passivation of the edge/defect sites here compared to with smaller amounts of EC.

The second part of this work aimed to identify good electrolytes for low temperature performance, and locate electrolyte compositions which would perform well both at low temperatures and for extended periods of time. In addition, the effect of temperature cycling on degradation was investigated.

One of the main conclusions regarding electrolyte choice and its effect on the thermal and electrochemical performance; The EC content seem to be very important, especially for long term stability. This is due to the passivating nature of the EC reduction product. The low temperature studies on capacity fade indicate that cells cycled at various temperatures experience a higher capacity fade compared to cells cycled at room temperature. Higher probability of lithium plating at low temperatures could cause this, as this can facilitate extended SEI formation and electrolyte reduction. This can lead to pressure build-up and exfoliation. Decrease in capacity at lower temperature is related to the potential shift due to decreased conductivity of the electrolyte. However the conductivity cannot explain the entire shift alone and other properties are contributing. These could be; Lithium transport through the SEI, charge transfer and de-solvation energy. The relative contributions of these could not be determined, as impedance

measurement only showed one large semi-circle. This indicates that for SLP30 the SEI and charge transfer process have similar time constants.

The final part of the work then focuses on the impedance of graphite G8, as it was discovered that in this system, the high frequency and middle frequency semi-circle were in fact separated. This allowed for further study of the relative contributions of these processes. , giving rise to these semi-circles.

Some of the main conclusions regarding EIS studies are; The high and middle frequency resistances are possible to separate, provided one obtain a beneficial electrolyte/electrode interphase, and the resistance through the SEI film is such that it allows for a different time constant compared to the charge transfer processes. Once these are separated one can study how the various contributions of HF arc and MF arc evolve with cycling and time. The main conclusion here is that they both increase with time, contrary to popular belief. The middle frequency arc was far more temperature dependent, and Arrhenius plots gave an activation energy of 67.1 kJ/mol, which is similar to previous studies with 40% EC, indicating a contribution from the de-solvation energy in the middle frequency arc. Both the high frequency and middle frequency resistance increased with time. This, combined with the temperature dependence of the middle frequency arc, further indicates the influence of a de-solvation energy contribution to the middle frequency arc, in addition to the charge transfer. This resistance increase correlated well with capacity fade from cycling, and can explain why the battery capacity eventually fades with time and cycling. Reasonable diffusion coefficients were extracted using both traditional methods and porous intercalation models.

Appendix

A.1 Abbreviations and Acronyms

BET: Brunauer, Emmet, Teller
C: Capacitance
CE: Counter electrode
CNLS: Complex nonlinear least squares
CPE: Constant phase element, also denoted (Q)
d: Interlayer distance
DEC: Diethyl carbonate
DFT: Density functional theory
DMC: Dimethyl carbonate
DSC: Differential scanning calorimetry
EA: Electron affinity or ethyl acetate
EC: Ethylene carbonate
EIS: Electrochemical impedance spectroscopy
EMC: Ethyl methyl carbonate
EQC: Equivalent circuit
EV: Electrical vehicle
FTIR: Fourier transform infrared spectroscopy
GIC: Graphite intercalation compounds
HEV: Hybrid electric vehicle
HOPG: Highly ordered pyrolytic graphite
HRTEM: High-resolution transmission electron microscopy
HT: Heat treatment
ICL: Irreversible capacity loss
L_a: Crystallite size along the graphene layers
L_c: Crystallite size perpendicular to the graphene layers
LIB: Lithium ion batteries
LECO: (Leco TC-436) Oxygen-Nitrogen Analyzer
NE: Negative electrode
NMP: 1-Methyl-2-pyrrolidone
OCV: Open circuit voltage
PE: Positive electrode
PC: Propylene carbonate
PSD: Particle size distribution
PVDF: Polyvinylidene difluoride
RA: Radical anion
R_e: Electrolyte resistance
RE: Reference electrode
R_{hf}: High frequency resistance
R_{lf}: Low frequency resistance
R_{mf}: Middle frequency resistance
RT: Room temperature
SD: Standard deviation
SEM: Scanning electron microscopy
SEI: Solid electrolyte interphase
SOC: State of charge
VC: Vinylene carbonate
WE: Working electrode
XRD: X-ray diffraction
XPS: X-ray photoelectron spectroscopy
Å: Ångstrom

A.2 List of conferences and publications

"Carbon materials for improved stability of anodes for Li-Ion batteries", iSCREAM (*internal Symposium on Ceramics and Energy Related Advanced Materials*), Trondheim, March 2010. Oral presentation

"Carbon materials for improved stability of anodes for Li-Ion batteries: An electrochemical impedance spectroscopy study", iSCREAM (*internal Symposium on Ceramics and Energy Related Advanced Materials*), Trondheim, March 2011. Oral presentation

"Electrochemical impedance spectroscopy of a porous graphite electrode used for Li-ion batteries with EC/PC based electrolytes", 220th Electrochemical Society (ECS) meeting, Boston**,** Massachusetts, October 9-14 2011. Poster session

"Short introduction to Li-Ion batteries", iSCREAM (*internal Symposium on Ceramics and Energy Related Advanced Materials*), Trondheim, March 2012. Oral presentation

"Electrochemical impedance spectroscopy of a porous graphite electrode used for Li-ion batteries with EC/PC based electrolytes", ECS Transactions 2012. 41(21): p. 1-6. Publication

"Investigation of temperature dependent stability of ethylene carbonate and propylene carbonate in multicomponent electrolytes for Lithium ion batteries" Kifee (*Kyoto International Forum for Energy and Environment)*, Trondheim, 9-12 september 2012. Oral presentation

"Investigation of temperature dependent stability of ethylene carbonate and propylene carbonate in multicomponent electrolytes for Lithium ion batteries ", 222th Electrochemical Society (ECS) meeting, Hawaii, Honululu**,** October 7-12 2012. Oral presentation

"Study of electrolytes for lithium ion batteries working in a wide temperature range", Trondheim, Seminar Inorganic materials and ceramics research group, November 7, 2012 . Oral presentation

"Density functional theory study of industrial graphite", International Battery Association (IBA) meeting, Barcelona, Spain, March 10-15th 2013. Poster session

"DFT assisted assessment of amount of edge/basal plane in non-commercial graphite used in Lithium Ion Batteries", Seminar Electrochemistry group, Trondheim 18 June 2013. Oral presentation